Elasto-capillarity in wood fibres

Majid Soleimani

Department of Chemical Engineering

McGill University

Montreal, Canada

April 2015

A thesis submitted to McGill University in partial fulfillment of the requirements for the degree of Doctor of Philosophy in Engineering.

Abstract

Capillary-driven deformations of flexible fibres remarkably affect the properties of a fibrous material in a wet or dry state. For example, capillary forces can eliminate wood-fibre lumens and collapse them into a ribbon-like conformation during the drying of a wet paper sheet. Furthermore, liquid bridges at the intersections of wet fibres can bring them into a close proximity and conform their surfaces to each other to produce a strong permanent bond. These deformations significantly change various paper properties, such as strength, hygroscopicity, and resistance to curling and edge crush.

Although elasto-capillarity in wood fibres is technologically important, it has not yet been quantitatively analyzed. In this thesis, I model the fibres with smooth circular tubes that have constant cross sections and contact angles, and analyze the deformations that are driven by the capillary forces. I begin by deriving an analytical approximation for the shape of a liquid droplet or a gas bubble on a curved surface, and apply this solution to a droplet residing either inside or outside of a circular tube. Then, I use the Surface Evolver software to numerically calculate the shape, Laplace pressure, and surface energy of an interface bridging either the interior walls of a buckled tube or the intersection of two different circular filaments. This numerical solution is coupled with analytical solutions of elastic deformations to compute the equilibrium configurations at various liquid volumes.

Based on the analysis of the droplet shape on curved surfaces, I conclude that the most energetically favoured location for the droplet is the point where the substrate has the most inward curvature. I can also estimate the capillary pressure that such bubbles impose on the wood fibres during drying. By analyzing the capillary-driven lumen collapse of the tube, I show the effects of wetting angle, tube-wall flexibility, and pit-hole size on the collapsing behaviour of wood fibres. I quantitatively prove that capillarity can flatten wood fibres during drying. Finally, by investigating the deformations of two crossing flexible filaments with a liquid bridge at their intersection, I predict that the capillary force goes through a

maximum as the liquid volume decreases. This is in contrast with parallel flexible filaments and in agreement with experimental observations. This investigation predicts the maximum possible capillary force between crossing fibres as well as the liquid volume where this peak force occurs.

These analyses are beneficial in many other applications including contact-angle measurements on curved surfaces, micro-electromechanical systems, and welding of flexible components.

Résumé

Les déformations des fibres souples entraînées par des capillaires affectent remarquablement les propriétés d'un matériau fibreux dans un état humide ou sec. Par exemple, des forces capillaires peuvent éliminer les lumens des fibres de bois et les effondre dans une conformation en forme de ruban pendant le séchage d'une feuille de papier humide. En plus, des ponts liquides aux intersections des fibres humides peuvent les amener dans une proximité proche et conformer leurs surfaces les unes aux autres pour produire une liaison permanente forte. Ces déformations changent significativement les différentes propriétés du papier telles que la résistance, la hygroscopicité, et la résistance à se courber et à l'écrasement du bord.

Bien que la capillarité élastique dans les fibres de bois soit technologiquement importante, celle-ci n'a pas encore été analysée quantitativement. Dans cette thèse, nous modélisons les fibres avec des tubes circulaires doux qui ont des sections transversales et des angles de contact constants, et analysons les déformations qui sont entraînées par les forces capillaires. Nous commençons par dériver une approximation analytique pour la forme d'une goutte de liquide ou une bulle de gaz sur une surface courbée, et appliquons cette solution à une gouttelette résidant soit à l'intérieur ou à l'extérieur d'un tube circulaire. Ensuite, nous utilisons le logiciel Surface Evolver pour calculer numériquement la forme, la pression de Laplace et l'énergie de surface d'une interface faisant le pontage entre les murs intérieurs d'un tube déformé ou à l'intersection de deux filaments circulaires différentes. Cette solution numérique est jumelée avec les solutions analytiques de déformations élastiques pour calculer les configurations d'équilibre à différents volumes de liquide.

En considérant l'analyse de la forme de gouttelettes sur des surfaces courbées, nous concluons qu'énergiquement l'endroit le plus favorisé pour la gouttelette est le point où la courbure du substrat est la plus prononcée vers l'intérieur. On peut aussi estimer la pression capillaire que ces bulles imposent sur les fibres de bois durant le séchage. En analysant l'effondrement de lumen du tube entraîné par la capillaire, nous montrons les effets de l'angle de mouillage, de la flexibilité du mur de tube, et de la taille de trou de la fosse sur le comportement effondrant des fibres de bois. Nous prouvons quantitativement que la capillarité peut aplatir des fibres de bois pendant le séchage. Finalement, en recherchant les déformations de deux filaments flexibles croisés avec un pont de liquide à leur intersection, nous prévoyons que la force capillaire passe par un maximum lorsque le volume de liquide diminue. Ceci est en contraste avec des filaments souples parallèles et en accord avec les observations expérimentales. Cette recherche prévoit la force capillaire maximale possible entre des fibres croisées ainsi que le volume de liquide où cette force maximale se produit.

Ces analyses sont bénéfiques dans de nombreuses autres applications, y compris les mesures d'angle de contact sur des surfaces courbées, des systèmes micro-électromécaniques et le soudage de composants flexibles.

Acknowledgments

I would like to express my profound gratitude to everyone who helped me during my long path to accomplish a PhD degree, including my teachers, friends, and colleagues.

My sincere thanks go to my supervisor Professor Reghan J. Hill for his patience, inspirations, and invaluable advices and teachings. I am deeply thankful to my co-supervisor Professor Theo G.M. van de Ven who was always helpful and offered precious guidance. I also thank Louis Godbout who kindly taught me and provided me with his useful ideas during my experiments.

My special thanks to the research groups from Professor Hill and Professor van de Ven labs for providing me with a friendly environment for my research.

I am grateful for the financial support from the Green Fibre Network, and also for giving me the opportunity to present my research to an interested audience from industry and academia in FIBRE conferences. I would like to thank the Faculty of Engineering, McGill University too, for the financial support through a McGill Engineering Doctoral Award.

Last but not least, I am deeply thankful to my wife who supported me with love and energy, my parents who always encouraged me and inspired me, and my brothers and sisters who honestly supported me, and I owe all of my achievements to them.

Contribution of Authors

Majid Soleimani developed the theoretical models, performed the numerical calculations, and conducted the experiments. He also wrote the manuscripts and applied the feedbacks from the supervisor and co-supervisor.

Reghan J. Hill supervised this research and provided the author with his valuable ideas and advices. He also edited the manuscripts and submitted them to the scientific journals.

Theo G.M. van de Ven provided general guidance and valuable feedbacks on the manuscripts.

Contents

List of Figures

List of Tables

Nomenclature

A	Scaled amplitude of the harmonic surface
ADSA	Axisymmetric drop shape analysis
A_H (J)	Hamaker constant
AR	Aspect ratio
A_{lg}	Scaled liquid-gas interfacial area
A_{sg}	Scaled solid-gas interfacial area
A_{sl}	Scaled solid-liquid interfacial area
A_n, B_n	Coefficients of the substrate perturbation
CI	Collapse index
C_n, D_n	Coefficients of the final perturbation solution
D_{min}, D_{max} (μm)	Shortest and longest external diameters of wood fibres
E (J, Pa)	Interfacial energy in Chapter 3,
	Young's elastic modulus in Chapters 4 and 5
F (N m^2)	Flexibility
FSP	Fibre saturation point
F_i (N)	Capillary force
H (m^{-1})	Mean curvature
I (m^4)	Area moment of inertia
L (m)	Length of filaments
LA, LA_0 (m^2)	Lumen area, initial lumen area
L_i (m)	Length of interface along the filaments
M (N m)	Bending moment
M_i (N m)	Capillary torque
P (Pa)	Laplace pressure
P_b (Pa)	Buckling pressure

P_c (Pa)	Capillary pressure
P_e (Pa)	Elastic pressure
P_{max} (Pa)	Maximum Laplace pressure
P_o, P_i (Pa)	External and internal pressures
P_0 (Pa)	Hydrostatic pressure at the level of tube center
R (m)	Radius of circular tube in Chapter 4, interface radius of curvature in Chapter 5
R_e (m)	Terminal interface radius of curvature
RMS	Root mean square
R_h (m)	radius of the hole
R_0 (m)	Spherical drop radius in Chapter 3, buckled tube radius of curvature at $y = 0$ in Chapter 4
R_1, R_2 (m)	Principle radii of curvature of interface
S (m)	Tube circumference
$S1, S2, S3$	Layers of the fibre secondary wall
U (m s^{-1})	Drop velocity in Chapter 3, total energy in Chapters 4 and 5
U_i (J)	Interfacial energy
U_e (J)	Elastic strain energy
V (m^3)	Fluid volume
V_G (m^3)	Gas volume
V_L (m^3)	Liquid volume
V_T (m^3)	Tube lumen volume
V_0 (m^3)	Initial tube volume
a (m)	Characteristic length
a_i	Coefficients of the fitted curve
d (m)	Filaments separation
f_m	Shape factor
$\varepsilon f(\theta)$	Perturbation of contact line
g (m s^{-2})	Gravitational acceleration
$\varepsilon g(r, \theta)$	Perturbation of interface
$\varepsilon h(r, \theta)$	Perturbation of substrate
εk	Perturbation of Laplace pressure
l_c (m)	Capillary length
n	Degree of fitted curve

n_i, n_s	Unit normal vectors on the interface and substrate
p_0 (Pa)	Gas pressure
p (Pa)	Liquid pressure
r (m)	Filament radius in Chapter 5
(r, θ, z)	Cylindrical coordinates in Chapter 3
r_0 (m)	Distance from the center at $y = 0$
z_0 (m)	Substrate shape equation
α (°)	Equilibrium contact angle
Γ	Dimensionless substrate-curvature gradient
γ (J m^{-2})	Liquid-gas interfacial tension
γ_{sg} (J m^{-2})	Solid-gas interfacial tension
γ_{sl} (J m^{-2})	Solid-liquid interfacial tension
δ (m)	Cut-off distance in Chapter 3,
	crossing angle between filaments in Chapter 5
ε	Perturbation parameter
ζ	Dimensionless friction coefficient
η (Pa s)	Fluid viscosity
κ (m^{-1})	Wave number of harmonic surface
λ (m)	Wave length of harmonic surface
ν (m)	Filament deflection
ξ_n, η_n	Coefficients of interface perturbation
ρ (kg m^{-3}, m)	Density in Chapter 4, radius of curvature of deflected filament
τ (Pa)	Shear stress
ϕ (°)	Half-opening angle of solid-liquid interface
ϕ_e (°)	Terminal Half-opening angle of solid-liquid interface
Ω	Elasto-capillary number

Chapter 1

Introduction

When a meniscus is formed at the interface of two fluids, the interfacial tension produces a 'capillary force' that accounts for many natural and industrial observations; for example, the clumping of wet hair into bundles (Bico *et al.*, 2004), coalescence of paintbrush fibres (Kim & Mahadevan, 2006), standing of aquatic insects on water (Hu & Bush, 2005), and lung airway closure (Heil *et al.*, 2008). Capillarity produces a surface force that depends on the first power of a characteristic length a (Lambert, 2007). With a small a, this force dominates body forces that depend on a^3. By dominating gravity for example, it makes water and nutrients rise in long trees and produces capillary adhesion among sand particles to facilitate sculpting with wet sand.

The capillary force in a small length scale can deform the elastic solids that are surrounding the meniscus. This deformation is termed 'elasto-capillarity', indicating the coupling of the elastic and capillary forces. Elasto-capillarity depends on the solid modulus of elasticity, surface tension, and contact angle (Mastrangelo & Hsu, 1993). The equilibrium point is the minimum of the total energy, which consists of the elastic and interfacial energies.

Because of the recent advances in micro- and nanotechnology, elasto-capillary deformations have been extensively investigated in the last two decades (Roman & Bico, 2010; Liu *et al.*, 2012). One of the most important applications is the surface-tension-driven collapse of elastic materials in a micro- or nanometer length scale. Capillary collapse is observed in the rearranging of carbon nanotube arrays (Chakrapani *et al.*, 2004), bundling of carbon nanotubes during evaporation (Lau *et al.*, 2003), and resist pattern damage (Tanaka *et al.*, 1993).

1.1 Elasto-capillarity in wood fibres

For more than 2000 years, cellulosic fibres have been used in paper sheets to produce a powerful means for communicating and sharing knowledge and art all over the world (Hubbe & Bowden, 2009). These fibres are typically $1-3$ mm in length and $20-30$ μm in diameter, and composed of sugar-based polymers (cellulose and hemicellulose), lignin, and water, with lesser amounts of extractives, protein, starch and inorganics. The distribution of these chemical components varies from plant to plant, and within different parts of the same plant (Bledzki *et al.*, 2002). Wood fibres have an anisotropic tubular structure with a lumen that is filled with water in wood or pulp, and a wall that is divided into several layers.

When manufacturing a papersheet from wood, several chemical and mechanical processes are required to impose significant changes on wood fibres. The first step to 'activate' the fibres for these changes is 'pulping', which separates the wood into its individual fibres (Hubbe *et al.*, 2007). Different pulping processes are mechanical pulping, semichemical pulping, and chemical pulping (Walker, 2006). In the next step, the fibres are subjected to shearing and compression loads in 'refining' and their conformability and capability of bonding together are adjusted for a specific paper grade. After adding chemical additives, the fibres are pressed and dried at a high pressure and temperature, respectively. The dried papersheets are then pressed again in 'calendaring' to furnish a smooth surface.

During drying, a meniscus can be formed either inside or outside of a single fibre or between different fibres. The resulted capillary force can deform the fibres and affect the network properties. In this project, I investigate whether this capillary force can eliminate the fibre lumen, and can deform the fibres in a network. The elasto-capillarity can also affect other aspects of the fibres such as internal or external fibrillation (Hubbe, 2007), but they are not investigated in this thesis.

1.2 Short-range forces

In addition to the capillary forces, there are several other forces that may affect wood-fibre dimensional changes during drying. For example, van der Waals, electrostatic, and hydrophobic forces can dominate capillarity when the fibre walls become very close to each other. Van der Waals forces between molecules are developed through three different mechanisms: Keesom Interaction between two permanent dipoles, Debye Interaction between a permanent dipole and a corresponding induced dipole, and London Dispersion Interaction between two instantly induced dipoles. Although these interactions are effective in molecular scales, their pair-wise summation can lead to van de Waals forces between macroscopic solids (Butt & Kappl, 2009), producing for example a significant attractive force for some animals to stick to walls and ceilings (Santos *et al.*, 2007).

A solid surface in water is usually charged, and therefore, attracts counter ions. The surface charges and counter ions together produce an electric double layer (Butt & Kappl, 2009). An overlap between the electric double layers of two charged surfaces produces an electrostatic double-layer force, which is basically different from the Coulomb force.

There are also other forces in water that are not well understood, such as hydration and hydrophobic forces. The hydration force is caused by the energy required to remove the water of hydration from a hydrophilic surface, and tends to repel two hydrophilic surfaces when their separation is less than a few nanometers (Butt & Kappl, 2009). However, hydrophobic surfaces, which have contact angles higher than 90° with water, tend to attract each other by hydrophobic forces. These forces originate from the tendency of the system to reduce the solid-water interfacial area by connecting the hydrophobic surfaces to each other.

Nevertheless, the van de Waals forces between macroscopic solids, electrostatic double-layer forces, and hydrophobic forces only become important when the distance between the two surfaces is less than 100 nm. At distances as large as 10 μm, only capillary forces are significant. Consequently, considering the wood-fibre dimensions, the capillary forces dominate at the initial stages of wood-fibre deformation during drying.

1.3 Surface Evolver

Brakke (1992) first developed Surface Evolver as a computer program that iteratively minimizes the energy of a surface. This program was then used widely to numerically calculate the shape of an interface, when subjected to several constraints, such as the surrounding geometry and fluid volume. The energy consists of the surface energy, gravity, and other forms. The available energy minimization methods are the 'gradient descent', 'conjugate gradient', and 'hessian' methods. The first and second methods minimize the energy, while the third method finds the zero-gradient point, which can be a maximum, minimum, or saddle point. Therefore, the hessian method can reach unstable equilibrium configurations too. A saddle point can be reached by all of these methods, but can be avoided by continuing the iterations while using the conjugate gradient method. The constraints are implemented using Lagrange multipliers. Surface Evolver comes with a comprehensive useful manual that includes the technical details of the code, several examples explaining how to use Surface Evolver, and theory and formulation (Brakke, 2008).

Surface Evolver discretizes a surface into a number of points termed 'vertices'. These points are connected to each other by directed lines termed 'edges' that have a head and a tail vertex. The edges are assembled according to the right-hand rule for the normal vector to produce triangular surface elements termed 'facets'. The facets can develop a body element that has a particular volume. Using divergence and Green's theorems, the volume and surface energies can be given as an energy integrand to the surrounding surfaces and edges, respectively.

Once the geometry and constraints are defined precisely, Surface Evolver can begin iterations toward the minimum energy. In this thesis, I couple Surface Evolver with Matlab to intelligently run Surface Evolver for many times without needing any manual interference. After defining an initial geometry, I explore a procedure that can evolve the surface to a converged state with a desired mesh size, when changing a specific parameter. This procedure is used by Matlab to automatically call Surface Evolver and calculate the interface shape for the various values of the parameter. The final solution is always checked manually to show the first-order convergence rate with respect to the number of facets. This technique enables us to couple the elastic deformations of the surrounding solids to the interface-shape changes. Details of the Matlab codes, as well as the initial geometry and solution procedures of the Surface Evolver software are available in appendices.

1.4 Objectives

This research was performed in the context of a larger project: 'control of lumen collapse in hydrophobically modified fibres' and in collaboration with the 'Green Fibre Network'. The main objective of the project is to explain the mechanisms of the wood-fibre dimensional changes during drying including fibre lumen collapse and shrinkage, thus improving the paper-products barrier and mechanical properties by controlling these changes.

The wood-fibre deformation during drying is important in many paper products. Traditional applications of paper are in packaging, printing and writing, and absorbents. Open-lumen fibres for example, can be used to increase the thickness and stiffness of the packaging papers without increasing the weight and cost, and furnish large air-filled spaces in the absorbent papers to increase the amount of water that can be absorbed. Furthermore, collapsed-lumen fibres can enhance inter-fibre bonding and paper strength in all kinds of paper products (Hubbe, 2007). Recently, open-lumen fibres are used as structural fillers for bulk composite materials to reduce the consumption of more expensive binder materials and improve their properties, particularly in the automotive industries, building applications, furniture and panels, and aerospace applications. (Bledzki *et al.*, 2002).

In this thesis, I focus on the capillary role on the wood-fibre dimensional changes during drying by modelling the fibres with elastic circular tubes, and analysing the capillary-driven deformations of the tubes. Therefore, my first objective is to compute the liquid-gas interface shape inside or outside of the tubes. Particularly, I want to calculate the shape of a gas bubble or a liquid drop on a curved surface to investigate the substrate-curvature impact on the shape, capillary pressure, and surface energy of the bubble or drop. This investigation furnishes the stable positions of the bubble or drop on the curved substrate.

The second objective is to quantify the lumen collapse of the circular tube, which is driven by a capillary pressure. Because a significant Laplace pressure on a fibre is produced by the interfaces pinned to the pit holes on the fibre wall, I consider that the pressure is imposed on the tube by a bubble that is pinned to a small hole on the tube wall. I want to calculate the necessary conditions that enable the capillary forces to bring the fibre walls into molecular proximity, thus allowing the van der Waals interactions and hydrogen bonds to make a permanent collapsed fibre.

The third objective is to investigate the wood-fibre deformations driven by liquid bridges between fibres. Capillary forces in a wet paper can readily deform wood fibres because of the increased fibre flexibility in a wet state. I want to calculate the equilibrium capillary force between flexible fibres and investigate the effects of the fibre flexibility, contact angle, liquid volume, and separation. This force furnishes the wet-paper strength when the solid content is less than 40% (van de Ven, 2008), and the molecular contact between the fibres during drying (Persson *et al.*, 2013), affecting various properties of the final product such as strength and porosity.

1.5 Thesis outline

This is a manuscript-based thesis with the following Chapters:

Chapter 2 is a literature review on bubbles and drops on curved surfaces, capillary driven collapse of circular tubes and wood fibres, and capillary forces between fibres.

Chapter 3 presents an analytical approximation of the shape of a liquid drop or a gas bubble on a curved surface. The solution is then used to compute the shape of a drop on a circular tube and a harmonic surface, comparing the results with numerical solutions. The substrate-curvature impact on the capillary pressure and surface energy are investigated, and the most energetically favoured (stable) positions for drops are calculated. This Chapter was published in Langmuir (Majid Soleimani, Reghan J. Hill, and Theo GM van de Ven, Bubbles and drops on curved surfaces. Langmuir 29.46 (2013): 14168-14177).

Chapter 4 investigates the capillary driven collapse of a circular tube as a model for a wood fibre. The elastic deformation of the circular tube is calculated from an analytical solution, the interface shape is calculated numerically from the Surface Evolver software (Brakke, 1992), and the elasto-capillarity is analyzed by coupling these solutions using Matlab. A phase diagram is obtained which separates collapsing and non-collapsing regimes based on elasto-capillary number and contact angle, and is tested with experimental results. This Chapter was published in Journal of Materials Science (Majid Soleimani, Reghan J. Hill, and Theo GM van de Ven, Elasto-capillary collapse of circular tubes as a model for cellulosic wood fibres. J. of Mater. Sci. 50.15 (2015): 5337-5347.).

Chapter 5 reports the effects of the flexibility, contact angle, liquid volume, crossing angle, and filament separation on the capillary force between two parallel or crossing flexible filaments. The results help to understand the capillary role in the fibre-product structure, wet-paper strength, and inter-fibre bonding. This Chapter was accepted in Langmuir.

Chapter 6 reviews the general conclusions, and explains how these conclusions can benefit the papermaking industry.

Chapter 2

Literature review

2.1 Capillarity and surface tension

Capillarity was first documented by Hauksbee (1710*a*,*b*) when he proposed that an attraction between glass and water causes the water rising in a capillary tube, independent of the glass thickness. Several experimental and theoretical investigations were performed on this phenomenon until Segner (1751) introduced the concept of liquid 'surface tension', which was later used by Young (1805) to establish his theory on capillary phenomena. Young also introduced the concept of 'contact angle', and used these two principles to solve several capillary problems. In his theory, he assumed an attractive force between particles, which is constant in small separations, and a repulsive force, which increases rapidly when the particles get close. He concluded that a particle is urged toward the centre of curvature of the surface by a force that is proportional to the mean curvature of the interface. Laplace (1806) also used the same principles to solve identical problems, but in a completely mathematical way. These two principles were later termed Young-Laplace and Dupré-Young conditions. The former states that the pressure drop in an interface is equal to its surface tension times the sum of the principle curvatures, and the latter relates the surface tensions between the three phases at a triple contact line to the angle that the three interfaces make with each other.

2.1.1 Sessile drop on a flat surface

The most popular method to measure the contact angle, which is also capable of measuring the surface tension (Kabza *et al.*, 2000), is to take a side picture of a sessile drop on a smooth flat surface, and try to measure the angle between the interfaces at the three-phase contact point. Bigelow *et al.* (1946) invented a 'telescope-goniometer' to measure the contact angle by depositing a liquid drop with an accurate volume on a completely horizontal stage and reading the contact angle with a protractor through a telescope eyepiece. This instrument was modified through years by using a camera to take photographs of the drop profile (Leja & Poling, 1960) with a high magnification (Smithwich, 1988), and using a motor-driven syringe (Kwok *et al.*, 1996) to measure dynamic contact angles.

Because the accurate measurement of the contact angle and surface tension is technologically important, the contact-angle calculation of a sessile drop on a flat surface has been excessively investigated. Bateni *et al.* (2003) fitted a polynomial to the drop contour close to the contact point, and take the derivative of the polynomial to calculate the contact angle. A similar method was used by fitting a spline (Stalder *et al.*, 2006), a sphere (Yang & Lin, 2003), or an axisymmetric solution of the Young-Laplace equation (Bashforth & Adams, 1883; Smith & Van de Ven, 1984; Hoorfar & Neumann, 2004), i.e., axisymmetric drop shape analysis (ADSA). Another method is to calculate an analytical approximation of the drop profile using perturbation methods, and fit the approximate solution to the drop contour (Ehrlich, 1968; Shanahan, 1984; Stalder *et al.*, 2010).

2.1.2 Sessile drop on a curved surface

The contact-angle-measurement method described in Section 2.1.1 is restricted to flat, ideal, horizontal surfaces. Nevertheless, non-axisymmetric drop morphology was recently studied to analyze the wettability of heterogeneous curved surfaces. Iliev & Pesheva (2006) proposed a numerical method to measure the local contact angles of a drop when the liquid volume, capillary length, and three-phase contact line are known. The method was an iterative minimization procedure that is capable of calculating non-axisymmetric drop shapes, and must be combined with experimental data, similar to ADSA methods. In another study, Guilizzoni (2011) developed a procedure to measure the contact angle on curved surfaces by only taking a side view of a drop contour, while the values of the liquid volume and surface tension are not identified. He could visualize the three dimensional shape of the drop using image processing, spline fitting, and numerical integration.

The effect of substrate curvature on wettability was studied by Extrand & Moon (2008) when they deposited small drops at the apex of polymer spheres to experimentally measure the apparent advancing contact angle while increasing the liquid volume. They corrected the measured contact angles for the substrate curvature, and concluded that the contact angles are the same as on flat, horizontal surfaces.

2.1.3 Drop motion driven by substrate curvature

Hauksbee (1710*b*) observed the self-propulsion of liquid drops between two non-parallel plates for the first time. Since then, several investigations were undertaken to explain and quantify how gradients of substrate properties can induce a drop motion. Lorenceau & Quéré (2004) studied the drop self-propulsion on a conical fibre towards regions of large radius, driven by a gradient of Laplace pressure, which is induced by the gradient of radius of curvature of the fibre. The drop equilibrium conformation and location on a vertical conical fibre was studied numerically by Liang *et al.* (2015). Although continuous motion without equilibrium was observed in the absence of gravity, the drops stopped at an equilibrium location when gravity was present. This mechanism is used by some shorebirds to transfer their prey from the beak tip toward the mouth (Prakash *et al.*, 2008; Bush *et al.*, 2010), and by cactuses for efficient fog collection (Guo & Tang, 2015).

Rapid propulsion of a liquid droplet is also achievable using a substrate-curvature gradient. Yao & Bowick (2012) proved theoretically that a gradient of roughness can propel liquid droplets toward maximal-roughness regions for hydrophilic surfaces, and minimal-roughness regions for hydrophobic surfaces. In an experimental investigation, Lv *et al.* (2014) reported a rapid motion of micro- and nanodroplets driven by a substrate-curvature gradient on both hydrophilic and hydrophobic surfaces, and showed that this mechanism drives small droplets faster than large droplets. Rapid drop propulsion is useful in lab-on-chip, and to refresh the heat transfer area in heat exchangers.

2.2 Elasto-capillarity

The surface-tension-driven deformation of elastic solids was first investigated because of its importance in microstructures (Mastrangelo & Hsu, 1993) and in lung airway closure (Halpern & Grotberg, 1992; Grotberg, 1994). Rapid advances in micro- and nanotechnology motivated elasto-capillary analysis in other applications, such as the bundling of the paint-brush hairs when it is removed from the liquid (Kim & Mahadevan, 2006), the production of three-dimensional structures by the wrapping of a liquid droplet with a planar sheet (Py *et al.*, 2007), and the capillary rise through flexible structures (Duprat *et al.*, 2011). These studies are well reviewed in Roman & Bico (2010) and Liu *et al.* (2012).

2.3 Wood-fibre lumen collapse

Wood consists of highly ordered cell systems in both axial and radial directions. In the axial direction, cells are extended along the trunk, and have different sizes and shapes depending on their role in the tree. While thick-walled cells are responsible for mechanical support and strength, thin-walled cells provide liquid transfer and nutrient storage (Monica *et al.*, 2009; Bledzki *et al.*, 2002).

The most important component in wood, which has crucial effects on its structure and properties, is water. Water in wood can exist both in the cell lumens and intercellular spaces, termed absorbed water or free water; and within the cell walls, termed adsorbed water or bound water. Because water first evaporates from the lumens and intercellular spaces during drying, there exists a situation called the Fibre Saturation Point (FSP), at which all of the absorbed water has been removed but the cell walls are still fully saturated. FSP is the point at which a different scenario occurs for the water evaporation, and the mechanical properties of fibres change (Walker, 2006).

There are several factors affecting the wood-fibres performance in a specific application, including its chemical composition, physical properties, and mechanical properties. Some of the most significant physical properties of wood fibres are the fibre dimensions, defects, strength, and structure. Knowing the fibre length and width is essential for comparing different kinds of wood fibres. For example, the aspect ratio, which is defined as the ratio of the fibre length to width, gives an indication of fibre strength (Bledzki *et al.*, 2002).

The fibre lumen can be eliminated when the fibre is subjected to an external load. Because of the crucial effect on wood-fibre products, lumen collapse has been widely studied for several decades. Wilkes & Wilkins (1987) supposed that the cell collapse is the reason for shrinkage during drying and occurs above FSP, considering capillarity as the most widely accepted explanation for this phenomenon. They claimed that the fibre tendency to collapse does not always depend on the ratio of wall thickness to lumen diameter, and some other factors, such as proximity to other cell types, may be involved. Hayashi & Terazaws (1992) conducted systematic experiments using water saturated Balsa wood, and identified necessary conditions leading to the cell collapse and the required stress level. They observed that after the cell collapse reached a maximum limit, part of the cell deformation recovered upon removing liquid tension.

Innes (1995*a*) developed a stress model of a fibre to predict the onset of collapse. The fibre cell was modelled as a thick walled cylinder, with a ratio of outside diameter to wall thickness of the order of 5. Neglecting longitudinal effects, he assumed that plane transverse sections remain plane (Navier hypothesis) and solved a one-dimensional problem. The model predicted the stress and strain distributions within the fibre wall as a function of temperature, moisture content, and strength properties and size of the fibre wall in the early stages of drying. Innes (1995*b*) reported a temperature called the collapse threshold temperature, as the highest temperature at which wood can be dried to FSP without resulting in collapse. In another study (Innes, 1996*b*), he measured large amounts of shrinkage in latewood slices, and lesser amounts in earlywood slices, while there was no shrinkage in the earlywood when the slices were dried at temperatures below the collapse threshold. Innes (1996*a*) showed that the safest way of avoiding collapse is to dry at temperatures below the collapse threshold temperatures of both the earlywood and the latewood. Innes & Redman (2003) employed a standard drying process, which was optimized by a drying model, to compare the response of the six different wood species. In contrast to their previous works, they conclude that collapse cannot be avoided by drying at lower temperatures.

Brodribb & Holbrook (2005) investigated the collapse of lignified cells peripheral to a leaf vein, modeling them with an array of cylindrical fibres aligned perpendicular to the leaf vein. They observed that during leaf dehydration the majority of these fibres collapsed from circular to flat. A simple mechanical model of fibre collapse, which is derived from the theoretical buckling pressure for pipes, accurately predicted the collapse dynamics.

2.3.1 Collapse index

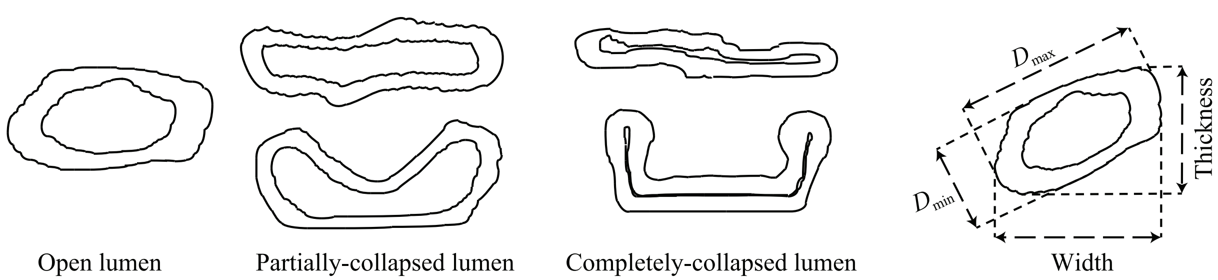

Figure 2.1: Left: Fibre cross sections with open, partially-closed, and completely-closed lumina. Right: Definition of fibre dimensions.

To quantify the level of lumen collapse in wood fibres, several geometrical parameters have been defined. Figure 2.1 shows examples of open-lumen, partially-collapsed, and completely collapsed fibres. Sepke (1991) proposed that an aspect ratio $AR = D_{\text{min}}/D_{\text{max}}$ can characterize the degree of fibre collapse. As shown in Figure 2.1, D_{min} and D_{max} are defined as the shortest and longest external diameters of the fibre, respectively. Figure 2.1 also shows the fibre thickness and width. The aspect ratio parameter was used in several studies, such as Jang *et al.* (1995) and Yan & Li (2008). A decrease in AR indicates a more collapsed fibre.

Jang *et al.* (1995) defined another parameter as the ratio of the change in the lumen area to the initial lumen area LA_0. This parameter is termed collapse index $CI = 1 - LA/LA_0$, where LA is the final lumen areas. This index is more representative of the collapse behaviour as it only depends on the changes in the lumen area, whereas AR depends on the shape of the collapsed fibres (see Figure 2.1). For a completely-collapsed fibre, $CI = 1$, and for an uncollapsed fibre, $CI = 0$. Because CI completely neglects the shape of the fibre wall area, He *et al.* (2003) introduced a shape factor f_m, as the ratio of fibre wall area to the area of the smallest rectangle that completely engulfs the fibre cross section. This shape factor is maximum for completely-collapsed fibres, and minimum for open fibres.

2.3.2 Wood fibre flexibility

Fibre flexibility is defined as $F = 1/(EI)$ where E is Young's modulus and I is the area moment of inertia in the plane of bending. The fibre elastic modulus is affected by several factors, such as microfibril angle, pulping process, and moisture content. There are several methods to measure the fibre Young's modulus. Page *et al.* (1971) used a tensile test and showed that wood fibres twist when stretched, because of the helical microfibrils in their wall. Dulemba *et al.* (1999) measured the flexibility of a single fibre in three successive wetting and drying cycles by deflecting the fibres as a simply supported beam, and relating the deflection to the flexibility. They observed that chemical fibres become stiffer when recycled.

Another method to determine the elastic modulus of wood fibres is to press the fibres on a glass slide, and analyse their deformations at the crossing. Lowe *et al.* (2005) wet pressed two wood fibres and investigated the effect of mechanical and chemical treatments on the fibre properties, but the deformation of the top fibre was affected by the bottom fibre. To remove the effect of the bottom-fibre deformation, Yan & Li (2008) pressed a wood fibre on a glass fibre. However, the deformation is not completely controlled by the fibre longitudinal flexibility in this method.

Nilsson *et al.* (2000) tried to measure the conformability of the fibre surface using micro-indentation measurements with a standard atomic-force-microscopy tip and cantilever, but found a wide variability in the results even at different locations of the same fibre. Furthermore, the measured modulus in this method was one order of magnitude smaller than the other measurements.

Gindl & Schöberl (2004) modeled wood-fibre wall as a fibre-reinforced composite to analyse the effect of the microfibril angle on the elastic modulus. They showed that the transverse elastic modulus is one order of magnitude smaller than the longitudinal elastic modulus when the microfibril angle is small.

The effect of pulping process and the various mechanical and chemical treatments during papermaking on the elastic modulus has been extensively studied. For example, the elastic modulus of chemical-pulp fibres are smaller than mechanical-pulp fibres (Hubbe *et al.*, 2007). Dulemba *et al.* (1999) showed that recycling increases E in chemical pulps, while decreases it in mechanical pulps. Furthermore, Yan & Li (2008) showed that refining and bleaching significantly increase the flexibility of wet fibres.

The area moment of inertia in the fibre flexibility depends on the fibre wall thickness and diameter. Jang *et al.* (1996) observed that the fibre wall thickness is decreased by a 'peeling off' mechanism during pulping, while the fibre perimeter remains constant. Therefore, assuming a circular cross section, the fibre diameter can be considered constant during papermaking.

2.4 Capillary-induced collapse of circular tubes

Collapse of circular tubes driven by an external pressure has been studied for several decades (Moreno *et al.*, 1970; Kresch, 1977, 1979; Bertram, 1987), because of its importance in vein and lung-airway closure. However, capillary-induced collapse of a flexible circular tube was first studied by Halpern & Grotberg (1992), where a liquid film coated the inner surface of the tube, and the instability of the film forms a liquid bridge and buckles the tube. They calculated a critical liquid-film thickness above which a bridge is formed, showing that the tube flexibility reduces the required liquid volume to establish a liquid bridge by 30%. Heil (1999*a*,*b*) numerically studied the existence and stability of occluding liquid bridges in buckled elastic circular tubes, and proved that the capillary forces are strong enough to maintain the tubes in a buckled configuration. They claimed that the minimum fluid volume required for the bridge formation is much smaller than the values previously reported. Hazel & Heil (2005) showed that the initial tube buckling can lead to a rapid collapse that further reduces the required fluid volume. In all of these papers, the lung-airway closure is explained by either a purely fluid-mechanical film collapse or a coupled, fluid-elastic compliant collapse. Heil *et al.* (2008) proved that both mechanisms can be responsible for the lung-airway closure, and, therefore, surface tension is the main parameter that controls the phenomenon.

Jaron & Collicott (2008) studied a liquid-gas interface shape in a buckled initially-circular tube, and calculated the minimum energy states in a volume-contact angle parameter space. They analysed the morphologies of liquid drops or bridges at different locations of a buckled tube while neglecting the concave part of the buckled tube, and found the most energetically favoured configurations. In a dynamic approach, Heap & Juel (2009) experimentally investigated the bubble propagating in a strongly collapsed tube, and characterized the mechanisms controlling the transitions between different types of bubbles that migrate in a collapsed tube. The capillary-induced collapse of circular tubes has been recently analysed by using molecular dynamics simulations to analyze the buckling of carbon nanotubes (Yang *et al.*, 2010; Wu *et al.*, 2013).

2.5 Capillary forces between fibres

When a liquid droplet is deposited on a cylindrical filament, it forms either a barrel shape surrounding the filament or a clamshell shape holding to one side of the filament. Minor *et al.* (1959) reported that a droplet with a zero contact angle forms the barrel shape, while contact angles larger than $60°$ lead to the clamshell shape, and with an intermediate contact angle, both shapes are possible. They tried to measure the contact angle of the liquid droplets on the filament by a direct observation. Carroll (1976) calculated an analytical solution for the barrel shape when gravity effect is negligible. He calculated the drop shape, Laplace pressure, and interfacial areas, and proposed an accurate method for measuring contact angles. Wu & Dzenis (2006) further investigated this problem theoretically, and derived the governing equations and boundary conditions based on the free energy variation of the droplet-fibre system. In their approach, it is possible to include effects of other forces on the drop shape, and also to use the free energy functional directly in developing a finite element method.

McHale *et al.* (2001) and McHale & Newton (2002) used Carroll (1976) solution and a finite element solution for the clamshell shape to compare the interfacial energies of the two shapes, and calculate the transition boundaries when changing the liquid volume and contact angle. However, Chou *et al.* (2011) showed that in a specific range of parameters, both shapes coexist. They also showed that gravity brings the clamshell shape downward, and can make the drop to fall.

2.5.1 Parallel filaments

Minor *et al.* (1959) observed that a liquid droplet on a fibre array can form a barrel shape, which spreads and forms a liquid column at a critical separation. Princen (1969*a*,*b*, 1970) obtained an analytical solution for the liquid column between two or more equidistant parallel filaments when the column length is much greater than the filament radius. For the case of two horizontal filaments in the absence of gravity, they experimentally showed the coexistence of the barrel-shape droplet in a specific range of separation with a zero contact angle. Bedarkar *et al.* (2010) studied the dependency of the wetting length of both configurations on the contact angle, separation, and droplet volume. They observed that the sensitivity of this length to the parameters depends on the droplet morphology. In another study (Wu *et al.*, 2010), they also investigated the transition of the droplet between the barrel shape and liquid bridge morphologies, producing characteristic curves in a liquid volume-contact angle space that are separating the regions of the two configurations. In an experimental study, Protiere *et al.* (2013) showed that these transitions are hysteretic, and can be used to transfer liquid at a small scale. They identified the coexistence regions too.

Capillary forces caused by the liquid droplet in either morphology can deform flexible filaments and lead to new configurations of the droplet-filaments system. Duprat *et al.* (2012) experimentally studied the equilibrium and dynamic behaviour of a liquid droplet between flexible initially-parallel filaments, and determined the necessary conditions for the drop to remain compact or spread and make the filaments to coalesce. They produced a phase diagram separating the total spreading, partial spreading with a droplet at one end, and no spreading regimes. These regimes can be observed in many industrial and natural phenomena. In another study (Duprat *et al.*, 2013), they tried to use the various drop morphologies between either rigid or flexible filaments to control evaporation. They investigated the evaporation rate and the complex transitions that occur during the drying of a liquid droplet between two parallel filaments. However, the dynamic behaviour of the spreading regimes was studied mainly on flexible sheets rather than flexible filaments (Aristoff *et al.*, 2011; Duprat *et al.*, 2011; Gat & Gharib, 2013).

2.5.2 Crossing filaments

Claussen (2011) analytically calculated the liquid-column shape at the node of two crossing filaments by modifying the Princen (1970) solution, when the filaments have a small inclination angle, and the column length is much larger than the filament radius. He compared the scaling behaviour of this solution with a numerical solution, and characterized the capillary torque between the filaments as a power law that agrees well with the numerical results for a wide range of crossing angles. The analytical solution was later used by Sauret *et al.* (2014) to justify their experimental observations on the various liquid-drop morphologies at the node of two crossing filaments: a liquid column, a mixed morphology consists of a drop at the end of a column, and a liquid drop at the node. With the modified Princen model, they could successfully calculate the critical column length where the symmetry breaks to form a mixed configuration. In their analysis, they could also capture the second transition to the single drop morphology by comparing the total interfacial energies. These transitions were later used by Boulogne *et al.* (2015) to enhance the evaporation rate in a fibrous media by shearing the network of fibres to reduce the crossing angles.

However, there is no analytical solution for a drop shape at the node of two crossing filaments with a large inclination angle. Therefore, numerical solutions have been used to investigate the drop morphology, Laplace pressure, and capillary force and torque on the filaments. Claussen (2011) qualitatively described the two possible droplet configurations at the node: a liquid bridge and a barrel-shape droplet. Nevertheless, the transition between these configurations has never been quantitatively analysed. Virozub *et al.* (2009) numerically calculated the interface shape of a liquid bridge between the filaments with various separation, contact angle, inclination angle, and liquid volume, and calculated the capillary force and torque on the filaments with a finite differences method. They observed that with a large separation, the capillary force is attractive and the bridge is symmetric and stable. However, with a large contact angle, a reduction in the separation may lead to a repulsive force, and a new stable asymmetric equilibrium with a near-zero force.

Furthermore, the previous symmetric solution may become unstable when decreasing the separation. In another study, Bedarkar & Wu (2009) calculated the capillary torques with a similar method, but without considering the asymmetric solutions. They observed that the capillary torque increases as the crossing angle increases, and after showing a maximum, vanishes at 90° crossing angles. The torque decreases when increasing contact angle and separation.

2.5.3 Capillary forces between wood fibres

The capillary forces caused by the liquid bridges between wood fibres in a wet paper sheet were considered as the main explanation of wet-paper strength for decades (Campbell, 1933). However, van de Ven (2008) showed that fibre entanglements is likely to significantly affect the wet strength. He suggested that above 40% solid content, almost all of the water in a wet paper is either in the fibre wall or in the liquid bridges at the fibre crossings. He then calculated the maximum capillary force between two wet sheets which was in fair agreement with experimental results, but the same model failed to predict the wet web strength indicating the importance of the fibre entanglements. Tejado & van de Ven (2010) proved that the main explanation for wet-paper strength is the fibre entanglements, rather than the capillary forces.

Another impact of the capillary forces between wood fibres is to pull the fibres into molecular proximity during drying. Wet fibres are much more flexible than dry fibres, and can be readily deformed by the capillary forces without storing much elastic energy. Persson *et al.* (2013) studied the surface topography of paper fibres using atomic force microscopy to measure the effective elastic modulus and the penetration hardness as a function of relative humidity. They concluded that for a good contact in a dry state, fibres break and reform their hydrogen bonds to conform their surfaces to each other, which further strengthens the capillary interaction and hydrogen bonding. This conformation is driven in part by the capillary forces between the fibres.

Chapter 3

Bubbles and drops on curved surfaces

3.1 Preface

The following Chapter is focused on the first objective of this thesis, which is the shape of a liquid droplet or a gas bubble located either inside or outside of a circular tube that mimics wood fibres. I present an analytical approximation for the shape, Laplace pressure, and surface energy of a droplet on a curved surface, and then, apply this general solution to a droplet on a circular tube. The substrate-curvature impact on the droplet shape, pressure, and energy is discussed, and a droplet migration induced by a substrate-curvature gradient is predicted.

3.2 Abstract

Surface curvature affects the shape, stability, and apparent contact angle of sessile and pendant drops. Here, I develop an approximate analytical solution for non-axisymmetric perturbations to small spherical drops on a flat substrate, assuming a fixed contact angle and fixed drop volume. The analytical model is validated using numerical solutions of the Laplace equation from the Surface Evolver software. I investigate the surface-curvature effects on drop shape, pressure, and surface energy, ascertaining the energy-gradient force that drives lateral drop migration. By balancing this force with the viscous resistance/drag force, in the lubrication approximation, velocities of the order 0.1 mm s^{-1} are predicted for 1 mm diameter drops of water with a 30° contact angle on a substrate with a curvature gradient 0.01 mm^{-2}, achieved, for example, on an harmonic surface with wavelength 4 cm

and amplitude 4 mm.

3.3 Introduction

Bubbles and drops on curved surfaces are ubiquitous in technological applications and in Nature. Their shapes are controlled by wettability, which depends on the chemical and physical properties of the substrate and its morphology. Because of its numerous applications (de Gennes *et al.*, 2004), wettability analysis by means of drop morphology has been the subject of many studies (Piao *et al.*, 2010). For example, numerical and experimental methods have been described for contact-angle measurement of heterogeneous curved surfaces by extending the axisymmetric approximation for drop shape, since traditional contact-angle measurements are restricted to flat, ideal, horizontal surfaces.

Iliev & Pesheva (2006) proposed a numerical method to specify the local contact angle of a drop when the contact line is known for a given drop volume and capillary length. Guilizzoni (2011) experimentally explored the shapes and contact angles of drops on curved surfaces using image processing, spline fitting, and numerical integration, extracting the drop contour in a number of cross-sections. This procedure requires only a side view, and can be used for fluids with unknown surface tension, without need to measure the drop volume. However, recent investigations by Extrand & Moon (2008) showed that substrate curvature does not affect the intrinsic contact angle. They deposited small liquid drops at the apex of polymer spheres to analyze the wetting of structured surfaces with spherical or cylindrical features, concluding that the intrinsic contact angles are the same as on flat, horizontal surfaces.

Another influence of substrate curvature is to impart a topological change in the interface configuration. Eral *et al.* (2011*a*) experimentally and analytically studied the equilibrium morphology of a drop on a sphere as a function of the contact angle and drop volume. They used electrowetting to precisely control the wetting parameters, which allowed all equilibrium morphologies to be accessed. This showed that the partially engulfing morphology is energetically more favourable than the spherically symmetric, completely engulfing morphology, as proved earlier by Smith & van de Ven (1981). Other examples of bubbles and drops on curved surfaces occur in elastocapillarity (Duprat *et al.*, 2012; Yang *et al.*, 2010; Py *et al.*, 2009, 2007), fog harvesting (Park *et al.*, 2013), electrowetting (García-Sánchez *et al.*, 2010; Mugele, 2009), and electrodeposition (Tsai *et al.*, 2002) processes.

For a liquid-gas interface to be at equilibrium, there are two hydrostatic conditions that must be satisfied simultaneously (Myshkis *et al.*, 1987). The first is the Laplace condition, which requires that the pressure jump across a liquid-gas interface is equal to the product of the interfacial tension γ and the mean curvature $2H$:

$$p_0 - p = 2H\gamma = \gamma\left(\frac{1}{R_1} + \frac{1}{R_2}\right), \tag{3.1}$$

where R_1 and R_2 are the principal radii of curvature, and p and p_0 are the liquid and gas pressures. The second is the Dupré-Young condition at the contact line:

$$\gamma \cos\alpha = \gamma_{sg} - \gamma_{sl}, \tag{3.2}$$

where γ_{sl} and γ_{sg} are the solid-liquid and solid-gas interfacial tensions, and α is the equilibrium contact angle. Equation (3.2) gives (Myshkis *et al.*, 1987)

$$\vec{n}_i \cdot \vec{n}_s = \cos\alpha, \tag{3.3}$$

where $\vec{n}_i$ and $\vec{n}_s$ are the unit normal vectors on the interface and substrate, respectively. The equilibrium shape is obtained by solving Eqn. (3.1) with Eqn. (3.3) and a prescribed volume and substrate shape.

Perturbation methods are useful in many capillary problems (Prabhala *et al.*, 2010; Carroll, 1986; O'Brien, 1991; Srinivasan *et al.*, 2011; Chesters, 1977). A notable analysis closely related to the present study was undertaken by Myshkis *et al.* (1987) They derived perturbation equations for a general interface by perturbing all the relevant parameters. However, because the final set of differential equations is very complicated, they demonstrated existence conditions and a general solution form, not an exact solution.

Although many studies have addressed drop- or bubble-shape analysis on curved surfaces, no analytical solution has been derived for non-axisymmetric curved surfaces that furnishes their profiles, internal pressure, and interfacial energy. Here, I propose a general solution for the equilibrium drop shape on a curved surface in the absence of gravity. One motivation is to understand the elastocapillary driven wood-fibre deformation during drying. As wood fibres dry, bubbles or drops form in the lumen or between entangled fibres (Walker, 2006). The capillary pressure may play a key role in the fibre deformation, and it substantially affects fibre strength and conformation (van de Ven, 2008; Hu & Hsieh, 2001). Here, I assess the effect of surface curvature on the drop shape, internal pressure, and surface energy. The results might be used to identify conditions that change an open lumen to a flattened structure upon drying.

I consider a spherical drop on a flat surface, which I perturb to compute the resulting drop shape. The new interface and contact line are obtained by solving Eqn. (3.1) while satisfying Eqn. (3.3) at constant volume. The solution has a singularity that I remove by restructuring the solution and matching the new form to the original one at the boundary of the problematic neighbourhood. This solution is then applied to a drop inside or outside a circular tube, and verified numerically using the Surface Evolver software (Brakke, 1992). The resulting interface shape, drop pressure, and energy match the numerical computations well for all contact angles, even for large values of the perturbation parameter. Since the energy changes with the substrate curvature, drops are expected to migrate to positions of lowest energy. This possibility is studied theoretically, and verified with Surface Evolver for a drop on an harmonic surface. I estimate the lateral velocity by balancing the lateral energy-gradient force with the viscous resistance force, in the lubrication approximation.

3.4 Theory

Consider a spherical fluid-fluid interface on a planar supporting substrate with a 3-phase contact angle α, as shown in Figure 3.1. The origin O is at the sphere centre, and the distances are scaled with the sphere radius R_0.

In cylindrical coordinates (r, θ, z), the interface is

$$z(r) = \pm\sqrt{1 - r^2}, \tag{3.4}$$

and the substrate is

$$z_0 = -\cos\alpha. \tag{3.5}$$

For a flat surface, the contact line is a circle,

$$r = \sin\alpha, \quad z = -\cos\alpha \tag{3.6}$$

and the volume enclosed by the interface and the support is obtained by integrating

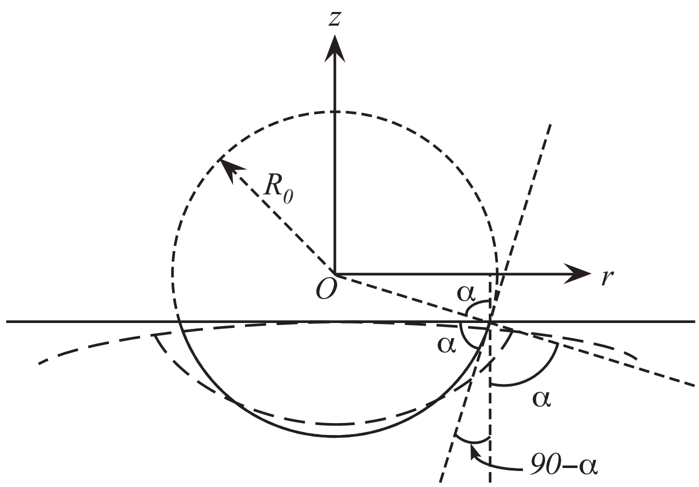

Figure 3.1: Perturbation (dashed curves) of an initially spherical drop on an initially flat substrate (solid curves).

Eqns. (3.4) and (3.5), giving

$$V = \frac{2\pi}{3}\left(1 - \cos^3\alpha - \frac{3}{2}\sin^2\alpha\cos\alpha\right). \tag{3.7}$$

Now I perturb the substrate by adding a disturbance to Eqn. (3.5), giving

$$z_0 = -\cos\alpha + \epsilon h(r,\theta), \tag{3.8}$$

where ϵ is the perturbation parameter, θ is the azimuthal coordinate, and

$$h(r,\theta) = A_0(r) + \sum_{n=1}^{\infty}[A_n(r)\cos(n\theta) + B_n(r)\sin(n\theta)]. \tag{3.9}$$

Note that $h(r,\theta)$ is continuous at $r = 0$, and $A_{n,r}(r)$, $B_{n,r}(r)$, $nA_n(r)$, and $nB_n(r)$ are $O(1)$ with the subscripts r and θ denoting partial derivatives. Because of the substrate perturbation, the contact line deviates from a circle. I approximate the perturbed contact line by adding a perturbation to Eqn. (3.6),

$$r = \sin\alpha + \epsilon f(\theta), \quad z = -\cos\alpha + \epsilon h(r,\theta) \tag{3.10}$$

where $f(\theta)$ has the same form as Eqn. (3.9). Similarly, the interface deviates from a sphere.

If $\alpha \leq \pi/2$, then

$$z(r,\theta) = -\sqrt{1-r^2} + \epsilon g(r,\theta), \tag{3.11}$$

where

$$g(r,\theta) = \xi_0(r) + \sum_{n=1}^{\infty} [\xi_n(r)\cos(n\theta) + \eta_n(r)\sin(n\theta)]. \tag{3.12}$$

Here, I must specify the functions $\xi_n(r)$ and $\eta_n(r)$ using the known functions $A_n(r)$ and $B_n(r)$, and by solving Eqn. (3.1) with appropriate boundary conditions. From Eqn. (3.1), the mean curvature in cylindrical coordinates when $z = z(r,\theta)$ is (Langbein, 2002)

$$\frac{\frac{1}{r}\frac{\partial}{\partial r}(r z_r)\left[1+\left(\frac{z_\theta}{r}\right)^2\right] + \frac{z_r}{r}\left[{z_r}^2 - 2\frac{z_\theta}{r} z_{r\theta} + \left(\frac{z_\theta}{r}\right)^2\right] + \frac{z_{\theta\theta}}{r^2}(1+{z_r}^2)}{\left[1+{z_r}^2+\left(\frac{z_\theta}{r}\right)^2\right]^{\frac{3}{2}}} = 2H. \tag{3.13}$$

Since the drop pressure is a constant that depends only on the mean interfacial curvature, the perturbed curvature is

$$H = 1 + \epsilon\frac{k}{2}\ . \tag{3.14}$$

Substituting Eqns. (3.11) and (3.14) into Eqn. (3.13), and retaining only the terms up to order ϵ gives

$$(r^4 - r^2)g_{rr} + (4r^3 - r)g_r - g_{\theta\theta} = \frac{kr^2}{\sqrt{1-r^2}}. \tag{3.15}$$

Now, since $\{\sin(n\theta), \cos(n\theta)\}$ is a complete orthogonal system, from Eqns. (3.12) and (3.15),

$$\begin{aligned} (r^4-r^2)\xi_{0,rr} + (4r^3-r)\xi_{0,r} &= \tfrac{kr^2}{\sqrt{1-r^2}}, \\ (r^4-r^2)\xi_{n,rr} + (4r^3-r)\xi_{n,r} + n^2\xi_n &= 0, \\ (r^4-r^2)\eta_{n,rr} + (4r^3-r)\eta_{n,r} + n^2\eta_n &= 0, \end{aligned} \tag{3.16}$$

which must be solved with a constant volume, specified substrate shape, and the Dupré-Young condition. To satisfy Eqn. (3.3), I calculate the perturbed substrate and interface normal vectors,

$$\begin{aligned} \vec{n}_s &= \left[\epsilon h_r(r,\theta), \epsilon\frac{h_\theta(r,\theta)}{r}, -1\right] + O(\epsilon^2), \\ \vec{n}_i &= \left[r + \epsilon g_r(r,\theta)\,(1-r^2)^{\frac{3}{2}}, \epsilon\frac{\sqrt{1-r^2}}{r} g_\theta(r,\theta), -\sqrt{1-r^2} + \epsilon r g_r(r,\theta)(1-r^2)\right] + O(\epsilon^2), \end{aligned} \tag{3.17}$$

where $h_r(r,\theta)$ and $h_\theta(r,\theta)$ are assumed to be $O(1)$, furnish additional conditions on $A_n(r)$ and $B_n(r)$. Satisfying Eqn. (3.3) at the perturbed contact line, which is given in Eqn. (3.10), and using Eqn. (3.17) gives

$$f(\theta) = \cos\alpha\ h_r(\sin\alpha,\theta) - \cos^3\alpha\ g_r(\sin\alpha,\theta). \tag{3.18}$$

Another boundary condition comes from the specified substrate shape. At the contact line, the interface and the substrate intersect, requiring

$$z\left[\sin\alpha + \epsilon f(\theta),\theta\right] = z_0\left[\sin\alpha + \epsilon f(\theta),\theta\right]. \tag{3.19}$$

Substituting Eqns. (3.8) and (3.11) into Eqn. (3.19), and using Eqn. (3.18) gives

$$-\sin\alpha\cos^2\alpha g_r(\sin\alpha,\theta) + g(\sin\alpha,\theta) = h(\sin\alpha,\theta) - \sin\alpha h_r(\sin\alpha,\theta). \tag{3.20}$$

Then, substituting Eqns. (3.9) and (3.12) into Eqn. (3.20) furnishes the boundary conditions for Eqn. (3.16):

$$\begin{aligned} -\sin\alpha\cos^2\alpha\xi_{n,r}(\sin\alpha) + \xi_n(\sin\alpha) &= A_n(\sin\alpha) - \sin\alpha A_{n,r}(\sin\alpha),\\ -\sin\alpha\cos^2\alpha\eta_{n,r}(\sin\alpha) + \eta_n(\sin\alpha) &= B_n(\sin\alpha) - \sin\alpha B_{n,r}(\sin\alpha). \end{aligned} \tag{3.21}$$

Using Eqn. (3.21) and demanding finite $g(0,\theta)$, the solution of Eqn. (3.16) is available in appendix A, giving

$$g(r,\theta) = C_0 + \frac{k}{2\sqrt{1-r^2}} + \sum_{n=2}^{\infty}\left\{\frac{\left(n+\sqrt{1-r^2}\right)\left[2(1-\sqrt{1-r^2})-r^2\right]^{\frac{n}{2}}}{r^n\sqrt{1-r^2}}\left[C_n\cos(n\theta) + D_n\sin(n\theta)\right]\right\}, \tag{3.22}$$

where

$$\begin{aligned} C_0 &= A_0(\sin\alpha) - \sin\alpha A_{0,r}(\sin\alpha) - \frac{k}{2}\cos\alpha,\\ C_n &= \frac{\left[A_n(\sin\alpha) - \sin\alpha A_{n,r}(\sin\alpha)\right]\sin^n\alpha}{(1-n^2)\left[2(1-\cos\alpha)-\sin^2\alpha\right]^{\frac{n}{2}}},\\ D_n &= \frac{\left[B_n(\sin\alpha) - \sin\alpha B_{n,r}(\sin\alpha)\right]\sin^n\alpha}{(1-n^2)\left[2(1-\cos\alpha)-\sin^2\alpha\right]^{\frac{n}{2}}}. \end{aligned} \tag{3.23}$$

In Eqn. (3.22), the first harmonic is not included because the equilibrium condition precludes satisfying the Laplace and Dupré-Young conditions simultaneously. The first mode has previously been excluded in the contact-line perturbation (Prabhala *et al.*, 2010) and contact-angle perturbations (Popova, 1983).

The only remaining unknown is the perturbation to the mean curvature (or pressure), which requires specifying k. With constant volume

$$\begin{aligned} V = &\int_0^{2\pi}\int_0^{\sin\alpha+\epsilon f(\theta)}\left[-\sqrt{1-r^2}+\epsilon g(r,\theta)\right] r\mathrm{d}r\mathrm{d}\theta \\ &-\int_0^{2\pi}\int_0^{\sin\alpha+\epsilon f(\theta)}\left[-\cos(\alpha)+\epsilon h(r,\theta)\right] r\mathrm{d}r\mathrm{d}\theta, \end{aligned} \tag{3.24}$$

Eqns. (3.7) and (3.24) give

$$k = \frac{-2\int_0^{\sin\alpha} A_0(r)rdr + \sin^2\alpha\left[A_0(\sin\alpha) - \sin\alpha A_{0,r}(\sin\alpha)\right]}{\cos\alpha - 1 + \frac{1}{2}\sin^2\alpha\cos\alpha}. \tag{3.25}$$

The solution is now complete for $\alpha \leq \pi/2$, but as $r \to 1$, Eqn. (3.22) becomes singular. Therefore, to remove this singularity, I bring the singular part under the square root, giving

$$z = -\sqrt{1 - r^2 + \epsilon\gamma_1(r,\theta) + \epsilon^2\gamma_2(r,\theta)} + \epsilon\gamma_3(r,\theta), \tag{3.26}$$

where γ_1 to γ_3 are found by matching Eqns. (3.22) and (3.26). This new form is then used in the interval $[1-\epsilon, r_{max}]$, which is illustrated as region 2 in Figure 3.2. Almost the same technique was used by Chesters (1977), but they did not keep the second-order term under the square root. This may not be correct, because at the maximum value of r the imaginary part of z is $O(\epsilon)$, and cannot be neglected. After matching Eqns. (3.22) and (3.26) at $r = 1 - |\epsilon|$ (see appendix B), I find

$$\begin{aligned} F(r,\theta) &= \tfrac{k}{2} + \sum_{n=2}^{\infty}\left\{nr^{-n}\left[C_n\cos(n\theta) + D_n\sin(n\theta)\right]\right\}, \\ \gamma_1(r,\theta) &= -2F + \tfrac{F^2}{2}\mathrm{sgn}(\epsilon), \quad \gamma_2(r,\theta) = \tfrac{F^2}{4}, \\ \gamma_3(r,\theta) &= C_0 + \sum_{n=2}^{\infty}\left\{r^{-n}(2-r^2)^{\frac{n}{2}-1}\left(2-r^2-n^2\right)\left[C_n\cos(n\theta) + D_n\sin(n\theta)\right]\right\}. \end{aligned} \tag{3.27}$$

If $\sin\alpha > 1-|\epsilon|$, then the contact line is in the interval $[1-|\epsilon|, r_{max}]$. Setting $\alpha = \pi/2 - |\epsilon|\beta$ gives

$$\sin\alpha = 1 - \frac{1}{2}\epsilon^2\beta^2 \quad \text{and} \quad \cos\alpha = \epsilon\beta, \tag{3.28}$$

so from Eqn. (3.3) I find the contact line equation in this interval

$$r = 1 + \epsilon\frac{\gamma_1(1,\theta)}{2} - \frac{1}{2}\epsilon^2\left\{[\beta\ \mathrm{sgn}(\epsilon) - h_r(1,\theta)]^2 - \gamma_2(1,\theta) + \frac{\gamma_1(1,\theta)^2}{4}\right\}. \tag{3.29}$$

For contact angles $\alpha > \pi/2$, there is little change in the equations when passing the $z = 0$ plane, since the mean curvature and the right-hand side of Eqn. (3.4) change sign there. Accordingly, there are two solutions that must match at r_{max}. I apply the same procedure above for $\alpha > \pi/2$, furnishing drop shapes for all contact angles. Depending on the contact angle, I divide the problem into four separate cases (Figure 3.2), since the drop-shape equation varies near $r = 1$, and the contact-line equation should be adapted correspondingly. When $\alpha > \pi/2$, for regions 1 and 4,

$$\begin{aligned} g(r,\theta) =& C_0 \pm \frac{k}{2\sqrt{1-r^2}} \\ & \pm \sum_{n=2}^{\infty}\left\{\frac{\left(n \pm \sqrt{1-r^2}\right)\left(2(1 \mp \sqrt{1-r^2}) - r^2\right)^{\frac{n}{2}}}{r^n\sqrt{1-r^2}}[C_n\cos(n\theta) + D_n\sin(n\theta)]\right\}, \end{aligned} \tag{3.30}$$

where the top sign (in the pair $\pm$ or $\mp$) identifies region 1 and the bottom sign identifies region 4 [k, C_0, C_n, D_n are defined in Eqns. (3.23) and (3.25)]. For regions 2 and 3,

$$z = \mp\sqrt{1 - r^2 + \epsilon\gamma_1(r,\theta) + \epsilon^2\gamma_2(r,\theta)} + \epsilon\gamma_3(r,\theta), \tag{3.31}$$

where the top sign identifies region 2 and the bottom sign identifies region 3 with the same γ_1, γ_2, and γ_3 as in Eqn. (3.27). The maximum value of r for cases 3 and 4 is

$$r_{max} = 1 + \epsilon\frac{\gamma_1(1,\theta)}{2} + \epsilon^2\left[\frac{\gamma_2(1,\theta)}{2} - \frac{\gamma_1(1,\theta)^2}{8}\right]. \tag{3.32}$$

3.4.1 Energy

In the absence of gravity, the total energy is the surface energy

$$\begin{aligned} E &= \gamma A_{lg} + \gamma_{sg}A_{sg} + \gamma_{sl}A_{sl} \\ &= \gamma A_{lg} - \gamma A_{sl}\cos\alpha + \text{const.} \end{aligned} \tag{3.33}$$

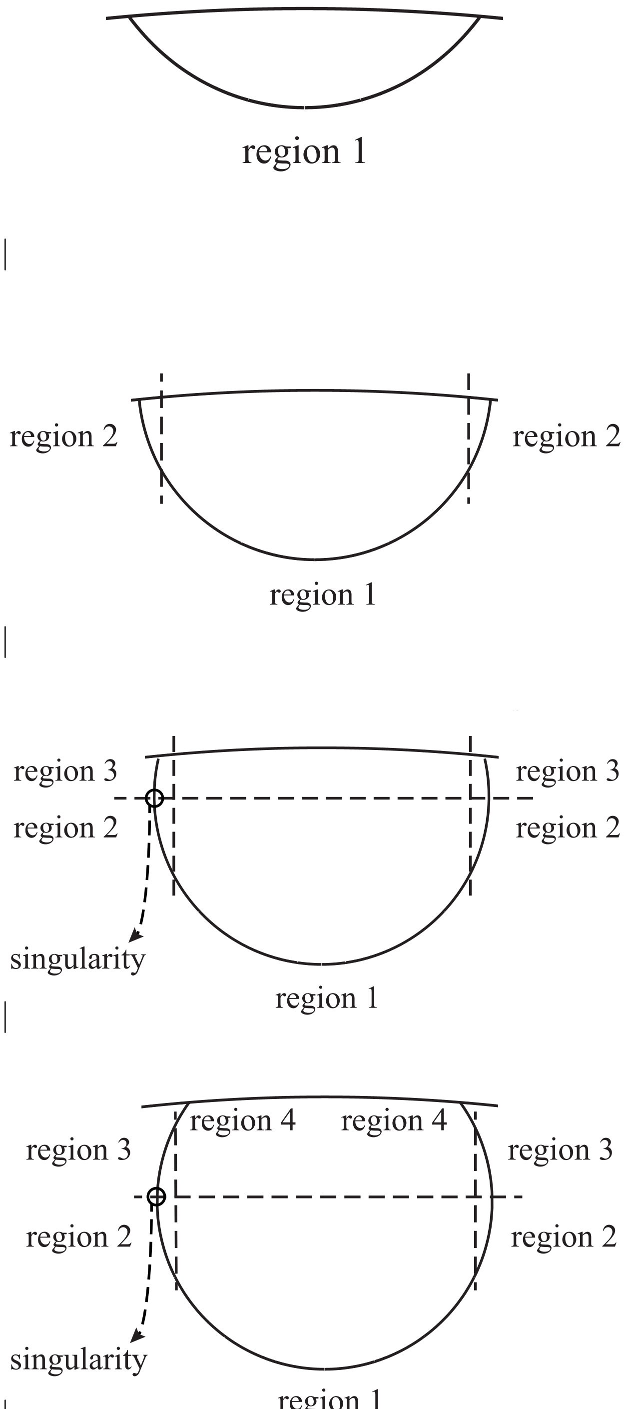

Case 1: $\alpha < \pi/2, \sin\alpha < 1 - |\epsilon|$

Case 2: $\alpha < \pi/2, \sin\alpha > 1 - |\epsilon|$

Case 3: $\alpha > \pi/2, \sin\alpha > 1 - |\epsilon|$

Case 4: $\alpha > \pi/2, \sin\alpha < 1 - |\epsilon|$

Figure 3.2: Configurations for various contact angles; small circles identify singularities at $r = 1$.

where subscripts sg, sl, and lg denote solid-gas, solid-liquid, and liquid-gas interfaces, respectively. With

$$S(r,\theta,z) = z \pm \sqrt{1-r^2} - \epsilon g(r,\theta) = 0, \tag{3.34}$$

$$\phi(r,\theta,z) = z + \cos\alpha - \epsilon h(r,\theta) = 0, \tag{3.35}$$

I have

$$A_{lg} = \int_0^{2\pi}\int_0^{\sin(\alpha)+\epsilon f(\theta)} \frac{|\nabla S|}{|\nabla S\cdot \mathbf{e}_z|} r\mathrm{d}r\mathrm{d}\theta, \tag{3.36}$$

$$A_{sl} = \int_0^{2\pi}\int_0^{\sin(\alpha)+\epsilon f(\theta)} \frac{|\nabla \phi|}{|\nabla \phi\cdot \mathbf{e}_z|} r\mathrm{d}r\mathrm{d}\theta, \tag{3.37}$$

which become

$$A_{lg} = 2\pi\left(1-\cos\alpha\right) + 2\pi\epsilon\left[-k\left(1-\cos\alpha\right) + \sin\alpha A_{0,r}(\sin\alpha)\right] + O(\epsilon^2), \tag{3.38}$$

$$A_{sl} = \pi\sin^2\alpha + 2\pi\epsilon\left[-\frac{k}{2}\sin\alpha + \cos\alpha A_{0,r}(\sin\alpha)\right] + O(\epsilon^2), \tag{3.39}$$

so the total energy (to within an arbitrary constant) from Eqn. (3.33) is

$$\frac{E}{\gamma R_0^2} = 2\pi\left(1-\cos\alpha - \frac{1}{2}\cos\alpha\sin^2\alpha\right) + 2\pi\epsilon\left[-2\int_0^{\sin\alpha} A_0(r)r\mathrm{d}r + \sin^2\alpha A_0(\sin\alpha)\right]. \tag{3.40}$$

3.4.2 Application to circular tubes

As an example, I consider the perturbation of spherical drop on a plane that is deformed into a cylinder, as shown in Figure 3.1. In Cartesian coordinates, the cylinder surface is described by

$$\left(z \pm R + R_0\cos\alpha\right)^2 + x^2 = R^2, \tag{3.41}$$

where R is the cylinder radius. Scaling with the drop radius R_0,

$$\left(z - \frac{1}{\epsilon} + \cos\alpha\right)^2 + x^2 = \left(\frac{1}{\epsilon}\right)^2, \tag{3.42}$$

where, in this example, $\epsilon = R_0/R$ with $|\epsilon| \ll 1$. Note that $\epsilon < 0$ (> 0) implies that the drop is inside (outside) the tube. Now I write Eqn. (3.42) explicitly in z, linearize it in ϵ, and transform to cylindrical coordinates, giving

$$z_0 = -\cos\alpha + \epsilon\left\{\frac{1}{4}r^2\left[1+\cos(2\theta)\right]\right\}. \tag{3.43}$$

Comparing Eqns. (3.8) and (3.43) furnishes $A_0(r)$ and $A_2(r)$, and from Eqns. (3.22), (3.26), (3.30), and (3.31) I find (see Figure 3.2)

- region 1:

$$z(r,\theta) = -\sqrt{1-r^2} + \epsilon\left\{C_0 + \frac{k}{2\sqrt{1-r^2}} + C_2\left[\frac{2}{r^2\sqrt{1-r^2}} - \frac{2}{r^2} - 1\right]\cos(2\theta)\right\}, \tag{3.44}$$

- region 2:

$$z = -\sqrt{1-r^2+\epsilon\gamma_1(r,\theta)+\epsilon^2\gamma_2(r,\theta)} + \epsilon\gamma_3(r,\theta), \tag{3.45}$$

- region 3:

$$z = \sqrt{1-r^2+\epsilon\gamma_1(r,\theta)+\epsilon^2\gamma_2(r,\theta)} + \epsilon\gamma_3(r,\theta), \tag{3.46}$$

- region 4

$$z(r,\theta) = \sqrt{1-r^2} + \epsilon\left\{C_0 - \frac{k}{2\sqrt{1-r^2}} - C_2\left[\frac{2}{r^2\sqrt{1-r^2}} + \frac{2}{r^2} + 1\right]\cos(2\theta)\right\}, \tag{3.47}$$

where

$$\begin{aligned} C_0 =& -\frac{1}{4}\sin^2\alpha - \frac{k}{2}\cos\alpha, \\ C_2 =& \frac{\sin^4\alpha}{24(1-\cos\alpha) - 12\sin^2\alpha}, \\ k =& \frac{-3\sin^4\alpha}{4\left(2\cos\alpha - 2 + \sin^2\alpha\cos\alpha\right)}, \end{aligned} \tag{3.48}$$

and

$$\begin{aligned}
\gamma_1(r,\theta) =& -k - \frac{4C_2}{r^2}\cos(2\theta) + \frac{1}{2}\left[\frac{1}{2} + \frac{2C_2}{r^2}\cos(2\theta)\right]^2 \operatorname{sgn}(\epsilon), \\
\gamma_2(r,\theta) =& \frac{1}{4}\left[\frac{k}{2} + \frac{2C_2}{r^2}\cos(2\theta)\right]^2, \\
\gamma_3(r,\theta) =& C_0 - \left(\frac{2}{r^2} + 1\right) C_2 \cos(2\theta).
\end{aligned} \tag{3.49}$$

3.4.3 Numerical solution

I verified the foregoing analytical approximation using the public domain Surface Evolver software, which is for studying equilibrium surfaces shaped by surface tension. From a user-defined initial guess of the shape, the program advances the surface to lower energy states by displacing mesh vertices. The user can progressively refine the mesh to achieve a desired accuracy. Details of the algorithm and the program implementation are available in the user manual (Brakke, 2008).

For a drop inside or outside a circular tube, Surface Evolver computes the equilibrium interface with a fixed volume [Eqn. (3.7)] and zero density. For example, from a pyramid as the initial shape, with one of the faces restricted to the tube wall, computations converged to 9 significant digits in the total energy using 20480 facets. An analysis demonstrating first-order convergence of the energy with respect to the number of facets is available in appendix C. Moreover, I demonstrate, using the pressure perturbation, that the analytical approximation has errors that are $O(\epsilon^2)$. Drop shapes for two representative examples are shown in Figure 3.3. Quantitative comparisons with the analytical theory are examined below.

3.5 Results

Drop profiles in the tube cross section are shown in Figure 3.4 (top) for $\epsilon = -0.1$ and -0.3 with $\alpha = 60°$. When $\epsilon = -0.3$, there is a non-smooth transition between the regions 1 and 2 in Figure 3.2, and the perturbation solution deviates from the numerics. Because of the larger errors in the contact-line calculation, the drop profile and the substrate do not match well at the contact line. Note that $|\epsilon| = 0.3$ is a large absolute value for the perturbation parameter, and I do not expect to obtain the same correspondence when increasing ϵ. For

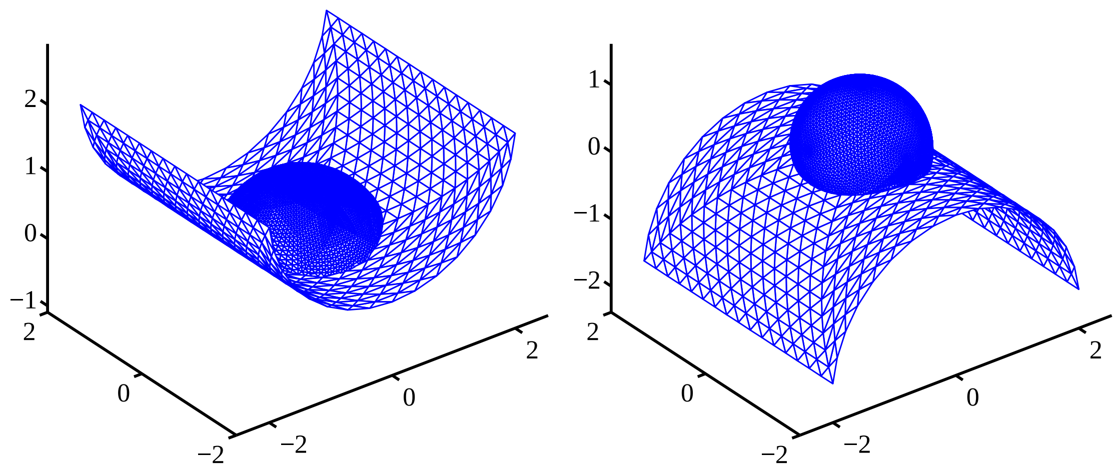

Figure 3.3: Drop shapes from Surface Evolver with $\alpha = 90°$, and $\epsilon = -0.5$ (left) and 0.5 (right).

$\epsilon = -0.1$, the transition is smooth, and inward bending of the surface stretches the drop normal to the tube axis, also compressing it along the tube axis. Drop profiles in the tube cross section with constant surface curvature and several contact angles are shown in Figure 3.4 (middle). Similarly to the top panel, where $\epsilon = -0.1$ for both hydrophobic and hydrophilic surfaces, the transitions between regions are smooth. Displacement profile scaled with ϵ, i.e., $g(r, \theta)$ from Eqn. (3.11) are shown in Figure 3.4 (bottom). For small ϵ, the numerical solution corresponds well with the perturbation solution, deviating gradually when increasing $|\epsilon|$. However, even with $\epsilon = -0.5$, the difference is small compared to $g(r, \theta)$.

Next, I compare the numerical and perturbation approximations of the pressure and energy. As explained in the theory Section, the pressure difference across the interface changes with the substrate curvature, and this change is equal to $k(\alpha)\epsilon$ with $k(\alpha)$ given by Eqn. (3.25). Note that k only depends on the axisymmetric part of the perturbation $A_0(r)$, since the other terms are periodic in θ, and vanish when integrated with respect to θ from 0 to 2π when calculating the drop volume. Thus, the non-axisymmetric part of the perturbation does not change the internal pressure. Figure 3.5 (right panel) compares $k(\alpha)\epsilon$ to Surface Evolver computations with three contact angles. Note that the internal pressure increases with substrate curvature when the drop is outside the tube, and decreases when it is inside the tube. Accordingly, because the interface curvature and the internal pressure

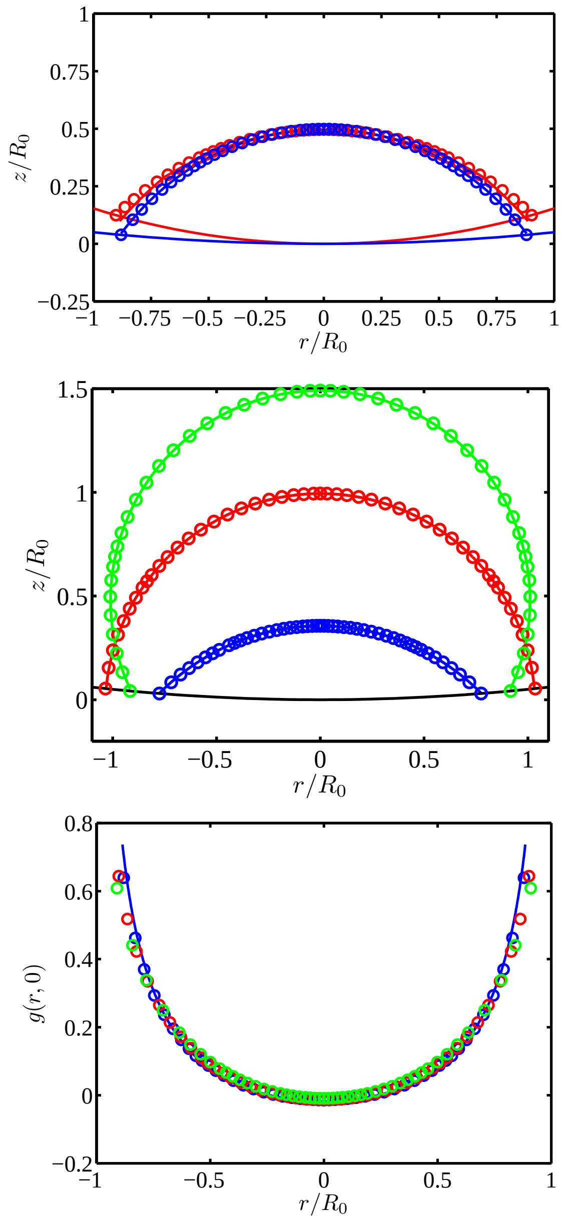

Figure 3.4: (top) Drop profiles with $\alpha = 60°$, and $\epsilon = -0.1$ (blue) and -0.3 (red). (middle) Drop profiles with $\alpha = 50°$ (blue), $90°$ (red) , $120°$ (green), and $\epsilon = -0.1$. (bottom) Scaled surface-displacement perturbation profile with $\alpha = 50°$, and $\epsilon = -0.1$ (blue), -0.3 (red), -0.5 (green). (symbols are from Surface Evolver, and lines are the perturbation approximation)

are related by Eqn. (3.1), the drop curvature increases when the drop is outside the tube, and decreases when it is inside the tube. When $\epsilon = 0$, the drop is spherical, and the three lines in Figure 3.5 intersect.

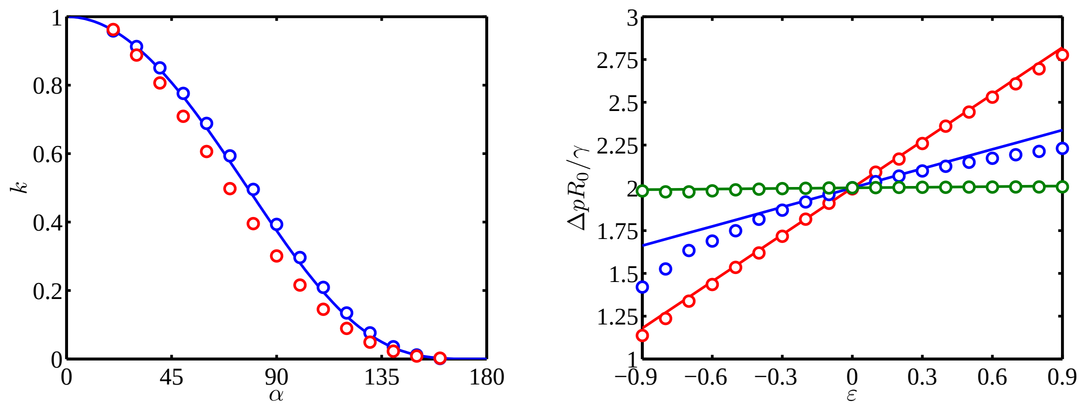

Figure 3.5: (left) Scaled pressure perturbation (k from Eqn 3.48) versus contact angle. Symbols are from Surface Evolver with $\epsilon = -0.1$ (blue) and 0.5 (red), and the line is the perturbation approximation. (right) Scaled internal drop pressure versus aspect ratio (symbols are from Surface Evolver, and lines are the perturbation approximation) with $\alpha = 30°$ (red), $90°$ (blue), $150°$ (green).

While the slopes of the lines in the right panel of Figure 3.5 equal k, and are independent of ϵ, they vary with contact angle. Figure 3.5 (left panel) compares the perturbation approximation of k with Surface Evolver computations with curvatures $\epsilon = -0.1$ and 0.5. Here, the theory agrees well with the numerics for all contact angles when $\epsilon < 0.3$, but deviates when increasing ϵ, with a maximum deviation occurring when $\alpha \approx 90°$. Here, Surface Evolver computations exhibited the slowest convergence, possibly because of the coincidence of the contact line with the singularity in the drop profile at the extremum ($r = 1$); interestingly, the pressure perturbation becomes non-linear in ϵ at $\alpha \approx 90°$ when $\epsilon > 0.2$. Note that k decreases with increasing α, indicating that the the perturbed pressure decreases with increasing contact angle. For very hydrophobic surfaces ($\alpha > 140°$), curvature does not significantly influence the pressure. For hydrophilic surfaces, which are characteristic of the wood fibres, however, the pressure perturbation can be a significant fraction of the unperturbed pressure. Thus, for example, when wood fibres dry, the air bubbles that grow inside the fibre lumen from micrometer dimensioned holes in the cell wall (pit holes), may produce a capillary pressure and an accompanying force that impacts fibre collapse.

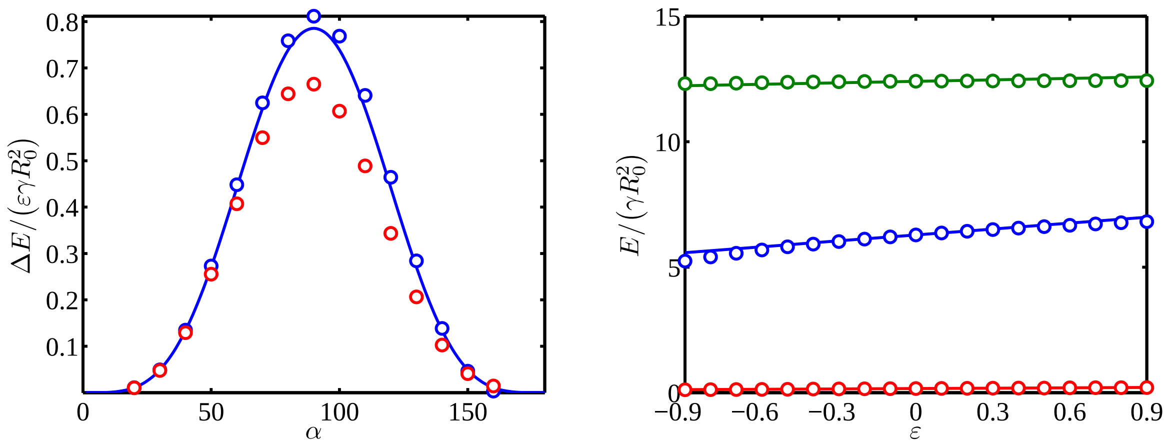

Figure 3.6: (left) Scaled energy perturbation versus contact angle. Symbols are from Surface Evolver with $\epsilon = -0.1$ (blue), and 0.5 (red), and the line is the perturbation approximation. Scaled energy versus aspect ratio (symbols are from Surface Evolver, and lines are the perturbation approximation) with $\alpha = 30°$ (red), $90°$ (blue), and $150°$ (green).

In the theory Section, I showed that the surface energy changes with the substrate curvature when the volume and the contact angle are fixed. This change is expressed as a function of contact angle in Eqn. (3.40), retaining only the first order terms in ϵ. The energy change only depends on the axisymmetric part of the perturbation. Figure 3.6 (left panel) shows how the energy changes with α with constant substrate curvatures $\epsilon = -0.1$ and 0.5. Similarly to the left panel of Figure 3.5, the largest difference between the Surface Evolver and perturbation results occurs when $\alpha = 90°$. The energy change increases with contact angle for hydrophilic surfaces, and decreases for hydrophobic surfaces, with the maximum at $\alpha \approx 90°$. Figure 3.6 (right panel) shows surface energy versus ϵ with three different contact angles. Here, the energy changes that accompany the changing substrate curvature are small compared to the initial energy. The total surface energy increases with curvature when the drop is outside the tube, and decreases when inside the tube.

3.6 Autonomous droplet motion

The foregoing energy change manifests as an energy-gradient force that drives lateral drop migration. To quantify this force, I consider a drop on an harmonic surface

$$z(r, \theta) = A\cos(\kappa x), \tag{3.50}$$

where A, $\kappa = 2\pi/\lambda$, and λ are the amplitude, wave number, and wave length, respectively. Figure 3.7 shows a drop on such surface where a local coordinate system $O'x'z'$ is positioned at the drop centre, and the osculating circle identifies the surface curvature. Approximating the surface locally by a circle, this problem is analogous to the drop on circular tube considered above. Thus, with a parabolic approximation of the circle,

$$z'(r,\theta) = \frac{1}{2}\epsilon x'^2 \tag{3.51}$$

and Eqn. (3.40) furnishes the drop energy. Because the curvature is independent of the coordinate system, I can express ϵ as a function of x, i.e.,

$$\epsilon = -\frac{1}{R} = \frac{A\kappa^2 \cos(\kappa x)}{\left\{1 + [A\kappa \sin(\kappa x)]^2\right\}^{3/2}}, \tag{3.52}$$

which furnishes a lateral force

$$F_x = -\frac{\mathrm{d}E}{\mathrm{d}x} = -\frac{\pi}{4}\sin^4\alpha \frac{\mathrm{d}\epsilon}{\mathrm{d}x}. \tag{3.53}$$

This result is validated by Surface Evolver in Figure 3.8, where a drop is seen to migrate (from right to left) to a position where the substrate has the largest negative (inward) curvature. This curvature-driven drop motion seems to explain the experiments of Renvoisé *et al.* (2009) where a liquid bridge in a tapered tube was observed to self-propel itself to the end with highest surface curvature, thus minimizing its surface energy.

The force is plotted as a function of x in Figure 3.9 (left panel). While the force vanishes at $x = 0$, this is not a position of stable equilibrium. The surface valleys are the energetically favoured (stable) positions for drops and bubbles. Note that, because there is no viscosity and a no-slip boundary condition in the Surface Evolver computation, there is no time scale. Nevertheless, since the force perturbs the equilibrium three-phase contact line, the apparent contact angle is the dynamic contact angle, and the drop moves.

If I neglect energy dissipation in the precursor film of the moving contact line and in the external fluid, then the tangential component of this force F_t is balanced by a viscous resistance $-\zeta\eta R_0 U$, where ζ is a dimensionless friction coefficient and η is the fluid viscosity.

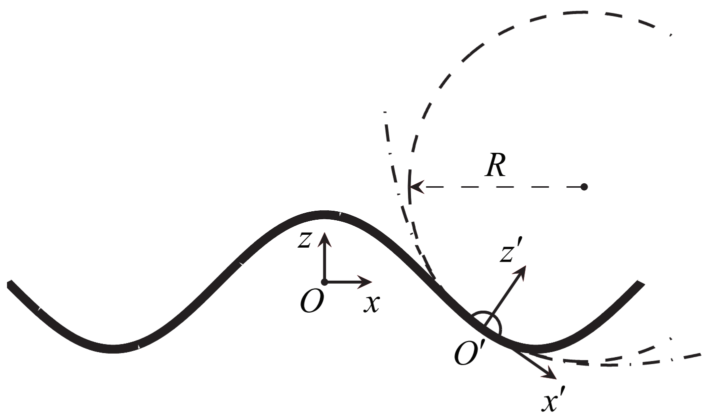

Figure 3.7: A sinusoidal surface showing the osculating circle (dashed line) and its parabolic approximation (dash-dotted line).

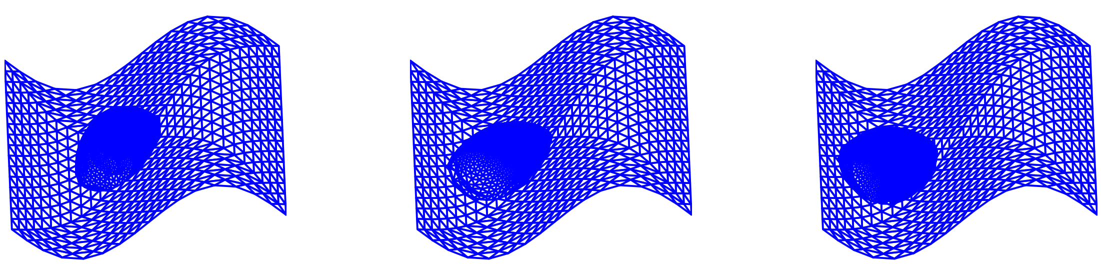

Figure 3.8: Drop motion induced by surface curvature on a sinusoidal surface calculated according to Surface Evolver (time advancing from left to right). The drop migrates from right to left, toward the position with the lowest surface energy.

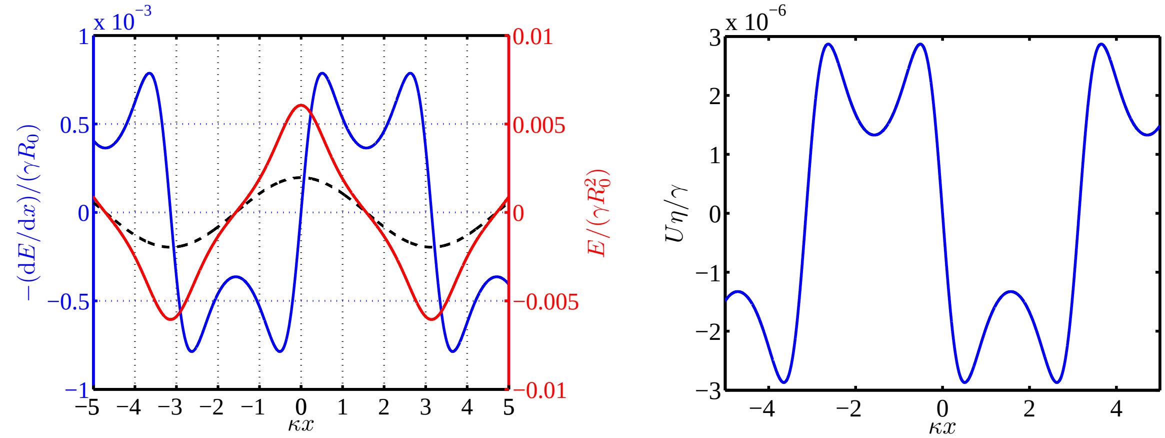

Figure 3.9: Scaled force ($F_x = -\mathrm{d}E/\mathrm{d}x$) and energy ($E$) (left panel), and scaled migration velocity (U) (right panel) versus scaled position for a 1 μL drop on a surface with $A/R_0 = 5$, $\lambda/R_0 = 40$, and $\alpha = 30°$.

The resulting drop velocity is

$$U = \frac{\gamma R_0 F_t}{\zeta \eta R_0} = -\frac{\pi}{4}\sin^4\alpha \frac{\gamma}{\zeta\eta}\frac{\mathrm{d}\epsilon}{\mathrm{d}x}\frac{1}{\left\{1 + [A\kappa\sin(\kappa x)]^2\right\}^{1/2}}. \tag{3.54}$$

Note that three sources of dissipation are present with a moving contact line (de Gennes, 1985): bulk hydrodynamic dissipation, viscous dissipation in the precursor film, and dissipation at the real contact line at the end of the precursor film. Although de Gennes (1985) proved that only the dissipation at the real contact line can be neglected for very small contact angles, it has been popular to neglect the precursor film dissipation (Brochard, 1989; Ford & Nadim, 1994; Daniel et al., 2001; Subramanian et al., 2005). The spherical drop-shape assumption during drop motion implies that the advancing and receding contact angles are equal to the thermodynamic contact angle, deviating from de Gennes (1985) theory. Thus, contact-angle hysteresis is not considered.

Here, I estimate ζ using a lubrication approximation, which restricts the solution to small contact angles where the drop height is small with respect to its radius. Daniel *et al.* (2001) showed that this approximation is valid when $\alpha < 45°$. The shear stress at the substrate-drop interface is

$$\tau = \eta\frac{3U}{h(r,\theta)}, \tag{3.55}$$

where $h(r, \theta)$ is the local drop height. Neglecting the effects of gravity and motion on drop shape, the drop surface is assumed spherical. To avoid the contribution of a non-integrable singularity in τ at the drop periphery, the integration domain must be truncated near the contact line. Following de Gennes (1985), the cut-off distance is furnished by consideration of van der Waals interactions, giving

$$\delta = \sqrt{\frac{A_{\mathrm{H}}}{6\pi\gamma\alpha^4}}, \tag{3.56}$$

where A_{H} is the Hamaker constant, and δ is the cut-off distance. With $A_{\mathrm{H}} \approx 10^{-20}$ J and $\gamma \approx 0.05$ J m^{-2}, I find

$$\delta \approx \frac{10^{-10}}{\alpha^2} \text{ m rad}^{-2}. \tag{3.57}$$

Next, integrating the shear stress over the truncated contact area of a spherical drop gives

$$\zeta = 6\pi \left\{ -\cos\alpha \ln\left[\frac{\delta \tan\alpha}{R_0(1-\cos\alpha)}\right] + (1-\cos\alpha) \right\}, \tag{3.58}$$

which is the same as derived by Subramanian *et al.* (2005) when I replace the sphere radius R_0 in Eqn. (3.54) with contact radius $R_0 \sin\alpha$.

As shown in Figure 3.10 (left panel), plotting ζ at fixed contact radius ($R_0 \sin\alpha =$ constant) demonstrates the effect of contact angle at constant contact area. Note that ζ decreases with drop size and contact angle, and diverges with vanishing contact angle. From ζ, I can estimate the drop velocity. For example, as shown in Figure 3.9 (right panel) for a 1 μL drop with $\eta = 0.001$ Pa s and $\gamma = 0.07$ N m^{-1} on a wrinkled surface with $\alpha = 30°$, $A/R_0 = 5$, and $\lambda/R_0 = 40$, the velocity is ≈ 0.2 mm s^{-1}.

Dimensional analysis shows that the dimensionless drop velocity $U\eta/\gamma$ depends on three independent dimensionless parameters: α, $\kappa R_0 \sin\alpha$, and $A/(R_0 \sin\alpha)$. Note that $U\eta/\gamma$ is the capillary number, which is the ratio of the characteristic viscous shear stresses to the capillary stresses. As shown in Figure 3.10 (right panel), this scaled velocity is small, indicating (as I required for the lubrication analysis) that the drop migrates with negligible deformation. Changes in $\kappa R_0 \sin\alpha$ and $A/(R_0 \sin\alpha)$ represent changes in the substrate-curvature gradient; thus, I set $\Gamma = \kappa^2 A R_0 \sin\alpha$ as a convenient alternate dimensionless parameter. Accordingly, an increase (decrease) in Γ indicates an increase (decrease) in substrate-curvature gradient $\mathrm{d}\epsilon/\mathrm{d}x$ or the drop radius R_0. Therefore, from Figure 3.10, the drop velocity increases monotonically with contact angle, drop size, and substrate-curvature gradient.

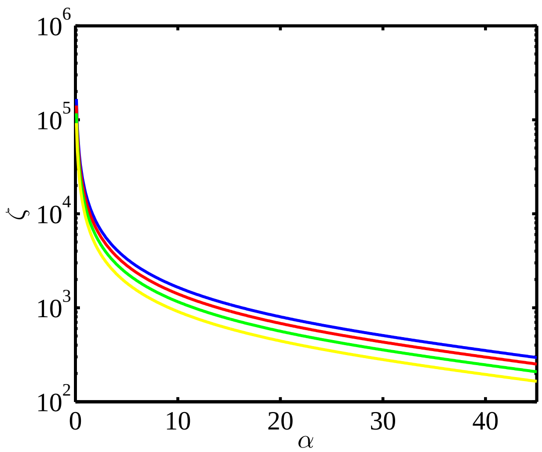

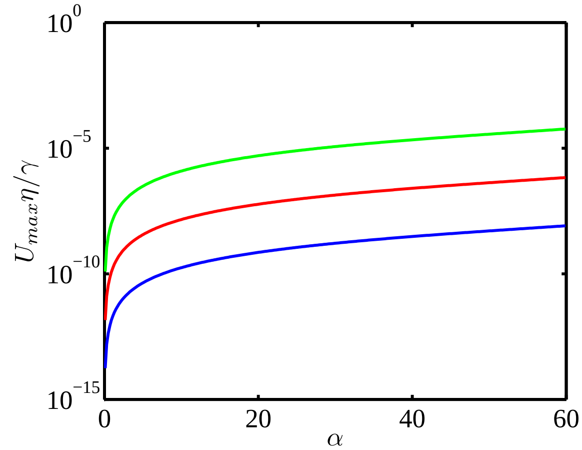

Figure 3.10: (left) Dimensionless friction coefficient (lubrication approximation) versus contact angle with contact radius $R_0 \sin\alpha = 10^{-3}$ (blue), 10^{-4} (red), 10^{-5} (green), and 10^{-4} (yellow). (right) Maximum scaled velocity on a wrinkled surface versus contact angle with $\Gamma = \kappa^2 A R_0 \sin\alpha = 0.001$ (blue), 0.01 (red), and 0.1 (green).

3.7 Summary

A non-axisymmetric perturbation analysis was performed for a drop or a bubble supported on a flat substrate in the absence of gravity. For a spherical cap on a planar substrate, a standard perturbation method was modified by adding a non-axisymmetric perturbation to the substrate, and calculating the perturbation to the drop profile. The solution has a singularity at the extremum ($r = 1$) when the contact angle exceeds 90°, but this can be removed by reconstructing the solution and using the new form in a small neighbourhood near the extremum. Calculating the internal pressure and the surface energy of the perturbed drop, I showed that, at constant volume, the pressure and the energy change with the axisymmetric part of the perturbation. The solution was then used to compute the shape of a drop inside or outside a circular tube, and these analytical results were compared to numerical solutions from the Surface Evolver software. The drop profiles and their perturbations correspond well with the numerical computations for all contact angles, although they depart gradually when increasing the perturbation parameter. I compared the calculated pressure and energy with the numerical results, showing that the internal pressure and surface energy increase with the substrate curvature when the drop is outside the tube, and decrease when inside the tube. Comparing the pressure and the energy at constant substrate curvature, but different contact angles, revealed that the pressure change decreases with the contact angle, while the surface energy change attains a maximum when the contact angle is 90°. Extending the example to a drop on an harmonic surface, I showed that the most energetically favoured (stable) positions for drops are the surface valleys. Indeed, drops are expected to migrate to these positions, driven by a force that is proportional to the surface-curvature gradient. I estimated the drop velocity by balancing the energy-gradient force with the viscous resistance obtained from a lubrication approximation, and found that this velocity increases with surface-curvature gradient, contact angle, and drop radius.

Chapter 4

Elasto-capillary collapse of circular tubes as a model for wood fibres

4.1 Preface

One of the most important capillary-driven deformations of wood fibres is lumen collapse, which is the second objective of this thesis. The following Chapter is focused on the modeling of wood-fibre lumen collapse driven by capillary forces from interfaces that are inside the lumen. Modelling fibres with circular tubes, the equilibrium configurations at each liquid volume are obtained, and their stability is investigated. The effects of the contact angle and elasto-capillary number on the collapsing behaviour of the tubes are discussed, and the results are applied to real wood fibres.

4.2 Abstract

Wood-fibre conformation affects paper properties in various paper-product categories, such as packaging, printing, and absorbents. Qualitative investigations suggest that capillary forces play a crucial role in determining the fibre conformation upon drying. To quantify this process, I theoretically and experimentally investigate deformation of a circular tube under capillary pressure. Fibre pit holes, which impose a significant capillary pressure while drying, are modelled as circular holes in a tube. The calculations are undertaken by coupling the analytical solution for buckling a circular tube to numerical solutions of the Young-Laplace equation. This elasto-capillary model elucidates the influences of wetting

angle, tube-wall flexibility, and hole size on the tube deformation. In experiments, flexible silicon-rubber tubes with a hole in the wall are filled with liquid, and the internal pressure is measured while withdrawing this fluid, thus mimicking evaporation during the drying of wood fibres. The results prove that capillarity can collapse the fibre lumen partially or completely, depending principally on the fibre-wall flexibility.

4.3 Introduction

Cellulose is a renewable polymer that has been manipulated in papermaking for more than 2000 years, affecting many aspects of science, technology, and culture (Hubbe & Bowden, 2009). Paper is a quasi-randomly deposited network of pulp fibres that are bonded following pressing and drying. Wood fibres are typically $1-3$ mm in length and $20-30$ μm in diameter with a complex anisotropic tubular structure in which cellulose micro-fibrils wind around the wall. The lumen is filled with water when in a pulp, but can be removed by subjecting the fibres to an external force. After drying, almost all of the delignified fibres in a paper sheet collapse into ribbon-like structures (Tejado & van de Ven, 2010), which decreases their resistance to bending, and enhances entanglement and the bonded area. Terms such as fibre flexibility (Emerton, 1957), conformability (Mohlin, 1975), compactability (Clark, 1985), and collapsibility (Lowe *et al.*, 2005) are all linked to the ability of fibres to collapse, producing stronger, denser, and less porous networks.

Closing and re-opening of the fibre lumen occurs in various paper manufacturing and recycling processes. While external loading in refining, wet pressing, and calendaring processes can squeeze fibres into collapsed states, capillary forces can also bring fibre walls into close proximity. Although Tejado & van de Ven (2010) have shown that the capillary force in fibre crossings is unlikely to be responsible for the strength of wet paper, and vanishes when water evaporates, they proposed that capillary forces inside the lumen are still considered a possible explanation for lumen collapse during drying. He *et al.* (2003) studied fibre behavior in wet pressing to quantify changes in fibre orientation and transverse dimensions when increasing the pressing pressure. The handsheets were pressed for 2 min at various pressures and dried under restraint before the fibre orientation and cross section were measured using confocal microscopy. They observed that, even at very high pressing pressures, 13% of the fibres were uncollapsed with 33% partially collapsed. The capillary pressure during drying is much lower than the pressing pressure; however, it acts over longer periods of time, and can overcome the effect of inter-fibre surface roughness, bringing the walls into molecular proximity, so that hydrogen bonds and van der Waals forces can maintain the fibres in a permanent ribbon-like conformation (Hubbe, 2007).

Although capillary forces are negligible at macroscopic scales, they dominate when the meniscus length scale is smaller than the capillary length $l_c = (\gamma/\rho g)^{\frac{1}{2}}$, where γ is the surface tension, and ρg is the specific weight. Flexible solids in contact with small interfaces can therefore deform or break if the capillary force exceeds the elastic resistance. These 'elasto-capillary' deformations exist in many practical applications (Roman & Bico, 2010), including micropatterns in a photoresist (Tanaka *et al.*, 1993), lung airway closure (Heil & White, 2002), drop motion on flexible fibre arrays (Duprat *et al.*, 2012), and self-folding of flexible sheets (Péraud & Lauga, 2014).

In this work, I develop a model for the capillary-induced collapse of cylindrical tubes upon drying. The purpose is to understand the physical processes that contribute to the flattening of wood fibres, and to control fibre deformation, since both open- and closed-lumen fibres have technological applications (Hubbe, 2007). However, the results may be important in other applications, such as food drying (Joardder *et al.*, 2013), lung airway closure (Baudoin *et al.*, 2013; Almeida *et al.*, 2013), and microelectromechanical systems (MEMS) (Kwon *et al.*, 2014).

In the wood-fibre literature, fibre flexibility is generally defined as $F = 1/(EI)$ where E is Young's modulus and I is the area moment of inertia in the plane of bending. Determining the fibre elastic modulus is difficult when fibres are wet. Most methods are based on the fibre deformation under tensile stretching (Page *et al.*, 1971; Tchepel *et al.*, 2006) or deflection under bending with one or two supports (Lowe *et al.*, 2005; Yan & Li, 2008). The fibre elastic modulus depends on several factors, such as microfibril angle, pulping process, and moisture content.

The fibre wall comprises a thin primary wall and a secondary wall that is divided into the outer, middle, and inner layers, termed S1, S2, and S3, respectively. The thickest layer (S2) contains 90% of the fibre mass, and has cellulose micro-fibrils wound into a spiral with a helix angle in the range 0–15°. This is the most influential layer for determining fibre-wall mechanical properties. Gindl & Schöberl (2004) modeled S2 as a fibre reinforced composite with cellulosic microfibrils as the fibres and the mixture of hemicelluloses and lignin as the continuous phase. Using available data for the elastic and shear moduli of cellulose, hemicelluloses, and lignin, the longitudinal and transverse elastic moduli were calculated as a function of the microfibril angle. For small microfibril angles, the transverse elastic modulus was found to be one order of magnitude smaller that the longitudinal elastic modulus.

The pulping process and mechanical and chemical treatments during papermaking significantly change fibre mechanical properties. For example, chemical pulp fibres are more flexible and more readily collapsible than mechanical pulp fibres (Hubbe *et al.*, 2007), and recycling decreases flexibility in chemical pulps while increasing flexibility in mechanical pulps (Dulemba *et al.*, 1999). For chemical pulps, the elastic modulus increases when increasing yield – the mass percentage of the recovered pulp compared to the original wood – for virgin fibres, while it slightly decreases at very low yields for recycled fibres (Scallan & Tigerström, 1991). Yan & Li (2008) proposed a new method to measure wet-fibre flexibility using confocal laser scanning microscopy, and showed that refining and bleaching significantly reduce the elastic modulus of wet fibres.

When the fibre wall is completely saturated, water prevents intermolecular bonds forming between cellulose micro-fibrils, leading to a soft fibre wall (Yan & Li, 2013). There are three main types of water in wood cells: free water, which exists inside the fibre lumen and between fibres; freezing bound water; and non-freezing bound water, which interacts directly with cellulose. During drying, free water and freezing bound water first evaporate in tandem (Weise *et al.*, 1996), and then non-freezing bound water evaporates until a very high solid content is reached. The fibre saturation point occurs when all free water is removed, leaving only bound water. As water is removed from the cell walls, hydrogen bonds form between cellulose fibrils, resulting in a stiffer and less porous cell wall (Yan & Li, 2013). However, capillary-induced collapse occurs before the fibre saturation point. At this time, an interface may form inside the lumen while the cell wall is still saturated.

Fibre flexibility is significantly affected by fibre dimension, especially fibre wall thickness and diameter (Yan & Li, 2008). Various papermaking and recycling processes may change fibre wall thickness, but they cause negligible changes in the fibre perimeter (Jang *et al.*, 1996). Therefore, the fibre diameter can be considered constant if a circular initial cross section is assumed. Jang *et al.* (1996) observed that increasing the specific energy in pulping and refining intensity decreases the fibre wall thickness via a 'peeling off' mechanism that involves delamination and detachment of fibre-wall material.

Considering the diversity of wood species, pulping processes, and mechanical and chemical treatments used in technological fibre applications, I propose a range for the fibre dimensions and elastic moduli for wet fibres during drying. An extensive review of the literature suggests that longitudinal elastic moduli are in the range $0.2 - 20$ GPa, and that fibres have $0.8 - 5$ μm wall thickness and lumen radii $3 - 18$ μm, with thickness-to-radius ratios in the range $0.05 - 1$ (Fischer *et al.*, 2014; Adusumalli *et al.*, 2010; Dulemba *et al.*, 1999; Gindl & Schöberl, 2004; Nilsson *et al.*, 2000; Page *et al.*, 1977; Saketi *et al.*, 2010; Scallan & Tigerström, 1991, 1992; Tchepel *et al.*, 2006; Yan & Li, 2008, 2013; Jang *et al.*, 1995, 1996; Jang & Seth, 1998).

4.4 Theory

4.4.1 Elastic analysis

To model the cell wall elastic deformation, I consider an initially circular tube with radius R, and constant wall thickness t. When the tube is subjected to a uniform radial traction due a pressure

$$P = P_o - P_i, \tag{4.1}$$

where P_o and P_i are the external and internal pressures, it deforms elastically while maintaining a circular cross section. However, above a critical positive value of P, the tube buckles into an ellipse, eventually adopting a fully collapsed cross section. To analyse the deformation during buckling, I consider a section of unit length. From symmetry, it is sufficient to analyse the deformation of a quarter section. I assume that the strain is small enough to justify a linear stress-strain relationship. Following Moreno *et al.* (1970), I consider the tube wall to be a curved beam, and use the theory of Love (1893) to calculate the buckled-tube profile according to

$$\frac{y''}{\left(1 + y'^2\right)^{3/2}} = -\frac{P}{2EI}\left[\left(x^2 + y^2\right) - r_0^2\right] - \frac{1}{R_0}, \tag{4.2}$$

where the origin is at the tube center, E is Young's modulus, and EI is the flexural rigidity with area moment of inertia[1]

$$I = \frac{t^3}{12}. \tag{4.3}$$

As shown in Figure 4.1(a), r_0 is the distance from the center, and R_0 is the tube wall radius of curvature at $y = 0$. Equation (4.2) requires four boundary conditions to ascertain r_0 and R_0:

$$y(r_0) = 0, \quad y'(r_0) = \infty, \quad y'(0) = 0 \tag{4.4}$$

[1] This is the area moment of inertia per unit length of the tube, having the unit m^3 instead of m^4.

with constant circumference S. I numerically integrate eqn (4.2) and use a shooting iteration to calculate r_0 and R_0 when

$$P > P_b = \frac{3EI}{R^3}, \tag{4.5}$$

which holds for circular beams. Tube profiles and values of r_0 and R_0 are shown in Figure 4.1. Here, the corresponding strain energy is (Timoshenko, 1930)

$$\delta U_e = \frac{M^2}{2EI} R\mathrm{d}\theta = \frac{EI}{2}\left\{\frac{P}{2EI}\left[\left(x^2+y^2\right)-r_0^2\right]+\left(\frac{1}{R_0}-\frac{1}{R}\right)\right\}^2 R\mathrm{d}\theta, \tag{4.6}$$

where M is the bending moment and $R\mathrm{d}\theta$ is a differential segment of the tube wall.

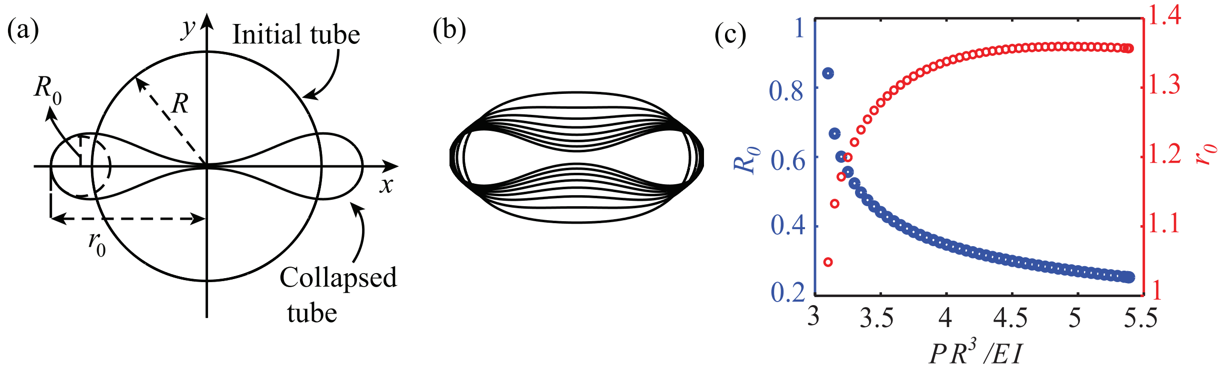

Figure 4.1: (a) Fibre cross section and its geometrical parameters before and after buckling. (b) Buckled-tube profiles when increasing the external pressure. (c) The tube-wall distance from its center at $y = 0$ (r_0), and the tube-wall radius of curvature at $y = 0$ (R_0) versus the scaled pressure.

4.4.2 Capillary analysis

Small $1 - 7$ μm openings in fibre walls —termed "pits"— assist intercellular transport. The primary walls in these holes produce a separating porous membrane that is destroyed during pulping (Ilvessalo-Pfäffli, 1995). When a single fibre is dried, air penetrates through pit holes if the fibre lumen has closed ends. This produces small interfaces that are pinned to the pit holes, providing capillary pressures that are greater than those produced by interfaces covering the lumen periphery. Therefore, to investigate the most significant capillary role in fibre collapse during drying, I suppose that fibres have closed ends, and that the only openings for gas penetration are the pits. Here, since the capillary-pressure and surface-tension forces are scaled with $\gamma R^2/R_h$ and γR_h, respectively, where R_h is the hole radius, I may neglect surface-tension forces when $(R_h/R)^2 \ll 1$.

I have previously calculated the bubble shape and pressure on curved surfaces (Soleimani *et al.*, 2013), showing that the maximum capillary pressure occurs when the bubble radius of curvature equals R_h, and can be approximated by

$$P_{max} \approx \frac{2\gamma}{R_h}. \tag{4.7}$$

If this capillary pressure exceeds the critical pressure from eqn (4.5), then the tube buckles, and if $P_{max} > 5.398EI/R^3$ (see Figure 4.1), then the tube walls touch. As shown in Figure 4.2(a), the bubble may exist between the merged walls or in an arbitrary location on the lobe-shaped section of the buckled tube. If the capillary pressure reaches P_{max} and the bubble does not contact the opposite wall — either because $P_{max} < 5.398EI/R^3$ or because it resides in the lobe — the tube opens and returns to its initial circular conformation. In this analysis, the projected area of the hole is preserved during deformation. According to the elastic analysis, this assumption introduces negligible relative error to the hole size, i.e., less than 0.0005%, 0.1%, 0.6%, and 4% when $R_h/R = 0.01$, 0.1, 0.2, and 0.5, respectively.

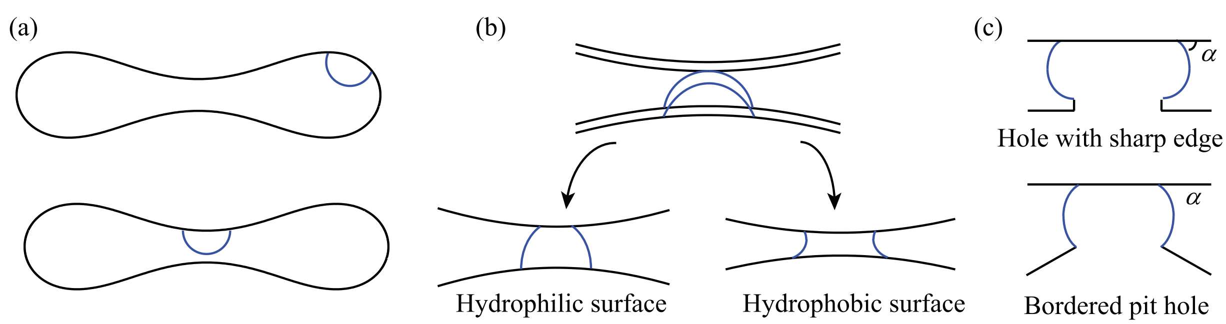

Figure 4.2: (a) Bubble position on a buckled tube. When the bubble is between the closed walls, it can bridge the gap easier than when at other positions. (b) Topological change when a bubble contacts the opposite wall. (c) Configurations where the contact angle at the hole may exceed the wetting angle.

When a bubble reaches the opposite tube wall [Figure 4.2(b)], it bridges the gap between the buckled walls. Here, the evolution of a stable bridge depends on the tube-wall wetting angle α, i.e., the equilibrium contact angle, in addition to tube flexibility and perforation size. The interface shape before and after bridging is governed by the Young-Laplace equation, which I solve using the Surface Evolver software (Brakke, 1992) to numerically calculate equilibrium fluid interfaces. With a polygon prism as the initial condition, iterations begin using the gradient descent method. I progressively refine the mesh, remove small edges, and equiangulate to achieve uniform triangular facets. The contact line is allowed to leave the hole edge when the contact angle reaches the wetting angle. After 100 iterations and mesh refinement to about 2000 facets, I switch the minimization algorithm to the conjugate gradient method, to speed convergence. First-order convergence of the energy with respect to the number of facets is achieved to eight significant digits in the total energy with $\approx 25,000$ facets. With 1000 iterations, the energy changed less than 0.004%, eliminating the possibility of the local minimum being a saddle point (Brakke, 2008).

Theoretically, the interface becomes unstable and detaches from the perforation edge when the contact angle at the edge exceeds α (Slobozhanin & Tyuptsov, 1974, 1975). However, the interface inside the buckled tube has various apparent contact angles around the non-axisymmetrically deflected edge of the perforation. Consequently, while the contact angle reaches α at some points, it is still smaller than α at other positions, so the interface leaves the edge non-axisymmetically. Figure 4.3 shows how the interface detaches from the hole when varying the wetting angle. For large wetting angles, the interface extends in the longitudinal direction of the buckled tube, whereas for small wetting angles it expands in the traverse direction, and for a specific wetting angle, it detaches symmetrically from the edge of the hole. This critical wetting angle depends on the perforation size and the shape of the deflected tube. For example, at $R_h/R = 0.2$ and $(P_eR^3)/EI = 5.37$, symmetric detachment occurs when $\alpha \approx 87.4°$.

The perforations in my experiments have sharp corners (from drilling), which affects the contact angle at the hole [shown in Figure 4.2(c)]. Therefore, in addition to the wetting angle limit, the interface is pinned to the hole until its surface becomes tangent to the tube wall. This can occur in wood fibres, since the interface is pinned to the asperities of the fibrillated surface around the pit holes (Tejado & van de Ven, 2010) or the sharp edge of bordered pit holes [Figure 4.2(c)], achieving contact angles that exceed the wetting angle. Results of analyses with these two criteria are compared in Section 4.6.

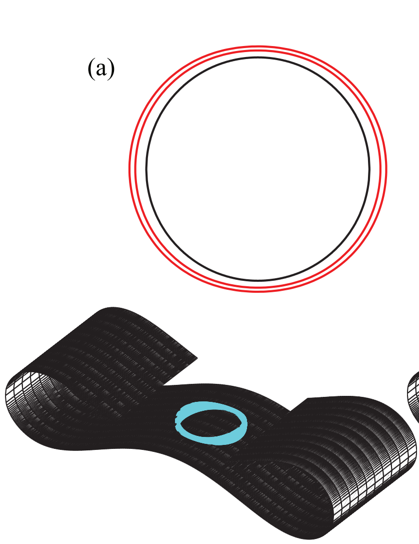

Figure 4.3: The top projections (top) and the 3-dimensional visualizations (bottom) of the bridged interfaces detaching from the hole edge after the contact angle exceeds the wetting angle. From left to right: symmetrical detachment at $\alpha = 87.4°$, longitudinal detachment at $\alpha = 100°$, and transverse detachment at $\alpha = 80°$, all with $R_h/R = 0.2$, $P_eR^3/EI = 5.37$. In the top views, the black lines are the hole edges, and the red lines are the detached contact lines. In the 3-dimensional views, a tube top section is removed to view the fluid interfaces.

4.4.3 Elasto-capillary analysis

Interactions of the interface and elastic tube are assessed by combining the calculated elastic deformation and capillary-interface solutions. At a specific liquid volume V_L, the equilibrium state is achieved when the interface provides the required capillary pressure to reduce the tube lumen-volume V_T to $V_T = V_L + V_G$, where V_G is the gas volume. If this equilibrium corresponds to a minimum in the total energy, which is the sum of the elastic and interfacial energies, then the solution is considered stable.

The elasto-capillary analysis is undertaken by coupling the elastic solution calculated within Matlab to the capillary solution from Surface Evolver. The tube cross-section shape is calculated by solving eqn (4.2) in Matlab, and Surface Evolver is called by Matlab to compute the interface shape, energy, and capillary pressure. To transfer the tube profile from Matlab to Surface Evolver, I fit a curve of the form

$$y = \sum_{i=1}^{n} a_i \left[\left(\frac{r_0}{R} \right)^2 - x^2 \right]^{\frac{i}{2}}, \tag{4.8}$$

to the calculated profile with $n = 4$ and more than 18000 data points, achieving a root mean square (RMS) error less than 10^{-4}.

4.5 Experiment

Super soft latex tubes (McMaster Carr) with $3/4''$ outside diameter and $1/16''$ wall thickness were selected to verify the tube-buckling theory. Tubes were filled with silicon oil (Sigma Aldrich) with 5 cSt viscosity and 913 kg m^{-3} density (reported at 25°C), and immersed in a water-methanol bath at room temperature to remove the influence of gravity. To maintain equilibrium, the inside liquid was pumped slowly (1 mL min^{-1}) at each step, and left for five minutes to relax.

To verify the elasto-capillary analysis, silicon elastomer tubes [Van Waters and Rogers (VWR) Company] were selected with $0.076''$ outside diameter and $0.009''$ thickness, and typical length to radius ratio in the range $20-30$ to ensure that the tube diameter was small compared to its length. Very small holes were drilled at the tube mid-point using 0.15 mm, 0.1 mm, and 0.05 mm drill bits following immersion of the tube in liquid nitrogen to cool below the glass transition temperature. The final perforation diameters were measured with a microscope, furnishing 0.044 ± 0.005 mm, 0.022 ± 0.003 mm, and 0.010 ± 0.002 mm for the 0.15 mm, 0.1 mm, and 0.05 mm drill bits, respectively. The wall thickness and tube diameters were measured before and after freezing, furnishing 0.19 ± 0.01 mm and 1.94 ± 0.03 mm, respectively. The elastic moduli of the tubes were measured using a standard tension test, furnishing $E = 3.1 \pm 0.2$ MPa under small longitudinal strain. The static wetting angles for water and oil on the tube wall were $104 \pm 4°$, $22 \pm 2°$, respectively. A tensiometer was used to measure the wetting angle by depositing $2 - 4$ μL drops on the tube surface, after cutting, opening and flattening. The oil surface tension in contact with air was 27.49 ± 0.05 mN m^{-1}, measured at 25°C using a Wilhelmy plate. The oil density was reported by the suppliers to be 880 kg m^{-3}. The foregoing uncertainties are standard deviations from three to ten measurements.

The silicon tubes were filled with water or oil, and then the inside liquid was slowly pumped from one end while recording the internal pressure with a pressure transducer. To isolate the contribution of viscous pressure losses, several pumping rates were used in the range $0.003 - 0.01$ μL min^{-1}. If the perforation was small enough, the pressure decreased until the tube flattened completely. Otherwise, at a specific negative pressure, the bubble at the hole entered the tube, resulting in a discontinuous change in the internal pressure. For example, for the silicon tube with 0.022 mm perforation diameter, the pressure jump occurred at -12.5 ± 1 kPa and -6.7 ± 0.1 kPa (independent of the rate)[2] when using water and oil, respectively; with a 0.01 mm hole, no jump was observed until a completely collapsed state was achieved.

4.6 Results and discussion

4.6.1 Theoretical predictions

To identify the equilibrium state of the buckled tube, various tube-interface configurations at constant volume were computed by projecting an external pressure to the tube, independent of the interfacial capillary pressure. As shown in Figure 4.4 (left panel), the external pressure is scaled with the flexural rigidity (EI), while the capillary pressure is scaled with surface tension. Because the external and capillary pressures are equal at equilibrium, the equlilibria are identified when

$$\frac{P_c R}{\gamma} = \Omega \frac{P_e R^3}{EI}, \tag{4.9}$$

[2]The viscous pressure is less than 2 mPa at these rates.

where the elasto-capillary number

$$\Omega = \frac{EI}{\gamma R^2} \tag{4.10}$$

is the ratio of the elastic energy to the interfacial energy.

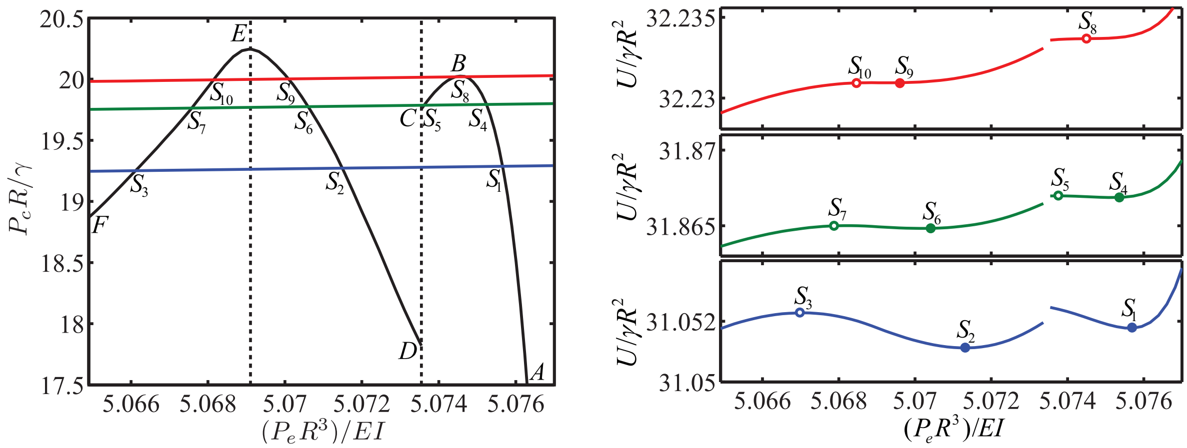

Figure 4.4: Computational results for $\alpha = 40°$ and $R_h/R = 0.1$. (Left) Capillary pressure calculated from interface solution versus external pressure that controls elastic deformation at constant liquid volume. Lines identify $\Omega = 3.800$ (blue), 3.900 (green), and 3.945 (red). The intersections of the lines and curves are equilibrium points. (Right) Energy of constant-volume configurations for the same elasto-capillary numbers as the left panel, showing stable (filled symbols) and unstable (open symbols) equilibria.

In Figure 4.4 (left panel), points on the curves AC and DF correspond to situations where the interface forms a bubble and a bridge, respectively, at constant liquid-volume. At point C, the bubble contacts the opposite buckled-wall, and the interface bridges the gap between the walls, identified by point D [see Figure 4.2(b)]. When the contact angle equals the wetting angle, the interface leaves the hole to reduce the interfacial energy, furnishing a maximum in the capillary pressure at point E. On the curve EF, the interface has either partially or completely left the hole. Lines of constant elasto-capillary number are also shown with $\Omega = 3.800$, 3.900, and 3.945. Based on eqn (4.9), equilibrium states are the intersections of constant Ω lines and constant-volume curves. Therefore, with $\Omega = 3.800$, there are three equilibrium states S_1, S_2, and S_3; with $\Omega = 3.900$, four equilibrium states exist, S_4, S_5, S_6, and S_7. Here, S_1, S_4, and S_5 are bubbles, whereas S_2, S_3, S_6 and S_7 are bridges.

Figure 4.4 (right panel) shows the total energy (the sum of interfacial and elastic energies) for various tube-interface configurations at constant liquid-volume and the same values of Ω. With $\Omega = 3.800$, S_1 and S_2 are the energy minima, and, therefore, are stable equilibrium states, so the system reaches one of these states according to the initial condition. When drying a wood fibre, because the liquid volume decreases, the initial interface is a bubble, so the system transits to S_1. With $\Omega = 3.900$, S_4 and S_6 are energy minima, but S_5 and S_7 are energy maxima, so S_3, S_5 and S_7 are unstable equilibrium states. For the same reason, all of the points on curves BC and EF in Figure 4.4 (left panel) are unstable. At these unstable equilibrium points, for example, a small constant-volume perturbation to a more-collapsed state (larger external pressure) increases the capillary pressure, which increases deformation. In contrast to S_3, a small perturbation to a more collapsed state at S_2 produces a smaller capillary pressure, retrieving the stable equilibrium state. With $\Omega = 3.945$, a saddle point in energy is produced when the constant-Ω line becomes tangent to the constant volume curve (S_8). At these points, a bubble becomes unstable before contacting the opposite wall, jumping from S_8 to S_9, which is an energy minimum.

When the liquid volume decreases, the curves in Figure 4.4 (left panel) shift to higher pressures. As shown in Figure 4.5, by decreasing the liquid volume, the capillary pressure of the bubble at the point of contact between the bubble and the tube wall [point C in Figure 4.4 (left panel)] decreases, while the maximum capillary pressure at point E increases. Bubble configurations [curve AC in Figure 4.4 (left panel)] are independent of wetting angle, since the interface is separated from the opposite wall and the contact angle at the hole is smaller than the wetting angle. However, bridge configurations [curve DF in Figure 4.4 (left panel)] are highly regulated by the wetting angle. Whereas for $\alpha = 40°$ [Figure 4.5 (left panel)] point D has a positive capillary pressure, for $\alpha = 90°$ [Figure 4.5 (right panel)] it moves to negative capillary pressures. Furthermore, the increase in the capillary pressure of point E slows when increasing the wetting angle. Note that at $\alpha = 90°$ [Figure 4.5 (right panel)], the beginning of the interface detachment from the hole is different from the maximum capillary pressure, so the system remains stable after the interface leaves the hole.

Stable equilibrium states are calculated using the method explained in Figure 4.4, and are plotted in Figure 4.6 (left panel) at various liquid volumes for $\alpha = 70°$ and $R_h/R = 0.1$. For small Ω, two stable equilibrium states exist in this range of liquid volumes, similarly to $\Omega = 3.800$ in Figure 4.4. As Ω increases, the end point of the bubble solution shifts to higher volumes, and the beginning of the bridge solution moves to lower volumes. At a critical elasto-capillary number Ω_c, these two points coincide, and for $\Omega > \Omega_c$, when the bubble contacts the opposite wall, no stable bridge solution exists to maintain a collapsed

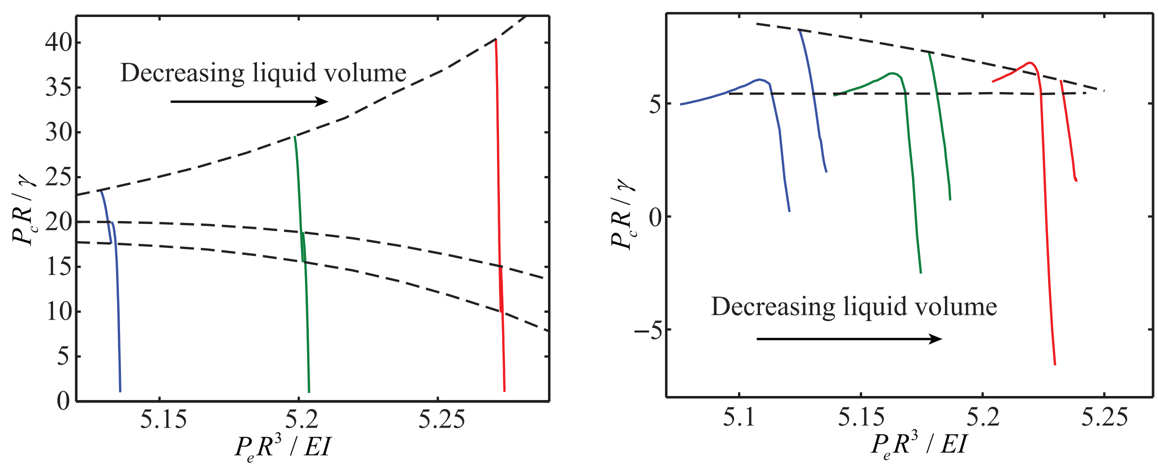

Figure 4.5: Computations of capillary pressure versus external pressure. (Left) $\alpha = 40°$, $R_h/R = 0.1$, $V/R^3 = 1.03$ (blue), 0.99 (green), and 0.95 (red). (Right) $\alpha = 90°$, $R_h/R = 0.2$, $V/R^3 = 0.99$ (blue), 0.96 (green), and 0.93 (red). Dashed lines show the critical points at which the bubble contacts the opposite wall to form a liquid bridge [points C and D in Figure 4.4 (left panel)] and when the bridge leaves the hole.

tube. Therefore, the tube opens if $\Omega > \Omega_c$. After the bridge forms when $\Omega < \Omega_c$, a decreasing liquid volume furnishes a higher capillary pressure, which increases the deformation. Calculations are continued until the gap between the walls is 0.07% of the tube radius and the interface remains stable. This means that, if the interface can form a stable bridge when it reaches the opposite wall, the tube will collapse completely by decreasing the volume of the remaining liquid until the tube walls make contact.

The critical elasto-capillary numbers computed for various wetting angles and hole radii are plotted in Figure 4.6 (right panel). A circular tube with a prescribed hole diameter and wetting angle collapses completely if the elasto-capillary number is below these curves. The normalized critical elasto-capillary number $\Omega_c R_h/R$ decreases with increasing wetting angle, so tubes collapse completely when α is small. When decreasing R_h/R, even though $\Omega_c R_h/R$ decreases, Ω_c increases, indicating easier collapse. The maximum critical elasto-capillary numbers correspond to the interface becoming unstable by switching from an energy minimum to a maximum. This occurs because the bubble reaches its maximum capillary pressure and becomes unstable at a greater liquid volume, before it contacts the opposite wall, similarly to $\Omega = 3.945$ in Figure 4.4. Therefore, Ω_c corresponds to a configuration with maximum bubble pressure, is independent of wetting angle, and is equal to the maximum Ω_c for smaller wetting angles than the critical α, as shown by the solid

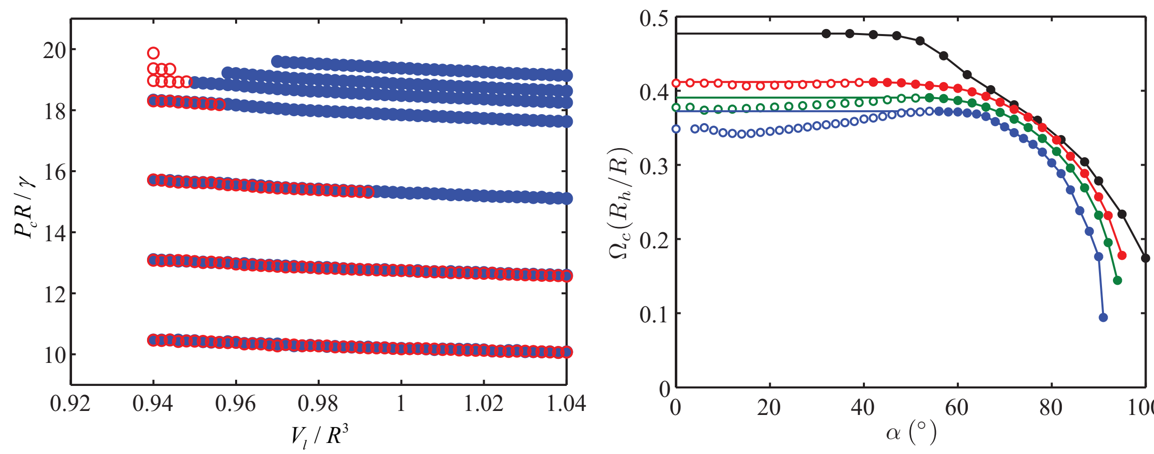

Figure 4.6: (Left) Computations of capillary pressure versus liquid volume when increasing Ω beyond Ω_c. No equilibrium solution exists when the bubble becomes unstable if $\Omega > \Omega_c$. Red symbols are bridge solutions, and blue symbols are bubble solutions. (Right) Critical elasto-capillary number (solid lines) versus wetting angle for $R_h/R = 0.01$ (blue), 0.1 (green), 0.2 (red), and 0.5 (black). Open symbols displaced from solid lines identify unstable configurations.

lines in Figure 4.6 (right panel). The unstable branches are shown as symbols without lines. The critical wetting angles where the instability occurs are weakly affected by the hole size.

Considering situations where the contact angle at the sharp edge may exceed the wetting angle, I performed calculations with the interface pinned to the hole edge until it becomes tangent to the tube wall. As shown in Figure 4.7 (left panel), while the bubble interfaces are unaffected by this change, the bridge interfaces destabilize at higher capillary pressures before becoming tangent to the tube wall. The critical elasto-capillary numbers of the two situations are compared in Figure 4.7 (right panel). This demonstrates that it is possible to form a stable bridge and completely collapse the tube, even with a large wetting angle.

4.6.2 Experimental results

The results of tube-buckling tests with several tube samples are compared with theory in Figure 4.8 (left panel). Here, V_0 is the initial unstrained tube volume, and P_0 is the hydrostatic pressure of the water-methanol bath at the level of the tube center. In contrast to theory, a smooth transition between circular and buckled configurations is observed. By increasing the external pressure beyond the critical pressure, the internal volume decreases

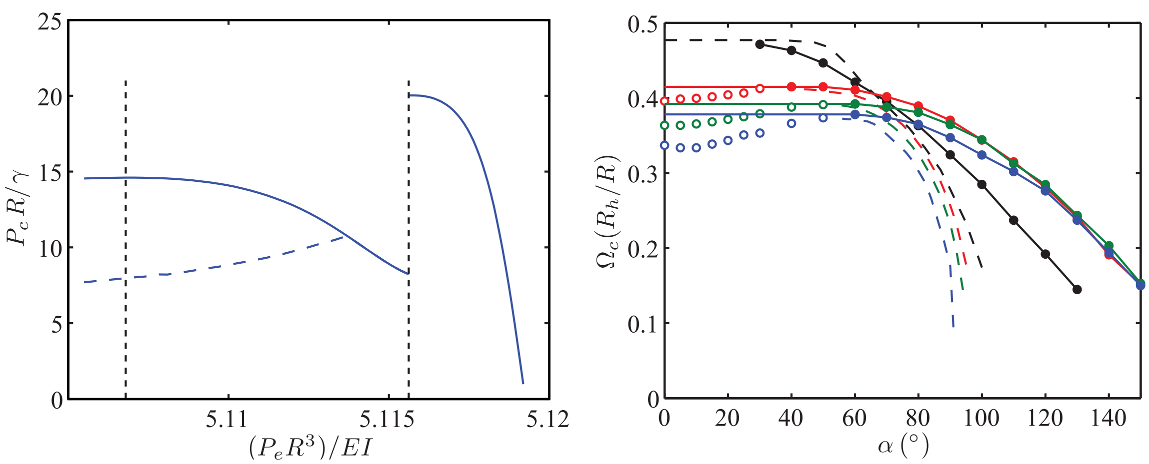

Figure 4.7: Computations of (left) capillary pressure versus external pressure for various configurations with constant liquid volume when the contact angle can be larger than the wetting angle at the hole edge. The dashed line is for the interface when it leaves the hole at the wetting angle. (Right) Critical elasto-capillary number versus wetting angle for $R_h/R = 0.01$ (blue), 0.1 (green), 0.2 (red), and 0.5 (black) when the contact angle can be larger than the wetting angle at the hole edge (solid lines), and when the interface leaves the hole at the wetting angle (dash lines). Open symbols displaced from solid lines identify unstable configurations.

rapidly until the opposite walls make contact, slowing the decrease in volume.

As explained in Section 4.5, when an interface pinned to the holes of the silicon elastomer tubes becomes unstable, the internal pressure jumps to a higher value, as seen in Figure 4.8 (right panel). By decreasing the hole diameter, the pressure jump occurs at a lower pressure. The tests were terminated at −23 kPa, as air bubbles appeared in the tube, either from the joints or by evaporation. The silicon tubes did not follow the same path when repeating the tests, because of hysteresis in the tube buckling; but the pressure jump where the bubble becomes unstable was highly reproducible using several tubes and various pumping rates.

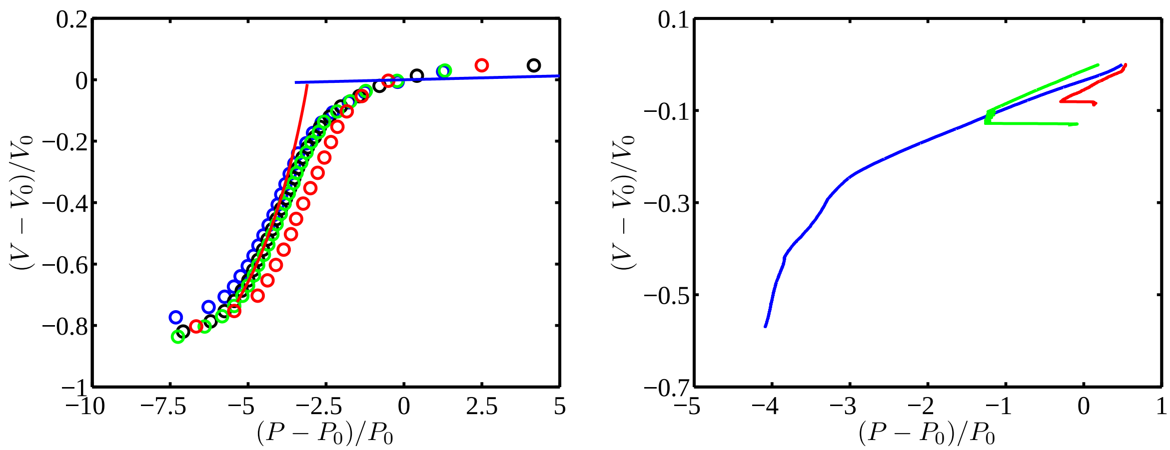

Figure 4.8: (Left) Experiments (symbols) compared with theory (lines) for several tubes. The blue line corresponds to circular cross-sectional configurations, and the red line is when a tube becomes non-circular. (Right) The discontinuity in pressure when a bubble at the hole becomes unstable. The blue line is for complete collapse with no hole on the tube, the green line is for $R_h = 0.022$ mm, and the red line is for $R_h = 0.044$ mm. The fluid withdrawal rate is 0.005 μL min^{-1}.

Results with silicone tubes, various perforation diameters, and internal liquids are shown in Figure 4.9. With a 0.01 mm hole, very small air bubbles entered the tube from the hole when using water, but complete collapse was observed when using oil without air entering the tube. Therefore, the only experimental observation of complete tube collapse occurred with the 0.01 mm hole and oil as the internal liquid, as identified in Figure 4.9. Here, the error bars are from propagating the standard deviations of the measurements of E, t, R, R_h, and γ. Consequently, considering the uncertainty in the normalized values of Ω_c, experiments seem to confirm theoretical predictions of the critical elasto-capillary number.

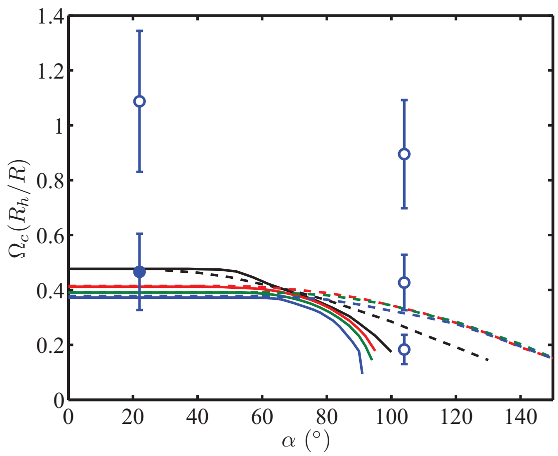

Figure 4.9: Phase diagram of the critical elasto-capillary number Ω_c versus wetting angle α comparing experiments (symbols) with theory (lines). The solid lines show $\Omega_c R_h/R$ when the contact angle at the hole cannot exceed the wetting angle, whereas the dashed lines are for when the contact angle can be larger than the wetting angle: $R_h/R = 0.01$ (blue), 0.1 (green), 0.2 (red), and 0.5 (black). The only experiment in which complete collapse was observed is identified with a filled symbol, confirming the critical elasto-capillary numbers from theory when the contact angle at the hole cannot exceed the wetting angle. For other experiments (open symbols), the tube either did not buckle or partially buckled, similar to Figure 4.8 (right panel).

4.6.3 Effect of capillarity in lumen collapse of wood fibres

In this analysis, we approximate fibres as having an initially circular cross-section. It should be noted that the cross section of real wood fibres varies along the fibre axis, being almost circular in earlywood or springwood, and rectangular in latewood or summerwood. Thus, my approximation amounts to a worst-case scenario, because any deviation from a circular cross-section would promote collapse. We also approximate fibres to be uniform along their longitudinal axis, which is justified, in part, by the longitudinal elastic modulus of real fibres being an order of magnitude larger than the transverse value.

As stated in section 4.4.2, the largest capillary pressure acting on open-lumen fibres is from the interface that is pinned to the pit holes. However, when fibre walls are very close or in contact, the pressure from liquid bridges can be sufficient to induce mutual conformation Persson *et al.* (2013). Therefore, my calculations were terminated when the capillary pressure at the pit hole brought the fibre walls into contact. It is possible for liquid bridges that occlude the fibre lumen to initiate collapse Heil (1999*b*), but the foregoing capillary-bridge mechanism is stronger, and perhaps more realistic, particularly when fibres have closed ends. Here, we consider situations when the contact line leaves the pit-hole border, either once the contact angle reaches the wetting angle or once the interface becomes tangent to the fibre wall. Nevertheless, fibre-wall roughness, porosity, and geometrical irregularities may lead to more complex behaviour of the contact line in real fibres.

Recall from Section 4.3, wood fibres have $3-18$ μm lumen radii and $0.8-5$ μm wall thickness, giving a thickness to radius ratio in the range $0.05-1$. In my model, since the tube cross section is approximated by a curved beam, the transverse elastic modulus is the appropriate modulus; this is one order of magnitude smaller than the longitudinal elastic modulus, in the range $0.02-2$ GPa. With these properties, $\Omega R_h/R$ is in the range $10^{-3}-10^{4}$. The wetting angle is in the range $30^\circ-100^\circ$, depending on the fibre and its chemical or mechanical treatment. Consequently, the capillary pressure may drive complete collapse in sufficiently flexible wood fibres. For example, bleached spruce Kraft pulp has a transverse elastic modulus ≈ 0.15 GPa (Yan & Li, 2008), so with $t/R \approx 0.15$, I have $0.2 < \Omega R_h/R < 1.4$ for various pit-hole sizes. This means that if a uniform distribution of fibre dimensions and an elastic modulus are presumed, then the non-uniform distribution of pit-hole diameters results in complete collapse of some fibres, while others remain open, as often observed. However, in rigid wood fibres, such as mechanical fibres or latewood fibres, capillary pressure is not predicted to affect the final configuration.

4.7 Conclusions

Buckling of a circular tube driven by the capillary pressure at an interface pinned to a small hole in a tube wall was analysed, and necessary conditions for a stable bridge, leading to complete tube collapse upon drying, were deduced. After comparing the theoretical results with experiments, I applied the phase diagram in Figure 4.9 to wood fibres. This showed that capillary forces may flatten wood fibres completely or partially during drying, according to their physical, chemical, and geometrical properties. Future analyses may include the orthotropic behaviour of the fibre elastic modulus, with a rectangular cross section, and include the effects of surface-tension force on fibre deformation.

Chapter 5

Capillary force between flexible filaments

5.1 Preface

Capillary forces are very important in bonding crossing wood fibres to each other in a paper sheet. They can deform the fibres to attach, and then, conform their surfaces to each other for a strong bonding. Analysis of the capillary forces between flexible fibres is the third objective of this thesis, which is the subject of the following Chapter. Two crossing or parallel flexible filaments are attracted to or repelled from each other when subjected to the capillary forces from a liquid bridge at their crossing. The equilibrium conformation is calculated iteratively, and the effects of elasto-capillary number, contact angle, crossing angle, separation, and liquid volume are investigated.

5.2 Abstract

Liquid droplets bridging two filaments are ubiquitous in nature and technology. Although the interface shape and the capillary force and torque have been studied extensively, the effect of filament flexibility is poorly understood. Here, I show that elastic deformation can significantly affect the interface shape and capillary force. I calculate the equilibrium state of parallel filaments, using analytical approximations and numerical solutions for the fluid interface. The results compare favourably, and the numerical solution is then applied for crossing filaments. In the investigated range of parameters, the capillary force increases

rapidly when the filaments touch. The force decreases continuously when decreasing the liquid volume with parallel hydrophilic filaments, but produces a maximum for crossing filaments. The liquid volume at the maximum force is reported when changing the filament flexibility, crossing angle, and contact angle. These results may be beneficial in applications when the strength and structure of wet fibrous materials are important, such as paper formation and welding of flexible components.

5.3 Introduction

Droplet-on-filament systems have been investigated extensively because of their many applications (Carroll, 1976; Soleimani *et al.*, 2013; Fang *et al.*, 2015). For example, a network of fibres is used in the fog collection apparatus of the cactus stem (Ju *et al.*, 2012), spider silk (Zheng *et al.*, 2010), and manufactured woven meshes (Park *et al.*, 2013), whereas it is also beneficial in controlling evaporation (Duprat *et al.*, 2013; Boulogne *et al.*, 2015). Furthermore, a droplet on a filamentous network can be responsible for the hierarchical helical structures observed in nature (Pokroy *et al.*, 2009), the bundles of wet hair (Bico *et al.*, 2004), and the water repellency of feathers (Rijke & Jesser, 2010).

Advances in micro- and nanoscale technology bring increasing attention to surface-tension-driven deformations of elastic solids, i.e., 'elasto-capillarity', because the deformations are dominated by surface forces rather than body forces (Roman & Bico, 2010; Liu *et al.*, 2012). The liquid-droplet shape between two parallel solid fibres has been studied for decades (Princen, 1970; Wu *et al.*, 2010), and recently was used to control evaporation (Duprat *et al.*, 2013) and liquid delivery (Duprat *et al.*, 2013; Keis *et al.*, 2004). In an array of parallel flexible fibres, elasto-capillarity furnishes several spreading regimes for the liquid, observable on wet feathers (Duprat *et al.*, 2012).

However, fibres in a random network are rarely parallel or clamped at one end. Therefore, studying the droplet shape between crossing fibres is essential for understanding the capillary impact on fibrous materials when exposed to moisture. Surface tension can attach or detach crossing fibres, which is important in many applications, such as the textile wetting and drying (Patnaik *et al.*, 2006), paper drying (Persson *et al.*, 2013), filtration and separation of two immiscible liquids (Contal *et al.*, 2004; Eral *et al.*, 2011*b*), electrical resistance and rheology of fibrous materials (Wu *et al.*, 2012; Skelton, 1975), and nanoparticle assembly (Min *et al.*, 2008). Such fibre deformations can cause surface-adhesion-driven collapse (Wu & Dzenis, 2007) and affect the bulk properties of fibrous materials (Wu & Dzenis, 2005).

Virozub *et al.* (2009) numerically investigated the liquid bridges between two identical cylinders at a fixed separation and inclination. With a large distance between the cylinders, the liquid bridge was symmetric, and the filaments were attracted by capillary forces. However, separation reduction at large contact angles furnished stable and apparently unstable solutions with near-zero attractive and repulsive forces, respectively. Bedarkar & Wu (2009) studied the capillary torque on the same geometry, with a similar method, which explains the role of capillarity on the alignment of wet rod-like particles and on the distortion of fibre networks in sensor grids and textiles. Claussen (2011) proposed an analytical description for a liquid column between two identical filaments with a small finite crossing angle, and compared the results with numerical solutions, characterizing the capillary torque as a power law, which is valid for a very wide range of crossing angles. Sauret *et al.* (2014) investigated the different morphologies of a perfectly wetting fluid lying at the intersection of two fibres with a small crossing angle. These morphologies are a liquid column, a droplet, and a mixed morphology where a drop lies at the end of a column. Nevertheless, the effect of the surface-tension-driven deformation of the filaments was not considered.

In this work, I study the capillary force and torque produced by a liquid bridge between two elastically-deformed filaments, calculating the equilibrium value using an iterative method. I compute an analytical solution for parallel filaments using an analytical approximation for the liquid bridge between two parallel curved cylinders. The analytical solution is then compared with a numerical solution, which is readily extended for crossing filaments. My main motivation is to calculate capillary forces between wood fibres in a wet paper, which has been shown to account for its strength when containing less than 40% solids (van de Ven, 2008). Such forces have been shown to bring the fibres into molecular contact during drying (Persson *et al.*, 2013).

5.4 Theory

5.4.1 Parallel filaments

Consider a liquid drop bridging two parallel filaments (see Figure 5.1), where their diameters are $2r$ and their surface-to-surface distance is $2d$. At equilibrium, the liquid bridge must

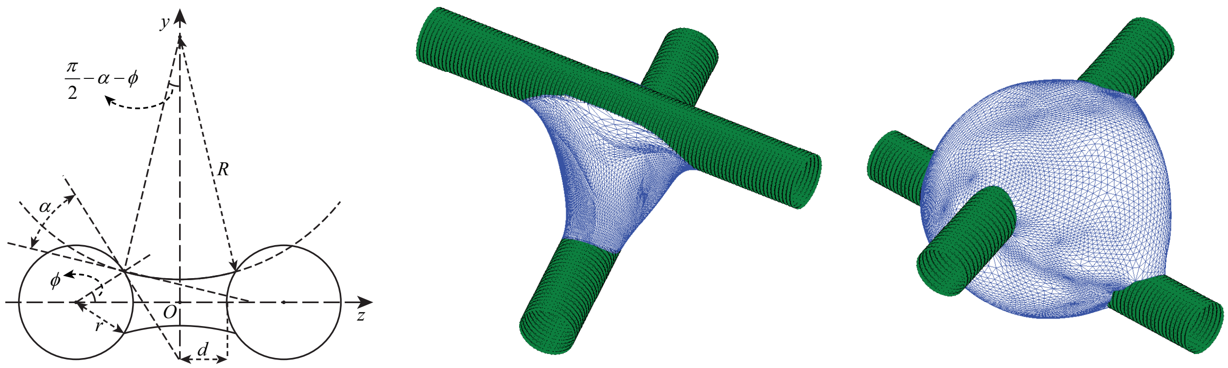

Figure 5.1: Left: Schematic of the cross-section of the liquid column between two parallel filaments showing the various geometrical parameters. Right: The three-dimensional visualization of a liquid bridge (left) and a liquid droplet (right) at the intersection of two crossing filaments.

satisfy the Laplace condition on its surface,

$$p_0 - p = \gamma \left(\frac{1}{R_1} + \frac{1}{R_2} \right), \tag{5.1}$$

and the Dupre-Young condition on its contact line,

$$\gamma \cos \alpha = \gamma_{sg} - \gamma_{sl}, \tag{5.2}$$

where R_1 and R_2 are the principal radii of curvature, p and p_0 are the liquid and gas pressures, γ_{sl}, γ_{sg}, and γ are the solid-liquid, solid-gas, and liquid-gas interfacial tensions, and α is the equilibrium contact angle. These conditions can be derived from the principle of stationary potential energy under constant-volume variations (Myshkis *et al.*, 1987). The Laplace equation is a nonlinear partial differential equation, and is usually solved analytically in two-dimensional geometries, such as axisymmetric or constant cross-sectional interfaces. Princen (1970) assumed a constant cross-section for a long liquid column that bridges two parallel horizontal filaments to derive an analytical solution by balancing the increase in the free energy with the work of the capillary pressure, when the liquid volume is increased infinitesimally. As shown in Figure 5.1, the filament separation

$$d = R \cos(\alpha + \phi) + r \cos \phi - r, \tag{5.3}$$

where R is the interface radius of curvature, and ϕ is the half-opening angle of the solid-liquid interface. The Princen model has been modified for fibres with a small finite inclination angle δ, where d varies slowly along the fibres. This modified model agrees with experimental (Sauret *et al.*, 2014) and numerical (Claussen, 2011) results; I extend it for slightly curved parallel fibres with separation

$$d(x) = R(x)\cos[\alpha + \phi(x)] + r\cos\phi(x) - r, \tag{5.4}$$

where x denotes distance along the filament axis (see Figure 5.4). Using the Princen formulation close to the terminal meniscus of the liquid column, I find

$$\left(\frac{R_e}{r}\right)^2\left[\frac{\pi}{2} - \beta + \frac{1}{2}\sin(2\beta)\right] + \frac{2R_e}{r}\left(\sin\phi_e\cos\beta - \phi_e\cos\alpha\right) + \frac{1}{2}\sin(2\phi_e) - \phi_e = 0, \tag{5.5}$$

where $\beta = \alpha + \phi_e$, and R_e and ϕ_e are the interface radius of curvature and opening angle close to the terminal meniscus, respectively. Equations (5.4) and (5.5) give R_e and ϕ_e, which together determine the interface terminal cross-sectional profile. The other principal curvature along the filament axis can be neglected, so R is constant along the liquid column, and $\phi(x)$ is calculated using Eqn (5.4). A prescribed volume then determines the length of the column, and the maximum possible length is when α_e reaches its maximum and the liquid column becomes unstable (Princen, 1970).

5.4.2 Crossing filaments

For a crossing angle $\delta < 10°$, Sauret *et al.* (2014) used the modified Princen model to calculate the length and cross-sectional profile of the long liquid columns. However, this failed to predict the interface shape with small L_i/r, where L_i is the length of the interface, as shown in Figure 5.4, because the interface curvature along the column axis is not constant. This occurs when either the liquid volume decreases or $\delta > 10°$ (Sauret *et al.*, 2014).

For a small liquid bridge between parallel or crossing filaments, I use the Surface Evolver (Brakke, 1992) software to calculate the interface shape, surface energy, and capillary torque and force. This minimizes the total energy of a surface with several constraints. The surface is discretized into points and edges that form triangles termed facets, and the constraints are implemented using Lagrange multipliers. The initial geometry is a distorted rectangular prism that is continuously refined after converging at each step to form a uniform dense mesh, giving first-order convergence of the energy with respect to the number of facets. The convergence criterion is when the energy change at each iteration is less than 7 significant digits with more than 60 000 facets.

Results from Surface Evolver with solid parallel cylinders are compared with the Princen model in Figure 5.2. Note that the numerical results deviate from the theory when $L_i/d < 6$. Furthermore, the Princen model predicts that a liquid column becomes unstable when $d/r > \sqrt{2}$ and $\alpha = 0$, while Surface Evolver provides stable solutions with $d/r > \sqrt{2}$ when the length of the liquid column is small, but does not converge for long columns. In this paper, I use the Princen model when $L_i/d > 6$.

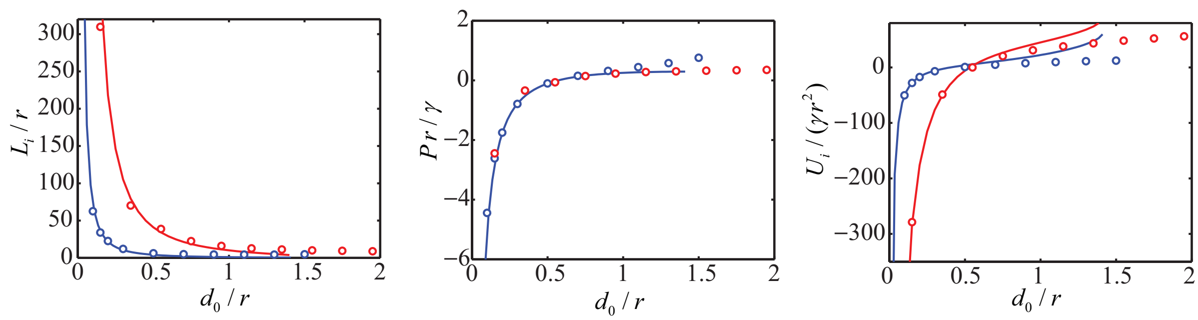

Figure 5.2: Comparison of the analytical Princen model (solid lines) and numerical Surface Evolver (symbols) calculations of a liquid column between two parallel solid filaments showing the length L_i, capillary pressure P, and surface energy U_i versus the filament separation d when $\alpha = 0$, $V/r^3 = 10$ (blue), and 100 (red).

Another configuration of a liquid droplet on an array of parallel filaments is a barrel-shaped droplet. Princen (1970) experimentally showed the existence of these metastable configurations when $0.57 < d/r < \sqrt{2}$, and Wu *et al.* (2010) numerically showed a transition from a bridge to a droplet when increasing the liquid volume, with a critical volume that depends on the contact angle and filament separation. However, there is no analysis for this transition for crossing filaments, as shown in Figure 5.1, except a qualitative description by Claussen (2011). Therefore, based on the results of Wu *et al.* (2010) for parallel filaments, I limit this analysis to small liquid volumes, small filament separations, and $\alpha \leq 90°$, focusing on liquid bridges.

The capillary force F_i and torque M_i are the surface-energy gradients with respect to separation and rotation, respectively, which I calculate using central finite-differences. The forces and torques were validated using the results of Bedarkar & Wu (2009) and Virozub *et al.* (2009).

5.4.3 Elastic filaments

When a bending moment M is applied to a linearly elastic filament, it satisfies

$$\frac{1}{\rho} = \frac{M}{EI}, \tag{5.6}$$

where ρ is the radius of curvature of the deflected filament, and EI is the flexural rigidity. For small deflections, $1/\rho \approx \mathrm{d}^2v/\mathrm{d}x^2$, where v is the deflection and x is defined in Figure 5.4, so

$$M = EI\frac{\mathrm{d}^2v}{\mathrm{d}x^2}. \tag{5.7}$$

To calculate M, the distribution of the capillary force on the filament should be computed first. For example, using the modified Princen model for a long liquid column between curved parallel cylinders, the force on a differential element of the filament is

$$\frac{\mathrm{d}F_i}{\gamma r} = 2\left\{\frac{r}{R}\sin\phi(x) + \sin[\alpha + \phi(x)]\right\}\frac{\mathrm{d}x}{r}, \tag{5.8}$$

where R is constant, and ϕ changes along the interface. The first and the second terms on the right-hand side represent the contributions of the capillary pressure and the surface-tension force, respectively. Equation 5.8 is not valid for small liquid bridges. When the filaments are rotated and deflected, it becomes extremely difficult to compute the force distribution and filament deformation. Figure 5.3 shows the shape of the solid-liquid interface when rotating crossed filaments. Note that the width of the contact region is almost constant along the filament axis when $\delta = 0°$ and $90°$, except when close to the terminal meniscus. However, the contact region does not have uniform width when $\delta = 30°$ and $60°$, since the solid-liquid interface deforms around the filament, producing an azimuthal force and an accompanying capillary torque.

To simplify the model, I use a linear force distribution in the xy- and xz-planes for the capillary torque and force, respectively, as shown in Figure 5.4. Therefore, the force on a differential element is

$$\begin{aligned} \frac{\mathrm{d}F_{iz}}{\gamma r} &= f_i\mathrm{d}x, \\ \frac{\mathrm{d}F_{iy}}{\gamma r} &= \frac{2m_i x\mathrm{d}x}{L_i}, \end{aligned} \tag{5.9}$$

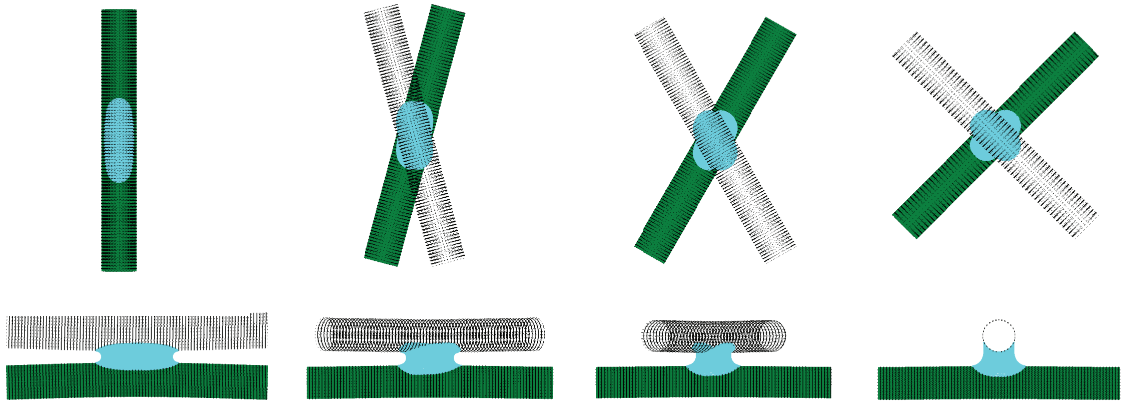

Figure 5.3: Top and accompanying side views when increasing the crossing angle $\delta = 0°$, $30°$, $60°$, and $90°$ (left to right) with $\alpha = 0°$, $V/r^3 = 4$, $d_0/r = 0.5$, $\Omega = 5000$.

where F_{iz} and F_{iy} are the capillary forces in z- and y-directions, respectively, giving

$$f_i = \frac{F_i}{\gamma L_i}, \quad m_i = \frac{6M_i}{\gamma L_i^2}. \tag{5.10}$$

Although the uniform force distribution significantly reduces the computational cost, the errors are expected to decrease with increasing slenderness of the solid-liquid interface, and when L_i is small compared to the filament length.

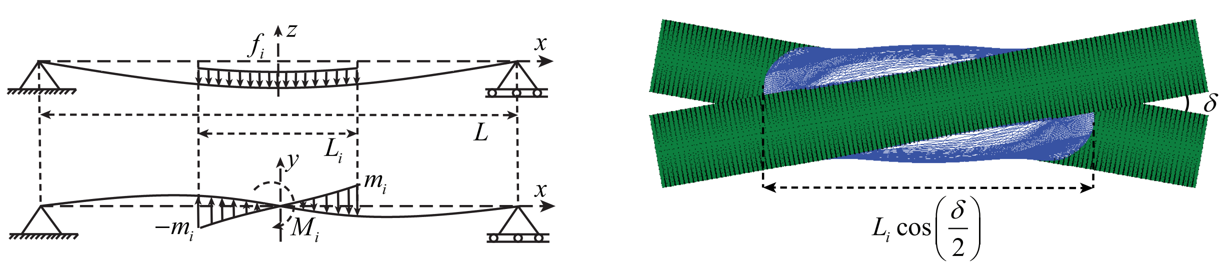

Figure 5.4: Left: Schematic of the filament deformation under capillary force in xz-plane and capillary torque in xy-plane, having simple supports at both ends. Right: The top view with the liquid bridge at the node, showing the inclination angle δ and the liquid-bridge length L_i.

The filament is on two simple supports that mimic the connections among fibres in a fibre network, and L is a free length, where a fibre has no contact with other fibres. In this paper, I fix $L/r = 15$ to remove one degree of freedom, simplifying the model. With this load distribution and boundary conditions, the filament deflection is calculated using Eqn (5.7). The deflected-filament centerline along the liquid bridge is[1]

$$\begin{aligned} z(x) &= b_4 x^4 + b_2 x^2 + b_0, \\ y(x) &= c_5 x^5 + c_3 x^3 + c_1 x, \end{aligned} \tag{5.11}$$

where x, y, and z are normalized with r, and

$$\begin{aligned} b_4 &= \frac{f_i r^3}{24\Omega L^3}, \\ b_2 &= \frac{f_i L_i r}{16\Omega L^3}(L_i - 2L), \\ b_0 &= \frac{f_i L_i}{384\Omega L^3 r}(L_i^3 - 4L_i^2 L + 8L^3), \\ c_5 &= \frac{m_i r^4}{60\Omega L_i L^3}, \\ c_3 &= \frac{m_i L_i r^2}{72\Omega L^4}(2L_i - 3L), \\ c_1 &= \frac{m_i L_i^2}{2880\Omega L^4}(40L^2 - 45L_i L + 12L_i^2), \end{aligned} \tag{5.12}$$

where

$$\Omega = \frac{EI}{\gamma L^3} \tag{5.13}$$

is the elasto-capillary number. The strain energy of the deflected filament is

$$\frac{U_e}{\gamma r^2} = \frac{f_i^2 L_i^2}{490\Omega L^3 r^2}(5L^3 - 5LL_i^2 + 2L_i^3) + \frac{m_i^2 L_i^4}{30240\Omega L^4 r^2}(35L^2 - 54LL_i + 21L_i^2). \tag{5.14}$$

An iterative method is used to find the filament-interface equilibrium. First, I calculate $F_i/\gamma r$ and $M_i/\gamma r^2$ for unstrained filaments, which cause deflection. Then the deflected filaments are used in the next iteration to calculate the force and torque until their absolute change in successive iterations is less than 0.01.

[1] A different solution for the filament deflection outside of the liquid bridge is calculated, and the two solutions are matched at the contact line.

5.5 Results and discussion

The results of the modified Princen model for the elastic parallel filaments are compared with Surface Evolver results in Figure 5.5. With $d/r = 0.1$, analytical and numerical results are in good agreement, but deviate when $d/r = 0.5$, either because the increased variation of d along the filaments contradicts the assumptions, or because the terminal meniscus becomes important. However, the modified Princen model is still a good approximation for $d/r = 0.5$, achieving less than 15% relative error in $F_i/(\gamma r)$, L_i/r, and $U_t/(\gamma r^2)$. Note that, with flexible filaments, d/r is the initial separation of the unstrained filaments.

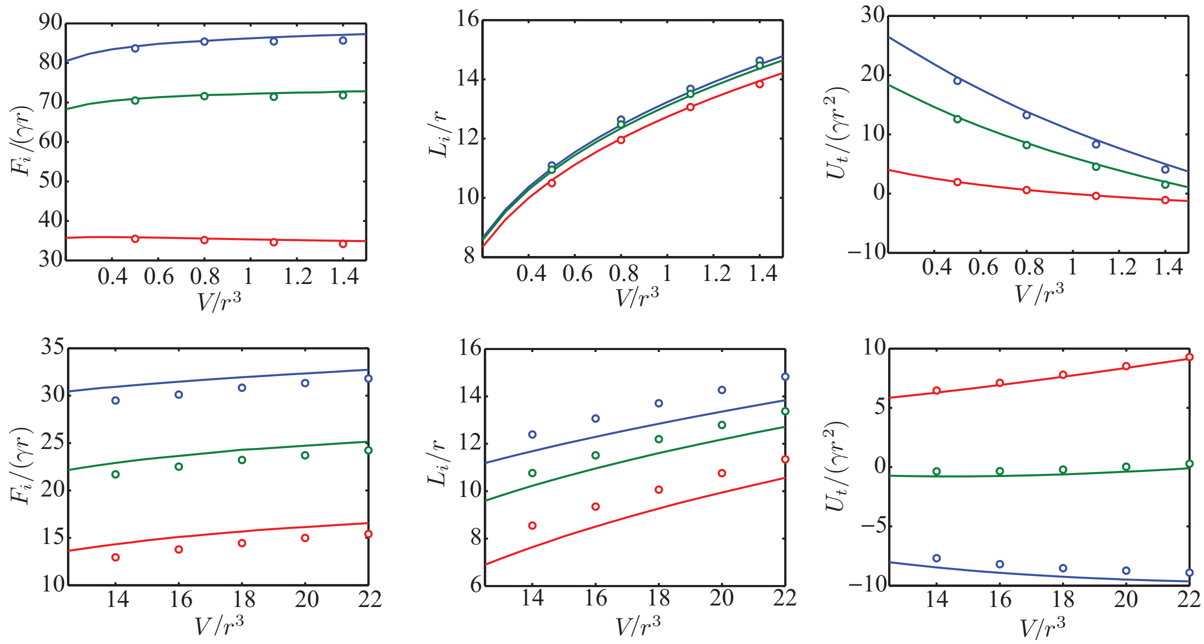

Figure 5.5: The analytical Princen-model results (solid lines) of the capillary force, length of the liquid column, and total energy versus the liquid volume for the parallel flexible filaments compared with the numerical results from Surface Evolver (symbols). Top: $d/r = 0.1$, $\Omega = 1.481$, $\alpha = 0°$ (blue), $30°$ (green), and $60°$ (red). Bottom: $d/r = 0.6$, $\Omega = 1.481$, $\alpha = 0°$ (blue), $30°$ (green), and $45°$ (red).

Analytical results for parallel elastic filaments are shown in Figure 5.6. With the stated elasto-capillary numbers and contact angles, the filaments contact each other at equilibrium when $d/r = 0.1$, while there is no contact when $d/r = 0.5$. The volume is increased until the length of the liquid column becomes close to the length of the filaments ($L/r = 15$). The capillary force continuously increases with volume, only reaching a maximum when $d/r = 0.1$ and $\alpha = 60°$. Therefore, the capillary force among hydrophilic parallel filaments is unlikely to show a maximum when the liquid volume varies. The length of the liquid column increases with volume, as expected, but the total energy can increase or decrease depending on α and Ω. Furthermore, the capillary force and the length of the liquid column decrease when increasing Ω. This decrease is negligible with the attached filaments $d/r = 0.1$, but is significant with detached filaments $d/r = 0.5$.

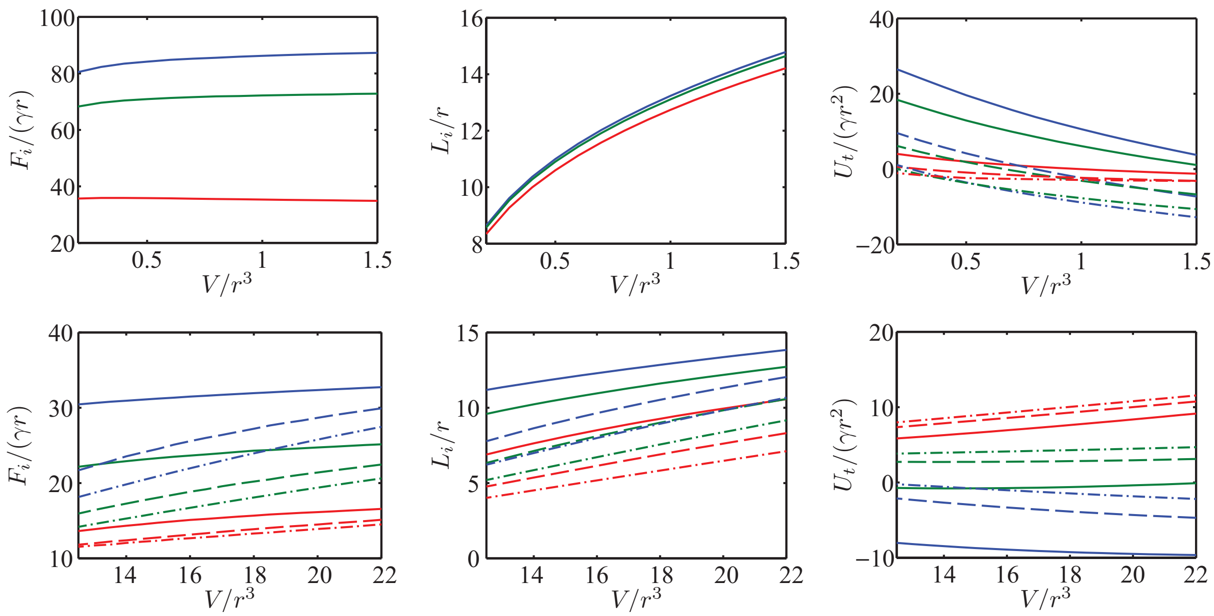

Figure 5.6: Analytical calculation of the capillary force, length of the liquid column, and total energy versus the liquid volume for parallel flexible filaments. $\Omega = 1.481$ (solid lines), 2.963 (dashed lines), and 5.926 dash-dotted lines. Top: $d/r = 0.1$, $\alpha = 0°$ (blue), 30° (green), and 60° (red). Bottom: $d/r = 0.6$, $\alpha = 0°$ (blue), 30° (green), and 45° (red). In the first two plots of the top panel, the solid, dashed, and dash-dotted lines are very close to each other, and so only one is shown.

The equilibrium capillary force of the crossing filaments when changing the elasto-capillary number is shown in Figure 5.7. The black line shows the force required for the filaments to contact each other; thus, filaments touch when the points are above this line. Note that, with $d/r = 1.5$, the black line is not shown, because the forces are very small, and there is no contact. It is obvious from Figure 5.7 that the capillary force decreases when increasing the contact angle and inclination angle. With $\alpha = 30°$ and $d/r = 0.5$, there is a rapid decrease in the force with increasing Ω when the filaments detach. This decrease is also observed for $\alpha = 60°$, and with a smaller slope when $d/r = 0.1$. However, the capillary force reaches a plateau when Ω is large. With $\alpha = 90°$, the force does not vary significantly when changing inclination angle. Furthermore, it decreases and becomes repulsive when the filaments become very close (see $d/r = 0.1$).

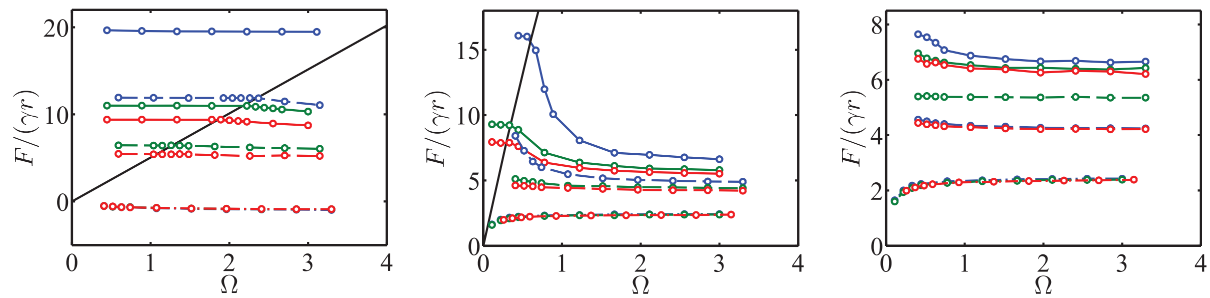

Figure 5.7: Numerical calculation of the capillary force versus the elasto-capillary number for crossed flexible filaments. From left to right: $d/r = 0.1$, $d/r = 0.5$, and $d/r = 1.5$. Solid lines: $\delta = 30°$, dashed lines: $\delta = 60°$, dash-dotted lines: $\delta = 90°$. Blue: $\alpha = 0°$, green: 45°, and red: 90°. The black solid lines show the critical force required for filament attachment. In the right panel, this line is very close to the vertical axis, and it is not shown.

The numerical results for the equilibrium capillary force of the crossing filaments versus the liquid volume are shown in Figure 5.8. Note that, except for $d/r = 1.5$, the force increases when decreasing volume, and, therefore, in contrast to parallel filaments, reaches a maximum, because the capillary force vanishes at $V = 0$. This agrees with the experiments of de Oliveira *et al.* (2008) for two wet paper sheets held together by capillary forces between (mostly) crossed wood fibres. This force goes through a maximum, and then vanishes as the water volume decreases. The maximum is obvious in Figure 5.8 when $\alpha = 90°$ and $\delta = 45°, 90°$. In these figures, the filaments touch when $d/r = 0.1$, and there is no contact when $d/r = 1.5$. When $d/r = 0.5$, the filaments are in contact above the black line, and there is no contact below it; consequently, the maximum may exist in both conditions.

The liquid volume of the maximum capillary force between the crossing filaments V_m is calculated with various d/r, Ω, α, and ϕ, and is plotted versus Ω in Figure 5.9. With small Ω, when the filaments are deformed and attached, V_m slightly increases with Ω, but significantly increases when the filaments detach. Furthermore, increasing the filament separation slightly changes V_m if the filaments remain attached, but significantly increases V_m if they are detached. Filament rotation seems to have a weak influence on V_m, while increasing contact angle decreases V_m.

Persson *et al.* (2013) showed that the capillary forces between wood fibres in a wet paper sheet pull the fibres into closer contact, and conform their surface profiles to each

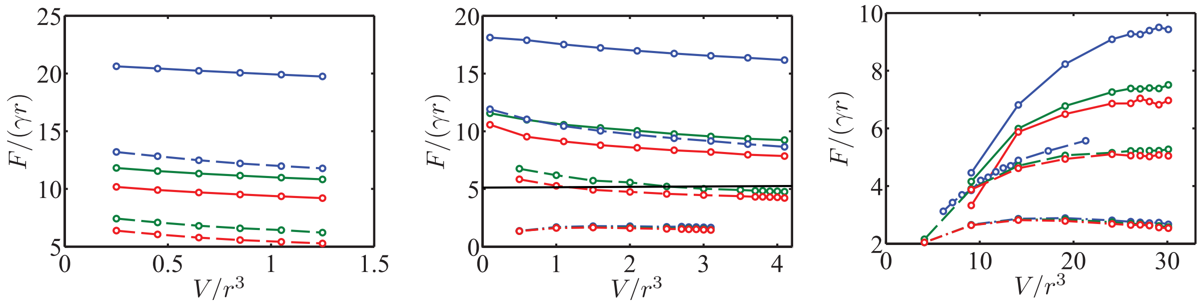

Figure 5.8: Numerical calculation of the capillary force versus the liquid volume for the crossed flexible filaments with $\Omega = 0.207$. From left to right: $d/r = 0.1$, 0.5, and 1.5. $\delta = 30°$ (solid lines), 60° (dashed lines), 90° (dash-dotted lines). $\alpha = 0°$ (blue), 45° (green), and 80° (red). The black solid line in the middle panel is showing the critical force required for filament attachment. Because of numerical instability, no solution can be calculated when $d/r = 0.1$ and $\delta = 90°$, and with large volumes when $d/r = 1.5$ and $\delta = 60°$.

other by breaking and reforming the hydrogen bonds. My calculations may provide a better estimate of the capillary forces between the wood fibres at a specific solid content, which is beneficial in analysing contact between wet fibres. The calculations are also important for finding the optimum weld-metal volume for a desired contact between flexible components.

5.6 Conclusions

The equilibrium shape of a liquid bridge between two crossing or parallel filaments was calculated iteratively when the filaments are deformed by the capillary force and torque. The capillary torque and force are the energy gradients with respect to rotation and separation, respectively. For parallel filaments, I used an analytical approximation for the interface shape and computed the equilibrium analytically, while the Surface Evolver software was also used to numerically calculate the interface shape. Numerical and analytical results agreed well. Surface Evolver was also used for the liquid bridge between crossed filaments, as no analytical solution is available. In the investigated range of parameters, the capillary force decreases when decreasing the liquid volume for parallel filaments, but has a maximum for crossed filaments. The volume at which the peak force occurs slightly varies when the filaments are attached, but significantly changes with the filament flexibility and separation when they are detached. This volume is a weak function of rotation. A significant decrease in the capillary force is predicted when the filaments detach from each other

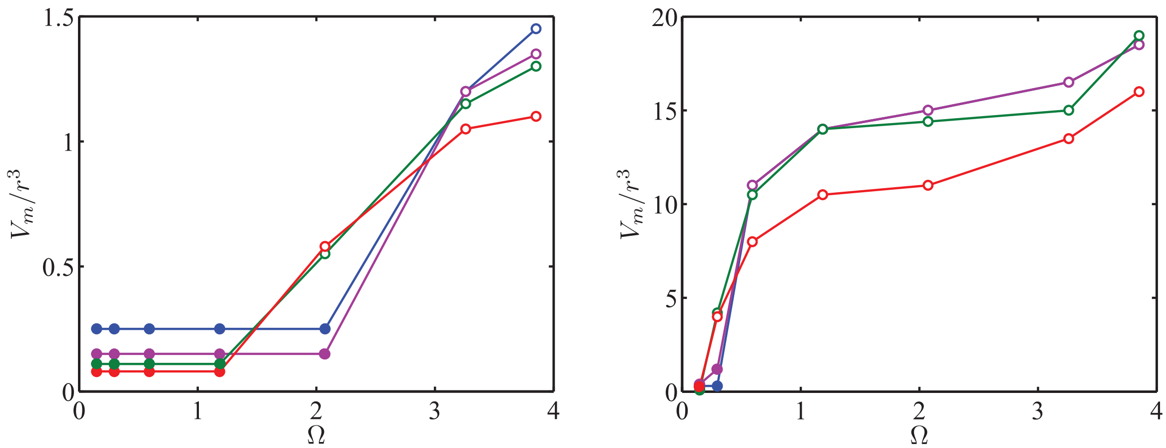

Figure 5.9: Numerical calculation of the liquid volume of the maximum force versus the elasto-capillary number. The filled symbols correspond to attached filaments and empty symbols are for detached filaments. Left: $d/r = 0.1$ and right: $d/r = 0.6$. Blue: $\delta = 45°$, $\alpha = 0°$, purple: $\delta = 90°$, $\alpha = 0°$, green: $\delta = 45°$, $\alpha = 45°$, red: $\delta = 90°$, $\alpha = 45°$.

as the filament flexibility decreases. These results are consistent with the experimental observations of the maximum capillary force between wet paper sheets, and are useful for analysing the contact between flexible components, in welding and in wet paper.

Chapter 6

Conclusions

The capillary-driven deformations of wood fibres during drying were investigated quantitatively, using analytical, numerical, and experimental approaches. Fibres were modeled with smooth circular tubes with a constant cross section and contact angle. First, the shape of a liquid drop or a gas bubble inside or outside of these tubes was calculated. Then, elastic deformation of the tubes was coupled with numerical solutions of the drop shape to calculate the equilibrium, when the drop is either inside the tube or between different tubes. The results enhance our understanding of the role of capillarity in wood-fibre dimensional changes during drying, particularly, lumen collapse and fibre entanglements in a network. My analyses are beneficial in many other applications, including contact-angle measurement, lung airway closure, and nano-particle assembly.

In Chapter 3, an analytical approximation was calculated for the shape of a liquid droplet or a gas bubble on a curved substrate in the absence of gravity. Considering a spherical cap on a flat substrate, a non-axisymmetric perturbation was added to the substrate, which leads to a modification to the drop profile. The perturbed profile showed a singularity at its maximum radius when the contact angle exceeds $90°$, which was removable by reformatting the solution close to the maximum radius. The perturbation solution also gave expressions for the Laplace pressure and surface energy, showing that they change only with the axisymmetric part of the perturbation. As an example, the solution was used to calculate the shape of a drop either inside or outside of a circular tube, and the results were compared with the numerical calculations from Surface Evolver software. The perturbed drop profile, Laplace pressure, and surface energy showed good correspondence with numerical calculations, although they deviated gradually when the perturbation parameter was increased. It was observed that the Laplace pressure and surface energy increase with the substrate curvature when the drop is outside the tube, and decrease when inside the tube. The change in the Laplace pressure deceased with increasing contact angle, but the change in the surface energy showed a peak at 90° contact angle. Because the surface-energy change was a function of substrate curvature, a gradient of substrate curvature could induce an energy gradient that produces a force on the drop and can lead to drop migration. For example, I calculated a drop profile on a harmonic surface, and predicted that the most energetically favoured (stable) positions for drops are the surface valleys. Surface Evolver results also showed that the drop migrates to the surface valleys, when it is arbitrarily deposited on the harmonic surface. Furthermore, I calculated the viscous resistance against the drop migration using a lubrication approximation, and balanced it with the energy-gradient force to compute the drop velocity. This velocity increased with the surface-curvature gradient, contact angle, and drop radius.

This perturbation solution is also beneficial to papermaking applications. For example, it is possible to fit this solution to the drop profile on a wood fibre to measure the contact angle. Furthermore, the perturbed capillary pressure gives a more realistic estimate of the Laplace pressure on wood fibres during drying. The surface energy of the perturbed drop determines the most stable locations for a liquid droplet or a gas bubble inside or outside of the wood fibres during drying.

In Chapter 4, cross-sectional deformations of an initially circular tube were analysed when it is subjected to a capillary pressure induced by a meniscus pinned to a small hole in the tube wall. An analytical solution of the tube buckling was coupled to the numerical calculations of the interface shape from the Surface Evolver software to compute the equilibrium configurations as the liquid volume was decreasing. The theoretical results predicted that if a stable bridge is formed when the interface touches the opposite tube wall, then further reductions of the liquid volume lead to complete tube collapse. I obtain characteristic curves for various hole diameters in the contact angle-elasto-capillary number space, separating the collapsing and non-collapsing regimes. After testing this diagram with experimental results, I tried to use my theory for real wood fibres. I used a range for the fibre dimensions and Young's modulus from the wood-fibre literature to calculate a range for the elasto-capillary number of wood fibres, and concluded that capillary forces may flatten wood fibres completely or partially during drying, depending on the physical, chemical, and geometrical properties of the fibres.

This analysis enhances our understanding of how capillarity affects the wood-fibre lumen collapse, beside other external loads such as pressing. The results are beneficial in finding strategies to control the lumen collapse, because both open- and closed-lumen fibres are technologically important. For example, it was quantitatively shown that increasing contact angle and Young's modulus increases the fibre resistance to capillary-driven collapse. This suggests the use of mechanical fibres to produce open-lumen fibres, because the more lignin in the walls of the mechanical fibres leads to a more hydrophobic and less flexible fibre. Some other strategies to prevent capillary-driven collapse are to increase the pit-hole diameter, to coat the fibres to increase the contact angle, and to use latewood fibres with thicker walls.

In Chapter 5, the capillary force imposed by a liquid bridge between two flexible fibres was investigated. The elastic deformations of the fibres were calculated analytically, and the liquid-bridge shape, surface energy, and Laplace pressure were calculated using the Surface Evolver software. After coupling the two solutions, the equilibrium was calculated iteratively. The force and torque that are imposed to the fibres by the bridge were the surface-energy gradients with respect to the separation and rotation, respectively. The interface shape between curved parallel fibres was computed analytically by extending the analytical approximation of a liquid column between rigid parallel fibres. Consequently, the equilibrium configuration of parallel flexible fibres was computed analytically, and showed a good correspondence to the numerical calculations. The numerical method was also used for crossing fibres where no analytical solution is available. In the investigated range of parameters, the capillary force decreased with decreasing the liquid volume when the fibres were parallel, but went through a maximum when they are non-parallel. When the capillary force attached the fibres to each other, the capillary force and the liquid volume of the peak force slightly changed with the fibre rotation, separation and flexibility. However, significant changes in the force and liquid volume were observed when the fibres detached. These calculations are in agreement with the experimental observation of a maximum attractive capillary force between two wet paper sheets, and estimate the force applied on wood fibres by the liquid bridges at the intersections. This force has been shown to pull the fibres into a molecular contact and to conform their surfaces to each other, which leads to a stronger bonding.

6.1 Applications and future work

Chapter 3 can be used to measure contact angle on curved surfaces. Therefore, the current investigation can be extended to include the effect of gravity, roughness, and variable contact angle by adding further perturbations to the equations. My analysis on drop propulsion driven by substrate curvature can be extended to design a drop motion in lab-on-chip or heat exchangers, for example, to refresh and clean an area in a microscopic scale. By adding the effect of friction, it is possible to calculate the critical volume where the droplet or bubble begins migration. Chapter 4 beneficial in pulp and paper industry to choose a suitable kind of wood fibre for a particular application. It can be used to design a procedure to control wood-fibre collapse by improving the fibre properties. The effects of other parameters, such as pressing or the existence of other fibres, on wood-fibre collapse can also be investigated as a continuation of this work. Chapter 5 can be extended to analyse the effect of moisture on the reology and strength of fibrous materials such as a wet papersheet. My investigation is for a limited range of parameters. Therefore, new investigations are required for a wider range of parameters. It is also possible to include the effect of moisture on the elastic properties of the filaments, which occurs, for example, in a papersheet.

References

ADUSUMALLI, R.-B., MOOK, W., PASSAS, R., SCHWALLER, P. & MICHLER, J. 2010 Nanoindentation of single pulp fibre cell walls. *J. Mater. Sci.* **45** (10), 2558–2563.

ALMEIDA, A. B., BULDYREV, S. V. & ALENCAR, A. M. 2013 Crackling sound generation during the formation of liquid bridges: A lattice gas model. *Phys. A.* **392** (16), 3409 – 3416.

ARISTOFF, J. M., DUPRAT, C. & STONE, H. A. 2011 Elastocapillary imbibition. *Int. J. Non Linear Mech.* **46** (4), 648–656.

BASHFORTH, F. & ADAMS, J. C. 1883 *An attempt to test the theories of capillary action: by comparing the theoretical and measured forms of drops of fluid*. University Press.

BATENI, A., SUSNAR, S., AMIRFAZLI, A. & NEUMANN, A. 2003 A high-accuracy polynomial fitting approach to determine contact angles. *Colloids Surf. A* **219** (1), 215–231.

BAUDOIN, M., SONG, Y., MANNEVILLE, P. & BAROUD, C. N. 2013 Airway reopening through catastrophic events in a hierarchical network. *Proc. Nat. Acad. Sci.* **110** (3), 859–864.

BEDARKAR, A. & WU, X.-F. 2009 Capillary torque in a liquid bridge between two angled filaments. *J. Appl. Phys.* **106** (11), 113527.

BEDARKAR, A., WU, X.-F. & VAYNBERG, A. 2010 Wetting of liquid droplets on two parallel filaments. *Appl. Surf. Sci.* **256** (23), 7260–7264.

BERTRAM, C. 1987 The effects of wall thickness, axial strain and end proximity on the pressure-area relation of collapsible tubes. *J. Biomech.* **20** (9), 863–876.

Bico, J., Roman, B., Moulin, L. & Boudaoud, A. 2004 Adhesion: elastocapillary coalescence in wet hair. *Nature* **432** (7018), 690–690.

Bigelow, W., Pickett, D. & Zisman, W. 1946 Oleophobic monolayers: I. films adsorbed from solution in non-polar liquids. *Coll. Sci.* **1** (6), 513–538.

Bledzki, A. K., Sperber, V. & Faruk, O. 2002 *Natural and wood fibre reinforcement in polymers*, , vol. 13. iSmithers Rapra Publishing.

Boulogne, F., Sauret, A., Soh, B., Dressaire, E. & Stone, H. A. 2015 Mechanical tuning of the evaporation rate of liquid on crossed fibers. *arXiv preprint arXiv:1501.01575* .

Brakke, K. A. 1992 The surface evolver. *Exp. Math.* **1** (2), 141–165.

Brakke, K. A. 2008 *Surface Evolver Manual*. Mathematics Department Susquehanna University.

Brodribb, T. J. & Holbrook, N. M. 2005 Water stress deforms tracheids peripheral to the leaf vein of a tropical conifer. *Plant Physiol.* **137** (3), 1139–1146.

Bush, J. W., Peaudecerf, F., Prakash, M. & Quéré, D. 2010 On a tweezer for droplets. *Adv. Colloid Interface Sci.* **161** (1), 10–14.

Butt, H.-J. & Kappl, M. 2009 *Surface and interfacial forces*. John Wiley & Sons.

Campbell, W. B. 1933 *The cellulose-water relationship in papermaking.*. Forest SerVice Bulletin 84; Department of the Interior: Ottawa, Canada.

Carroll, B. J. 1976 The accurate measurement of contact angle, phase contact areas, drop volume, and laplace excess pressure in drop-on-fiber systems. *J. Colloid Interface Sci.* **57** (3), 488–495.

Carroll, B. J. 1986 Equilibrium conformations of liquid drops on thin cylinders under forces of capillarity. a theory for the roll-up process. *Langmuir* **2** (2), 248–250.

Chakrapani, N., Wei, B., Carrillo, A., Ajayan, P. M. & Kane, R. S. 2004 Capillarity-driven assembly of two-dimensional cellular carbon nanotube foams. *Proc. Natl. Acad. Sci. U.S.A.* **101** (12), 4009–4012.

Chesters, A. K. 1977 An analytical solution for the profile and volume of a small drop or bubble symmetrical about a vertical axis. *J. Fluid Mech.* **81** (4), 609–624.

Chou, T.-H., Hong, S.-J., Liang, Y.-E., Tsao, H.-K. & Sheng, Y.-J. 2011 Equilibrium phase diagram of drop-on-fiber: Coexistent states and gravity effect. *Langmuir* **27** (7), 3685–3692.

Clark, J. d. 1985 *Pulp technology and treatment for paper*. Miller Freeman Publications.

Claussen, J. O. 2011 Elasticity and morphology of wet fiber networks. PhD thesis, Niedersächsische Staats-und Universitätsbibliothek Göttingen.

Contal, P., Simao, J., Thomas, D., Frising, T., Callé, S., Appert-Collin, J. & Bémer, D. 2004 Clogging of fibre filters by submicron droplets. phenomena and influence of operating conditions. *J. Aerosol Sci.* **35** (2), 263–278.

Daniel, S., Chaudhury, M. K. & Chen, J. C. 2001 Fast drop movements resulting from the phase change on a gradient surface. *Science* **291**, 633–636.

Dulemba, M., Qi, D. & Aravamutha, R. 1999 The effect of repeated drying and wetting on single fiber flexibility. *J. Prog. Pap. Recycl.* **9** (1), 38–45.

Duprat, C., Aristoff, J. M. & Stone, H. A. 2011 Dynamics of elastocapillary rise. *J. Fluid Mech.* **679**, 641–654.

Duprat, C., Bick, A. D., Warren, P. B. & Stone, H. A. 2013 Evaporation of drops on two parallel fibers: Influence of the liquid morphology and fiber elasticity. *Langmuir* **29** (25), 7857–7863.

Duprat, C., Protiere, S., Beebe, A. Y. & Stone, H. A. 2012 Wetting of flexible fibre arrays. *Nature* **482** (7386), 510–513.

Ehrlich, R. 1968 An alternative method for computing contact angle from the dimensions of a small sessile drop. *J. Colloid Interface Sci.* **28** (1), 5–9.

Emerton, H. W. 1957 *Fundamentals of the beating process;: The theory of the development in pulps of papermaking characteristics by mechanical treatment*. British Paper and Board Industry Research Association.

Eral, H. B., Manukyan, G. & Oh, J. M. 2011*a* Wetting of a drop on a sphere. *Langmuir* **27** (9), 5340–5346.

Eral, H. B., de Ruiter, J., de Ruiter, R., Oh, J. M., Semprebon, C., Brinkmann, M. & Mugele, F. 2011*b* Drops on functional fibers: from barrels to clamshells and back. *Soft Matter* **7** (11), 5138–5143.

Extrand, C. W. & Moon, S. I. 2008 Contact angles on spherical surfaces. *Langmuir* **24** (17), 9470–9473.

Fang, J., Davoudi, M. & Chase, G. G. 2015 Drop movement along a fiber axis due to pressure driven air flow in a thin slit. *Sep Purif Technol* **140**, 77–83.

Fischer, W. J., Lorbach, C., Jajcinovic, M., Hirn, U. & Bauer, W. 2014 Measured and calculated bending stiffness of individual fibers. In *Progress in Paper Physics*. Raleigh, North Carolina, USA.

García-Sánchez, P., Ramos, A. & Mugele, F. 2010 Electrothermally driven flows in ac electrowetting. *Phys. Rev. E* **81**, 015303.

Gat, A. & Gharib, M. 2013 Elasto-capillary coalescence of multiple parallel sheets. *J. Fluid Mech.* **723**, 692–705.

de Gennes, P. G. 1985 Wetting: statics and dynamics. *Rev. Mod. Phys.* **57**, 827–863.

de Gennes, P.-G., Brochard-Wyart, F. & Quéré, D. 2004 *Capillarity and wetting phenomena: Drops, bubbles, pearls, waves*. Springer.

Gindl, W. & Schöberl, T. 2004 The significance of the elastic modulus of wood cell walls obtained from nanoindentation measurements. *Composites Part A* **35** (11), 1345 – 1349.

Grotberg, J. B. 1994 Pulmonary flow and transport phenomena. *Annu. Rev. Fluid Mech.* **26** (1), 529–571.

Guilizzoni, M. 2011 Drop shape visualization and contact angle measurement on curved surfaces. *J. Colloid Interface Sci.* **364** (1), 230–236.

Guo, L. & Tang, G. 2015 Experimental study on directional motion of a single droplet on cactus spines. *Int. J. Heat Mass Transfer* **84**, 198–202.

Halpern, D. & Grotberg, J. B. 1992 Fluid-elastic instabilities of liquid-lined flexible tubes. *J. Fluid Mech* **244** (-1), 615–632.

Hauksbee, F. 1710*a* An account of an experiment, concerning the angle requir'd to suspend a drop of oyl of oranges, at certain stations, between two glass planes, placed in the form of a wedge. by mr. fr. hauskbee, frs. *Phil. Trans.* **27**, 473–474.

Hauksbee, F. 1710*b* An account of an experiment touching the ascent of water between two glass planes, in an hyperbolick figure. by mr. francis hauksbee, frs. *Phil. Trans.* **27**, 539–540.

Hayashi, K. & Terazaws, S. 1992 Cell collapse in balsa wood. *Drying Technol.* **10** (5), 1249–1265.

Hazel, A. L. & Heil, M. 2005 Surface-tension-induced buckling of liquid-lined elastic tubes: a model for pulmonary airway closure. *Proc. R. Soc. A* **461** (2058), 1847–1868.

He, J., Batchelor, W. & Johnston, R. 2003 The behavior of fibres in wet pressing. *Tappi J.* **2** (12), 27–31.

Heap, A. & Juel, A. 2009 Bubble transitions in strongly collapsed elastic tubes. *J. Fluid Mech.* **633**, 485–507.

Heil, M. 1999*a* Airway closure: Occluding liquid bridges in strongly buckled elastic tubes. *J. Biomech. Eng.* **121** (5), 487–493.

Heil, M. 1999*b* Minimal liquid bridges in non-axisymmetrically buckled elastic tubes. *J. Fluid Mech.* **380**, 309–337.

Heil, M., Hazel, A. L. & Smith, J. A. 2008 The mechanics of airway closure. *Respir. Physiol. Neurobiol.* **163** (1-3), 214 – 221, respiratory Biomechanics.

Heil, M. & White, J. P. 2002 Airway closure: surface-tension-driven non-axisymmetric instabilities of liquid-lined elastic rings. *J. Fluid Mech.* **462**, 79–109.

Hoorfar, M. & Neumann, A. 2004 Axisymmetric drop shape analysis (adsa) for the determination of surface tension and contact angle. *J. Adhes.* **80** (8), 727–743.

Hu, D. L. & Bush, J. W. M. 2005 Meniscus-climbing insects. *Nature* **437** (7059), 733–736.

Hu, X.-P. & Hsieh, Y.-L. 2001 Effects of dehydration on the crystalline structure and strength of developing cotton fibers. *Textile Res. J.* **71** (3), 231–239.

Hubbe, M. 2007 Bonding between cellulosic fibers in the absence and presence of dry-strength agents - a review. *BioResources* **1** (2), 281–318.

Hubbe, M. & Bowden, C. 2009 Handmade paper: a review of its history, craft, and science. *BioResources* **4** (4), 1736–1792.

Hubbe, M., Venditti, R. & Rojas, O. 2007 What happens to cellulosic fibers during papermaking and recycling? a review. *BioResources* **2** (4), 739–788.

Iliev, S. & Pesheva, N. 2006 Nonaxisymmetric drop shape analysis and its application for determination of the local contact angles. *J. Colloid Interface Sci.* **301** (2), 677–684.

Ilvessalo-Pfäffli, M.-S. 1995 *Fiber Atlas: Identification of Papermaking Fibers (Springer Series in Wood Science)*. Springer.

Innes, T. C. 1995*a* Collapse free pre-drying of eucalyptus regnans f. muell. *Eur. J. Wood Wood Prod.* **53** (6), 403–406.

Innes, T. C. 1995*b* Stress model of a wood fibre in relation to collapse. *Wood Sci. Technol.* **29** (5), 363–376.

Innes, T. C. 1996*a* Collapse and internal checking in the latewood of eucalyptus regnans f.muell. *Wood Sci. Technol.* **30** (6), 373–383.

Innes, T. C. 1996*b* Pre-drying of collapse prone wood free of surface and internal checking. *Eur. J. Wood Wood Prod.* **54** (3), 195–199.

Innes, T. C. & Redman, A. L. 2003 Comparative drying characteristics of six regrowth. australian hardwoods. In *8th International IUFRO Wood Drying Conference*.

Jang, H., Howard, R. & Seth, R. 1995 Fiber characterization using confocal microscopy - the effects of recycling. *Tappi J.* **78** (12), 131–137.

Jang, H. F., Amiri, R., Seth, R. S. & Karnis, A. 1996 Fiber characterization using confocal microscopy - collapse behavior of mechanical pulp fibers. *Tappi J.* **79** (4), 203–210.

Jang, H. F. & Seth, R. S. 1998 Using confocal microscopy to characterize the collapse behavior of fibers. *Tappi J.* **81** (5), 167–174.

Jaron, J. M. & Collicott, S. H. 2008 Two-phase static capillary phenomena in flattened tubes. *Papers AIAA* **15**, 10533–10550.

Joardder, M. U. H., Karim, M. & Kumar, C. 2013 Better understanding of food material on the basis of water distribution using thermogravimetric analysis. In *International Conference on Mechanical, Industrial and Materials Engineering (ICMIME2013)*. Rajshahi University of Engineering & Technology, Rajshahi, Bangladesh, paper ID: AB-052.

Ju, J., Bai, H., Zheng, Y., Zhao, T., Fang, R. & Jiang, L. 2012 A multi-structural and multi-functional integrated fog collection system in cactus. *Nat. Commun.* **3**, 1247.

Kabza, K. G., Gestwicki, J. E. & McGrath, J. L. 2000 Contact angle goniometry as a tool for surface tension measurements of solids, using zisman plot method. a physical chemistry experiment. *J. Chem. Educ.* **77** (1), 63.

Keis, K., Kornev, K. G., Kamath, Y. K. & Neimark, A. V. 2004 Towards fiber-based micro-and nanofluidics. In *Nanoengineered nanofibrous materials*, , vol. 169, p. 175. The Netherlands: Kluwer: Springer.

Kim, H.-Y. & Mahadevan, L. 2006 Capillary rise between elastic sheets. *J. Fluid Mech.* **548** (-1), 141–150.

Kresch, E. 1977 Cross-sectional shape of flexible tubes. *Bull. Math. Biol.* **39** (6), 679–691.

Kresch, E. 1979 Compliance of flexible tubes. *J. Biomech.* **12** (11), 825–839.

Kwok, D., Lin, R., Mui, M. & Neumann, A. 1996 Low-rate dynamic and static contact angles and the determination of solid surface tensions. *Colloids Surf. A* **116** (1), 63–77.

Kwon, S., Stambaugh, C., Kim, B., An, S. & Jhe, W. 2014 Dynamic and static measurement of interfacial capillary forces by a hybrid nanomechanical system. *Nanoscale* **6**, 5474–5478.

LAMBERT, P. 2007 *Capillary forces in microassembly: modeling, simulation, experiments, and case study*. Springer Science & Business Media.

LANGBEIN, D. 2002 *Capillary Surfaces*. Springer-Verlag.

LAPLACE, P. 1806 *Supplement to book 10 of Mecanique Celeste*. Crapelet, Courcier, Bachelier, Paris.

LAU, K. K., BICO, J., TEO, K. B., CHHOWALLA, M., AMARATUNGA, G. A., MILNE, W. I., MCKINLEY, G. H. & GLEASON, K. K. 2003 Superhydrophobic carbon nanotube forests. *Nano letters* **3** (12), 1701–1705.

LEJA, J. & POLING, G. 1960 On the interpretation of contact angle. In *Proceedings of the 5th Mineral Processing Congress*, p. 325.

LIANG, Y.-E., SHENG, Y.-J. & TSAO, H.-K. 2015 Drops on hydrophilic conical fibers: Gravity effect and coexistent states. *Langmuir* **31**, 1704–1710.

LIU, J., ZUO, W. & MEI, Y. 2012 Droplet-induced anomalous deformation of a thin micro-plate. *Colloids Surf., A* **412**, 108–119.

LORENCEAU, É. & QUÉRÉ, D. 2004 Drops on a conical wire. *J. Fluid Mech.* **510**, 29–45.

LOVE, A. E. H. 1893 *A treatise on the mathematical theory of elasticity*. Cambridge: University Press.

LOWE, R., RAGAUSKAS, A. & PAGE, D. H. 2005 Imaging fibre deformations. In *13th, Fundamental Research Symposium; Advances in paper science and technology*, pp. 921–942.

LV, C., CHEN, C., CHUANG, Y.-C., TSENG, F.-G., YIN, Y., GREY, F. & ZHENG, Q. 2014 Substrate curvature gradient drives rapid droplet motion. *Phys. Rev. Lett.* **113** (2), 026101.

MASTRANGELO, C. H. & HSU, C. H. 1993 Mechanical stability and adhesion of microstructures under capillary forces. i. basic theory. *J. Microelectromech. Syst.* **2** (1), 33 –43.

MCHALE, G., NEWTON, M. & CARROLL, B. 2001 The shape and stability of small liquid drops on fibers. *Oil Gas Sci. Technol.* **56** (1), 47–54.

McHale, G. & Newton, M. I. 2002 Global geometry and the equilibrium shapes of liquid drops on fibers. *Colloids Surf. A* **206** (1), 79–86.

Min, Y., Akbulut, M., Kristiansen, K., Golan, Y. & Israelachvili, J. 2008 The role of interparticle and external forces in nanoparticle assembly. *Nat. Mater.* **7** (7), 527–538.

Minor, F., Schwartz, A., Wulkow, E. & Buckles, L. 1959 Part iii: The behavior of liquids on single textile fibers. *Text. Res. J* **29**, 940–949.

Mohlin, U. B. 1975 Cellulose fibre bonding. 5. conformability of pulp fibres. *Sven papperstidn* **78 (11)**, 412–416.

Monica, E., Gellerstedt, G. & Henriksson, G. 2009 *Wood Chemistry and Biotechnology*. De Gruyter.

Moreno, A. H., Katz, A. I., Gold, L. D. & Reddy, R. V. 1970 Mechanics of distension of dog veins and other very thin-walled tubular structures. *Circ. Res.* **27** (6), 1069–1080.

Mugele, F. 2009 Fundamental challenges in electrowetting: from equilibrium shapes to contact angle saturation and drop dynamics. *Soft Matter* **5** (18), 3377–3384.

Myshkis, A. D., Babskii, V. G., Kopachevskii, N. D., Slobozhanin, L. A. & Tyuptsov, A. D. 1987 *Low Gravity Fluid Mechanics*. Springer-Verlag.

Nilsson, B., Wågberg, L. & Gray, D. 2000 Conformability of wet pulp fibres at small length scales. *FSCN/Teknisk fiberkemi* **R-00-6**, 1–16.

O'Brien, S. B. G. 1991 On the shape of small sessile and pendant drops by singular perturbation techniques. *J. Fluid Mech.* **233**, 519–537.

de Oliveira, M. H., Maric, M. & van de Ven, T. G. M. 2008 The role of fiber entanglement in the strength of wet papers. *Nord. Pulp Paper Res. J.* **23** (4), 426–431.

Page, D. H., El-Hosseiny, F. & Winkler, K. 1971 Behaviour of single wood fibres under axial tensile strain. *Nature* **229**, 252 – 253.

Page, D. H., El-Hosseiny, F., Winkler, K. & Lancaster, A. P. S. 1977 Elastic modulus of single wood pulp fibres. *Tappi J.* **60** (4), 114 – 117.

PARK, K.-C., CHHATRE, S. S., SRINIVASAN, S., COHEN, R. E. & MCKINLEY, G. H. 2013 Optimal design of permeable fiber network structures for fog harvesting. *Langmuir* **29** (43), 13269–13277.

PATNAIK, A., RENGASAMY, R. S., KOTHARI, V. K. & GHOSH, A. 2006 Wetting and wicking in fibrous materials. *Textile Progress* **38** (1), 1–105.

PÉRAUD, J.-P. & LAUGA, E. 2014 Geometry and wetting of capillary folding. *Phys. Rev. E* **89**, 043011.

PERSSON, B. N. J., GANSER, C., SCHMIED, F., TEICHERT, C., SCHENNACH, R., GILLI, E. & HIRN, U. 2013 Adhesion of cellulose fibers in paper. *J. Phys. Condens. Matter* **25** (4), 045002.

PIAO, C., WINANDY, J. E. & SHUPE, T. F. 2010 From hydrophilicity to hydrophobicity: a critical review: part i. wettability and surface behavior. *Wood Fiber Sci.* **42** (4), 490–510.

POKROY, B., KANG, S. H., MAHADEVAN, L. & AIZENBERG, J. 2009 Self-organization of a mesoscale bristle into ordered, hierarchical helical assemblies. *Science* **323** (5911), 237–240.

POPOVA, L. N. 1983 Nonaxisymmetric equilibrium shapes of a drop on a plane. *Fluid Dyn.* **18** (4), 634–637.

PRABHALA, B., PANCHAGNULA, M., SUBRAMANIAN, V. R. & VEDANTAM, S. 2010 Perturbation solution of the shape of a nonaxisymmetric sessile drop. *Langmuir* **26** (13), 10717–10724.

PRAKASH, M., QUÉRÉ, D. & BUSH, J. W. 2008 Surface tension transport of prey by feeding shorebirds: the capillary ratchet. *science* **320** (5878), 931–934.

PRINCEN, H. M. 1969*a* Capillary phenomena in assemblies of parallel cylinders: I. capillary rise between two cylinders. *J. Colloid Interface Sci.* **30** (1), 69–75.

PRINCEN, H. M. 1969*b* Capillary phenomena in assemblies of parallel cylinders: Ii. capillary rise in systems with more than two cylinders. *J. Colloid Interface Sci.* **30** (3), 359–371.

Princen, H. M. 1970 Capillary phenomena in assemblies of parallel cylinders: Iii. liquid columns between horizontal parallel cylinders. *J. Colloid Interface Sci.* **34** (2), 171–184.

Protiere, S., Duprat, C. & Stone, H. A. 2013 Wetting on two parallel fibers: drop to column transitions. *Soft Matter* **9** (1), 271–276.

Py, C., Reverdy, P., Doppler, L., Bico, J., Roman, B. & Baroud, C. N. 2007 Capillary origami: Spontaneous wrapping of a droplet with an elastic sheet. *Phys. Rev. Lett.* **98** (15), 156103.

Py, C., Reverdy, P., Doppler, L., Bico, J., Roman, B. & Baroud, C. N. 2009 Capillarity induced folding of elastic sheets. *Eur. Phys. J. Spec. Top.* **166**, 67–71.

Renvoisé, P., Bush, J. W. M., Prakash, M. & Quéré, D. 2009 Drop propulsion in tapered tubes. *Europhys. Lett.* **86** (6), 64003.

Rijke, A. M. & Jesser, W. A. 2010 The feather structure of dippers: water repellency and resistance to water penetration. *Wilson J. Ornothol* **122** (3), 563–568.

Roman, B. & Bico, J. 2010 Elasto-capillarity: deforming an elastic structure with a liquid droplet. *J. Phys Condens Matter* **22** (49), 493101.

Saketi, P., Treimanis, A., Fardim, P., Ronkanen, P. & Kallio, P. 2010 Microrobotic platform for manipulation and flexibility measurement of individual paper fibers. In *Intelligent Robots and Systems (IROS), 2010 IEEE/RSJ International Conference on*, pp. 5762–5767.

Santos, D., Spenko, M., Parness, A., Kim, S. & Cutkosky, M. 2007 Directional adhesion for climbing: theoretical and practical considerations. *J. Adhes. Sci. Technil.* **21** (12-13), 1317–1341.

Sauret, A., Bick, A. D., Duprat, C. & Stone, H. A. 2014 Wetting of crossed fibers: Multiple steady states and symmetry breaking. *EPL* **105** (5), 56006.

Scallan, A. & Tigerström, A. C. 1991 Elasticity of fiber wall; effects of pulping and recycling. In *CPPA 1st Research Forum on Recycling.*, p. 149. Montreal.

Scallan, A. & Tigerström, A. C. 1992 Swelling and elasticity of the cell walls of pulp fibres. *J. pulp pap. sci.* **18** (5), J188–J193.

Segner, J. 1751 De figuris superficierum fluidarum. *Comment. Soc. Reg. Gotting. i.* **1**, 301–372.

Sepke, P. 1991 Current and future technologies of refining conference. *Pira, UK, Paper* **15**.

Shanahan, M. E. 1984 Profile and contact angle of small sessile drops. a more general approximate solution. *J. Chem. Soc., Faraday Trans. I* **80** (1), 37–45.

Skelton, J. 1975 Interfiber forces during wetting and drying. *Science* **190** (4209), 15–20.

Slobozhanin, L. A. & Tyuptsov, A. D. 1974 Stable equilibrium of the surface of a capillary liquid in contact with the edge of a solid. *Fluid Dyn.* **9** (1), 1–3.

Slobozhanin, L. A. & Tyuptsov, A. D. 1975 Evolution and detachment of slowly growing drops and bubbles. *J. Appl. Mech. Tech. Phys.* **16** (1), 83–88.

Smith, P. & Van de Ven, T. 1984 Profiles of slightly deformed axisymmetric drops. *J. colloid interface sci.* **97** (1), 1–8.

Smith, P. G. & van de Ven, T. G. M. 1981 A note on the thermodynamics of partial engulfment. *Colloid Surface* **2** (4), 387–390.

Smithwich, R. W. 1988 Contact-angle studies of microscopic mercury droplets on glass. *J. Colloid Interface Sci* **123** (2), 482–485.

Soleimani, M., Hill, R. J. & van de Ven, T. G. M. 2013 Bubbles and drops on curved surfaces. *Langmuir* **29** (46), 14168–14177.

Srinivasan, S., McKinley, G. H. & Cohen, R. E. 2011 Assessing the accuracy of contact angle measurements for sessile drops on liquid-repellent surfaces. *Langmuir* **27** (22), 13582–13589.

Stalder, A., Kulik, G., Sage, D., Barbieri, L. & Hoffmann, P. 2006 A snake-based approach to accurate determination of both contact points and contact angles. *Colloids Surf. A* **286** (1), 92–103.

Stalder, A. F., Melchior, T., Müller, M., Sage, D., Blu, T. & Unser, M. 2010 Low-bond axisymmetric drop shape analysis for surface tension and contact angle measurements of sessile drops. *Colloids Surf. A* **364** (1), 72–81.

Subramanian, R. S., Moumen, N. & McLaughlin, J. B. 2005 Motion of a drop on a solid surface due to a wettability gradient. *Langmuir* **21** (25), 11844–11849.

Tanaka, T., Morigami, M. & Atoda, N. 1993 Mechanism of resist pattern collapse during development process. *Jpn. J. Appl. Phys.* **32**, 6059.

Tchepel, M., Provan, J. W., Nishida, A. & Biggs, C. 2006 A procedure for measuring the flexibility of single wood-pulp fibres. *Mech. Comp. Mater.* **42** (1), 83–92.

Tejado, A. & van de Ven, T. G. 2010 Why does paper get stronger as it dries? *Mater. Today* **13** (9), 42 – 49.

Timoshenko, S. 1930 *Strength of materials. Part I: Elementary theory and problems.*. D. van Nostrand Co.

Tsai, W. L., Hsu, P. C., Hwu, Y., Chen, C. H., Chang, L. W., Je, J. H., Lin, H. M., Groso, A. & Margaritondo, G. 2002 Electrochemistry: Building on bubbles in metal electrodeposition. *Nature* **417** (6885), 139–139.

van de Ven, T. G. M. 2008 Capillary forces in wet paper. *Ind. Eng. Chem. Res.* **47** (19), 7250–7256.

Virozub, A., Haimovich, N. & Brandon, S. 2009 Three-dimensional simulations of liquid bridges between two cylinders: forces, energies, and torques. *Langmuir* **25** (22), 12837–12842.

Walker, J. C. 2006 *Primary Wood Processing: Principles and Practice*, 2nd edn. Springer.

Weise, U., Maloney, T. & Paulapuro, H. 1996 Quantification of water in different states of interaction with wood pulp fibres. *Cellulose* **3** (1), 189–202.

Wilkes, J. & Wilkins, A. P. 1987 Anatomy of collapse in eucalyptus species. *IAWA BULL n.s.* **8**, 291–295.

Wu, W., Yang, Y., Yuan, Q. & Sun, D. 2013 The collapse of an elastic tube induced by encapsulated liquid droplets. *Soft Matter* **9** (41), 9774–9779.

Wu, X.-F., Bedarkar, A. & Vaynberg, K. A. 2010 Droplets wetting on filament rails: Surface energy and morphology transition. *J. Colloid Interface Sci.* **341** (2), 326–332.

WU, X.-F. & DZENIS, Y. A. 2005 Elasticity of planar fiber networks. *J. Appl. Phys.* **98** (9), 093501.

WU, X.-F. & DZENIS, Y. A. 2006 Droplet on a fiber: geometrical shape and contact angle. *Acta mechanica* **185** (3-4), 215–225.

WU, X.-F. & DZENIS, Y. A. 2007 Collapse analysis of nanofibres. *Nanotechnology* **18** (28), 285702.

WU, X.-F., ZHOU, Z. & ZHOU, W.-M. 2012 Electrical contact resistance in filaments. *Appl. Phys. Lett.* **100** (19), 193115.

YAN, D. & LI, K. 2008 Measurement of wet fiber flexibility by confocal laser scanning microscopy. *J Mater. Sci.* **43** (8), 2869–2878.

YAN, D. & LI, K. 2013 Conformability of wood fiber surface determined by afm indentation. *J. Mater. Sci.* **48** (1), 322–331.

YANG, M.-W. & LIN, S.-Y. 2003 A method for correcting the contact angle from the $\theta/2$ method. *Colloids Surf. A* **220** (1), 199–210.

YANG, Y., GAO, Y. F., SUN, D. Y., ASTA, M. & HOYT, J. J. 2010 Capillary force induced structural deformation in liquid infiltrated elastic circular tubes. *Phys. Rev. B* **81**, 241407.

YAO, Z. & BOWICK, M. J. 2012 Self-propulsion of droplets by spatially-varying surface topography. *Soft Matter* **8** (4), 1142–1145.

YOUNG, T. 1805 An essay on the cohesion of fluids. *Philosophical Transactions of the Royal Society of London* **95**, 65–87.

ZHENG, Y., BAI, H., HUANG, Z., TIAN, X., NIE, F.-Q., ZHAO, Y., ZHAI, J. & JIANG, L. 2010 Directional water collection on wetted spider silk. *Nature* **463** (7281), 640–643.

Appendix A

Solution of the differential equation in chapter 3

Here, I only consider ξ_n, but exactly the same equations hold for η_n. Thus, to solve Eqn. (3.16), I apply the change of variable

$$t = \sqrt{1-r^2}, \quad y_n = \sqrt{1-r^2}\xi_n, \tag{A.1}$$

so Eqn. (3.16) becomes

$$(1-t^2)y_{n,tt} - 2ty_{n,t} + (2 - \frac{n^2}{1-t^2})y_n = 0, \tag{A.2}$$

which is the first degree, nth order associated Legendre equation. The Maple software gives

$$y_n = {C_1}^n (n-t) \left(\frac{1+t}{1-t}\right)^{\frac{n}{2}} + {C_2}^n (n+t) \left(\frac{1-t}{1+t}\right)^{\frac{n}{2}} \tag{A.3}$$

for $n > 1$. Transforming back to the main variables, I have

$$\xi_n = {C_1}^n \frac{\left(n - \sqrt{1-r^2}\right) \left[2(1+\sqrt{1-r^2}) - r^2\right]^{\frac{n}{2}}}{r^n\sqrt{1-r^2}} + {C_2}^n \frac{\left(n + \sqrt{1-r^2}\right) \left[2(1-\sqrt{1-r^2}) - r^2\right]^{\frac{n}{2}}}{r^n\sqrt{1-r^2}}. \tag{A.4}$$

Since the first independent solution has a singularity at $r = 0$, ${C_1}^n = 0$, and ${C_2}^n$ is specified from Eqn. (3.21) as the boundary condition. For $n = 1$, the solution is

$$\xi_1 = C_1 \frac{r}{\sqrt{1-r^2}} + C_2 \left[\frac{r \ln\left(\frac{1+\sqrt{1-r^2}}{1-\sqrt{1-r^2}}\right)}{\sqrt{1-r^2}} + \frac{2}{r} \right]. \tag{A.5}$$

For the same reason as Eqn. (A.4), $C_2 = 0$, but there is no value of C_1 that satisfies Eqn. (3.21). For $n = 0$

$$\xi_0 = C_1 + \frac{k}{2\sqrt{1-r^2}} + C_2 \left[\frac{1}{2} \ln\left(\frac{1+\sqrt{1-r^2}}{1-\sqrt{1-r^2}} \right) - \frac{1}{\sqrt{1-r^2}} \right], \tag{A.6}$$

where, again, $C_2 = 0$, and C_1 is specified by Eqn. (3.21) as the boundary condition.

Appendix B

Solution in the neighbourhood of $r = 1$ in Chapter 3

First, I rewrite Eqns. (3.11) and (3.22) as

$$z = -\sqrt{1-r^2} + \epsilon \tfrac{F(r,\theta)}{\sqrt{1-r^2}} + \\ \epsilon \left[C_0 + \sum_{n=2}^{\infty} \left\{ \tfrac{\left(n+\sqrt{1-r^2}\right)\left(2(1-\sqrt{1-r^2})-r^2\right)^{\frac{n}{2}} - n}{r^n\sqrt{1-r^2}} \left[C_n \cos(n\theta) + D_n \sin(n\theta) \right] \right\} \right], \tag{B.1}$$

where $F(r, \theta)$ is defined in Eqn. (3.27). Obviously, the singularity at $r = 1$ appears only in the second term on the right-hand side. If $1 - r^2 = O(1)$, then

$$-\sqrt{1-r^2} + \epsilon \frac{F(r,\theta)}{\sqrt{1-r^2}} = -\sqrt{1-r^2-2\epsilon F(r,\theta)}. \tag{B.2}$$

When $1 - r^2 \ll 1$, higher order terms are required to equate each side of Eqn. (B.2), so

$$-\sqrt{1-r^2} + \epsilon \frac{F(r,\theta)}{\sqrt{1-r^2}} = -\sqrt{1-r^2+\epsilon\gamma_1(r,\theta)+\epsilon^2\gamma_2(r,\theta)}. \tag{B.3}$$

Here, the right-hand side is a new form for the solution, and is used in the interval $[1 - |\epsilon|, r_{max}]$. Equating the two sides of Eqn. (B.3) at $r = 1 - |\epsilon|$ gives

$$\gamma_1(r,\theta) = -2F + \frac{F^2}{2}\mathrm{sgn}(\epsilon), \quad \gamma_2(r,\theta) = \frac{F^2}{4}. \tag{B.4}$$

The remaining terms in Eqn. (B.1) also change in neighbourhood of $r = 1$. When $r = 1 - |\epsilon|$, a new $|\epsilon|^{\frac{1}{2}}$ order arises, so an $|\epsilon|^{\frac{1}{2}}$ order term is added to the solution in this neighbourhood,

$$
\begin{aligned}
|\epsilon|^{\frac{1}{2}}\gamma_3 + \epsilon\gamma_4 &= \epsilon \left\{ C_0 + \sum_{n=2}^{\infty} \left[\frac{\left[n+\sqrt{1-r^2}\right]\left(2(1-\sqrt{1-r^2})-r^2\right)^{\frac{1}{2}} - n}{r^n\sqrt{1-r^2}} \left[C_n \cos(n\theta) + D_n \sin(n\theta)\right] \right] \right\} \\
&= \epsilon \left\{ C_0 + \sum_{n=2}^{\infty} \left[\frac{\left(n+\sqrt{1-r^2}\right)\left(2-r^2\right)^{\frac{n}{2}}\left(1-\frac{n}{2-r^2}\sqrt{1-r^2}\right) - n}{r^n\sqrt{1-r^2}} \left[C_n \cos(n\theta) + D_n \sin(n\theta)\right] \right] \right\},
\end{aligned}
\tag{B.5}
$$

where higher orders of $\sqrt{1-r^2}$ are neglected. Finally,

$$
|\epsilon|^{\frac{1}{2}}\gamma_3 + \epsilon\gamma_4 = \epsilon \left\{ C_0 + \sum_{n=2}^{\infty} \left[\frac{\left(2-r^2\right)^{\frac{n}{2}-1}\left(2-r^2-n^2\right)}{r^n} \left[C_n \cos(n\theta) + D_n \sin(n\theta)\right] \right] \right\}, \tag{B.6}
$$

and, consequently,

$$
\gamma_3 = 0, \quad \gamma_4 = C_0 + \sum_{n=2}^{\infty} \left\{ \frac{\left(2-r^2\right)^{\frac{n}{2}-1}\left(2-r^2-n^2\right)}{r^n} \left[C_n \cos(n\theta) + D_n \sin(n\theta)\right] \right\}. \tag{B.7}
$$

Appendix C

Analysis of numerical and perturbation errors

Figure C.1 below shows the perturbed energy from Surface Evolver plotted as a function of the number of facets (left panel). I fitted these data to power-law relations of the form $\Delta E/(\gamma R_0^2) = \text{const.} + e_E$, where the error $e_E = \alpha N^\beta$. As shown in the right panel, the error decays with a power-law exponent $\alpha \approx -1$.

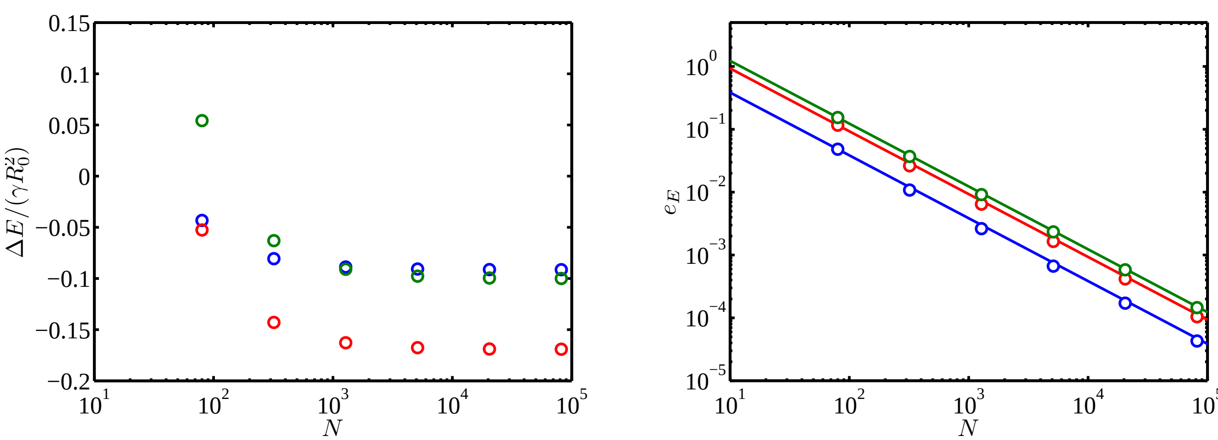

Figure C.1: Grid convergence test: (left) energy change versus number of facets for $\varepsilon = -0.2$ and 60° (blue), 90° (red), and 120° (green) contact angles. (right) Energy error when increasing number of facets for the same contact angles showing convergence order.

To establish the order of the error for the perturbation theory, I calculated difference between the perturbed pressure from the analytical approximation from values obtained from Surface Evolver, after extrapolating the computations (which converge as N^{-1}) to

$N = \infty$, as undertaken in Figure C.1 for the energy. This difference is plotted as a function of the perturbation parameter ϵ in Figure C.2, where it is demonstrated that it grows as ϵ^2.

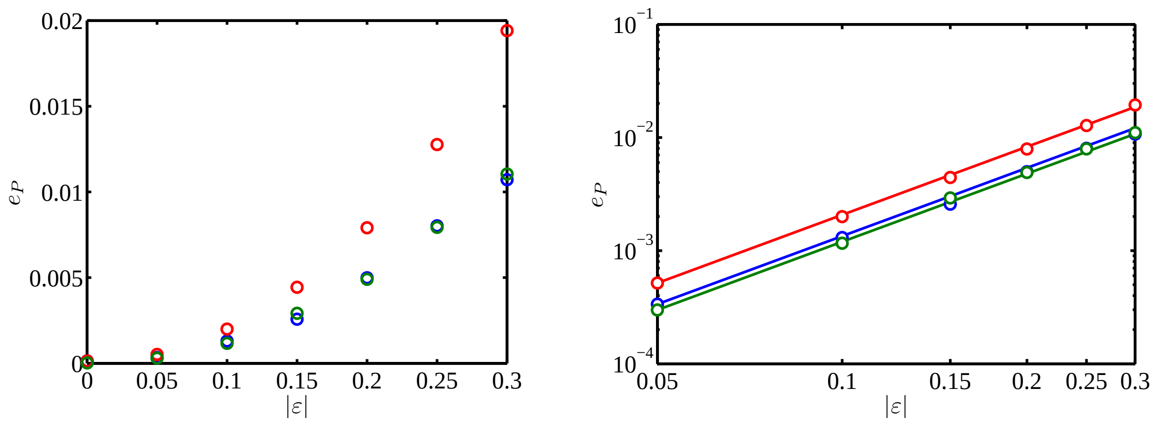

Figure C.2: (left) Pressure error versus ε for $\alpha = 50°$ (blue), $90°$ (red), $120°$ (green). (right) Pressure error order for the same contact angles.

Appendix D

Details of the experiments

As explained in Section 4.5, super soft latex tubes from McMaster Carr with 3/4″ outside diameter and 1/16″ wall thickness were filled with silicon oil and immersed in a water-methanol bath to verify the tube-buckling theory. The schemtaic of the setup is shown in Figure D.1. For the silicon-rubber tubes, I didn't use the water-methanol bath as the gravity impact was negligible.

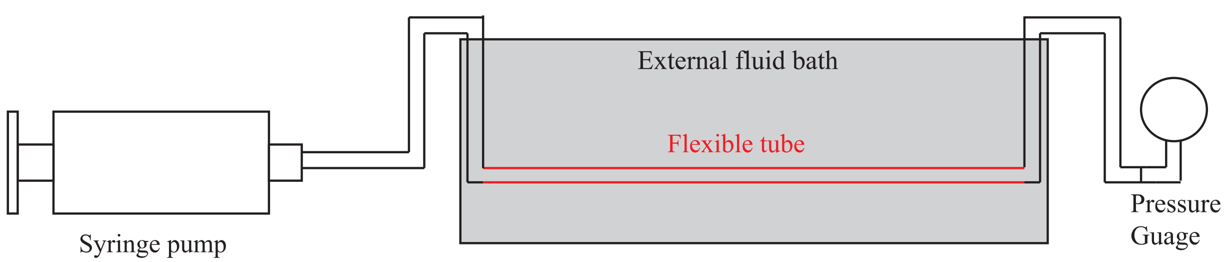

Figure D.1: Schematic of the experimental setup

D.1 Young's modulus measurement

To measure the elastic modulus of the silicon-rubber tube, I used a standard tension test with 0.5 mm min^{-1} elongation rate. A sample raw data of stress σ versus strain e, and the corresponding filtered data are shown in Figure D.2. I used a moving average filter of order 300, which takes the average of 300 surrounding data points. I calculated the slope of this curve when the strain $0.01 < e < 0.03$ to measure the Young's modulus. Here, σ is the force per unit tube-wall area, and e is the tube elongation with respect to its initial length (engineering strain).

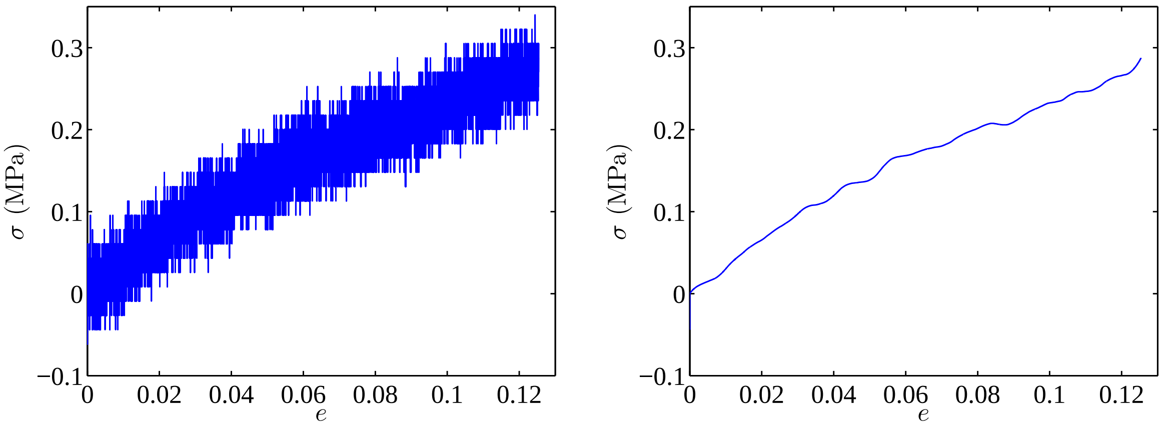

Figure D.2: Left: A sample raw data of stress versus strain. Right: Same data when filtered with a moving average filter

D.2 Contact angle measurement

I used a standard tensiometer to measure the contact angle. Sample pictures taken from a water or oil droplet on a flattened tube is shown in Figure D.3 and D.4.

Figure D.3: Three different measurements of contact angle of water on silicon-rubber tube.

D.3 Surface tension measurement

I used a Wilhelmy plate test to measure the oil surface tension. Table D.1 shows the results of several measurements.

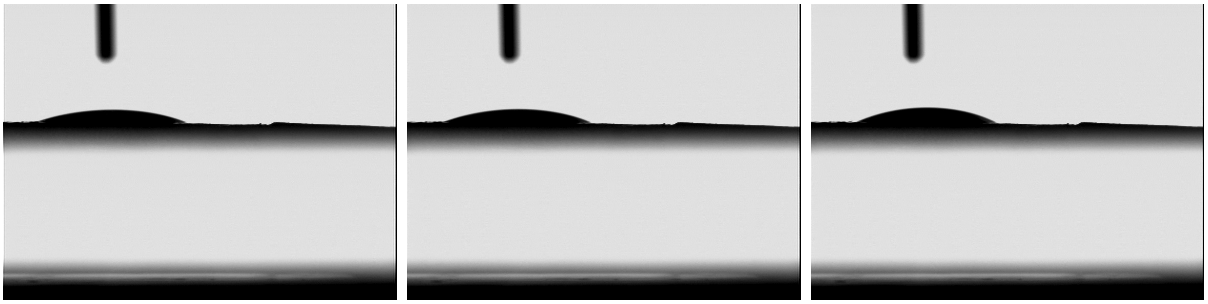

Figure D.4: Three different measurements of contact angle of oil on silicon-rubber tube.

Table D.1: Several measurements of oil surface tension with the Wilhelmy plate at 25°.

Test number	1	2	3	4
Measured surface tension (mN/m)	27.39	27.582	27.487	27.47

D.4 Hole size measurement

The hole diameter was measured using a microscope. Sample pictures from the holes are shown in Figure D.5

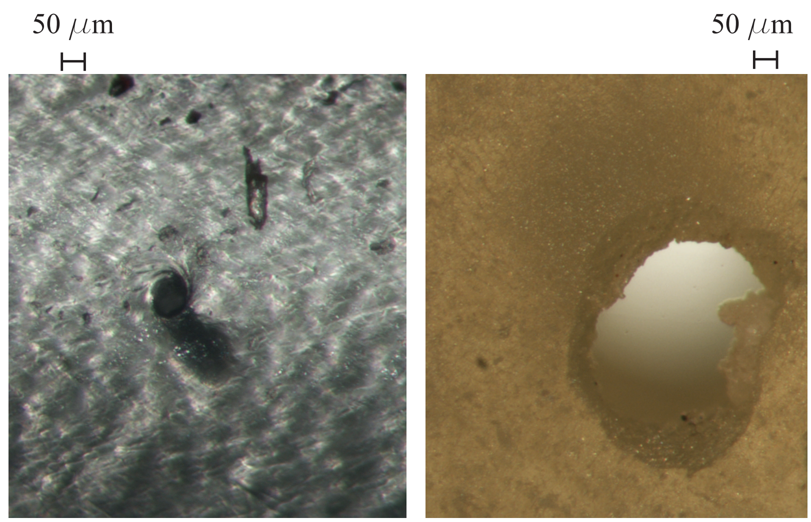

Silicone tube 2 mm diameter and 0.2 mm thickness.

Latex tube 19.5 mm diameter and 1.6 mm thickness.

Figure D.5: Two different holes drilled under liquid nitrogen using different drill bits.

Appendix E

Matlab code for Chapter 4

```
% This code calculates the critical elasto-capillary number at which the
% cicular tube will collapse under capillary pressure, when changing
% contact angle.

clc
clear

% Defining parameters
Rh=0.1; % Hole size
angle1=0; % Contact angle
Vbf=10^-3; % Maximum bubble volume
Vbs=Vbf/1000; % Minimum bubble volume
a=0.85; % Maximum liquid volume
b=1.;% Minimum liquid volume

[omega,A,B,I,Vtot,Pe_bu_f,Pc_bu_f,Pc_br_s,V_bu_f,Pem,Pcm,Vbm]=find_omega_c(angle1,Rh,a,b,Vbf,Vbs);
ii=1;

save Rh01_results
```

```
I2=b-a;
while angle1(ii)<180
     angle1(ii+1)=angle1(ii)+5;
    if ii<3
          a=Vtot(ii)-I2;
          b=Vtot(ii)+I2;
     else
          a=Vtot(ii)-2*abs(Vtot(ii)-Vtot(ii-2));
          b=Vtot(ii)+2*abs(Vtot(ii)-Vtot(ii-2));
     end

     Vbf=V_bu_f(ii);
     Vbs=Vbf/1000;
     [omega(ii+1),A(ii+1),B(ii+1),I(ii+1),Vtot(ii+1),Pe_bu_f(ii+1)
        ,Pc_bu_f(ii+1),Pc_br_s(ii+1),V_bu_f(ii+1),Pem(ii+1),Pcm(ii
        +1),Vbm(ii+1)]=find_omega_c(angle1(ii+1),Rh,a,b,Vbf,Vbs);
     ii=ii+1
     save Rh01_results
end

%
  %%%%%%%%%%%%%%%%%%%%%%%%%%%%%%%%%%%%%%%%%%%%%%%%%%%%%%%%%%%%%%%%%%%%%%%%%%%%%%%%%%%%%%%

function [omega,A,B,I,Vtot,Pe_bu_f,Pc_bu_f,Pc_br_s,V_bu_f,Pem,Pcm
    ,Vbm]=find_omega_c(angle1,Rh,a,b,Vbf,Vbs)
% This function calculates the critical elasto-capillary number

tol=min([Rh^5,10^-7]);

I=b-a;

Vtot=b; % Fixing liquid volume

```

```
% Calculating configuration with minimum bubble volume
Pe_bu_s=find_Vs(Vtot,Vbs,Rh);

% Calculating configuration when bubble touches the opposite wall
    .
[Pe_bu_f,Pc_bu_f,Pc_br_s,V_bu_f]=find_Vbm(Vtot,Vbs,Vbf,Rh,angle1,
    tol);
step=Pe_bu_s-Pe_bu_f;

% Calculating configuration when bridge becomes unstable by
    exceeding wetting angle.
[Pe_u,Pc_u,Vb_u]=find_unstable2(Pe_bu_f-step/10,Pe_bu_f-3*step,
    Vtot,Rh,angle1,step/2);
step2=Vb_u-V_bu_f;

% Calculating configuration with the maximum capillary pressure.
[Pem,Pcm,Vbm]=find_Pcmax2(V_bu_f+step2/10,Vb_u,Vtot,Rh,angle1,
    step2/10);
B=Pcm-Pc_bu_f-(Pem-Pe_bu_f)*Pc_bu_f/Pe_bu_f;

% Finding the root.

while B>0
     a=b;
     A=B;
     b=b+I/2;
     Vtot=b;
     Pe_bu_s=find_Vs(Vtot,Vbs,Rh);
     [Pe_bu_f,Pc_bu_f,Pc_br_s,V_bu_f]=find_Vbm(Vtot,Vbs,Vbf,Rh,
         angle1,tol);
     step=Pe_bu_s-Pe_bu_f;
     [Pe_u,Pc_u,Vb_u]=find_unstable2(Pe_bu_f-step/10,Pe_bu_f-3*
         step,Vtot,Rh,angle1,step/2);
     step2=Vb_u-V_bu_f;
```

```
    [Pem,Pcm,Vbm]=find_Pcmax2(V_bu_f+step2/10,Vb_u,Vtot,Rh,angle1
        ,step2/10);
    B=Pcm-Pc_bu_f-(Pem-Pe_bu_f)*Pc_bu_f/Pe_bu_f;
    I=b-a;
end

save midle1 b B V_bu_f Vb_u Vbm

Vbf=V_bu_f;

Vtot=a;
Pe_bu_s=find_Vs(Vtot,Vbs,Rh);
[Pe_bu_f,Pc_bu_f,Pc_br_s,V_bu_f]=find_Vbm(Vtot,Vbs,Vbf,Rh,angle1,
    tol);
step=Pe_bu_s-Pe_bu_f;
[Pe_u,Pc_u,Vb_u]=find_unstable2(Pe_bu_f-step/10,Pe_bu_f-3*step,
    Vtot,Rh,angle1,step/2);
step2=Vb_u-V_bu_f;
[Pem,Pcm,Vbm]=find_Pcmax2(V_bu_f+step2/10,Vb_u,Vtot,Rh,angle1,
    step2/10);
A=Pcm-Pc_bu_f-(Pem-Pe_bu_f)*Pc_bu_f/Pe_bu_f;

while A<0
    b=a;
    B=A;
    a=a-(a-0.8416)/4;
    Vtot=a;
    Pe_bu_s=find_Vs(Vtot,Vbs,Rh);
    [Pe_bu_f,Pc_bu_f,Pc_br_s,V_bu_f]=find_Vbm(Vtot,Vbs,Vbf,Rh,
        angle1,tol);
    step=Pe_bu_s-Pe_bu_f;
    [Pe_u,Pc_u,Vb_u]=find_unstable2(Pe_bu_f-step/10,Pe_bu_f-3*
        step,Vtot,Rh,angle1,step/2);
    step2=Vb_u-V_bu_f;
```

```
    [Pem,Pcm,Vbm]=find_Pcmax2(V_bu_f+step2/10,Vb_u,Vtot,Rh,angle1
        ,step2/10);
    A=Pcm-Pc_bu_f-(Pem-Pe_bu_f)*Pc_bu_f/Pe_bu_f;
end

save midle1 a A b B V_bu_f Vb_u Vbm


I=b-a;
while I>Rh*0.003
    c=a+I/2;
    Vtot=c;
    Pe_bu_s=find_Vs(Vtot,Vbs,Rh);
    [Pe_bu_f,Pc_bu_f,Pc_br_s,V_bu_f]=find_Vbm(Vtot,Vbs,Vbf,Rh,
        angle1,tol);
    step=Pe_bu_s-Pe_bu_f;
    [Pe_u,Pc_u,Vb_u]=find_unstable2(Pe_bu_f-step/10,Pe_bu_f-3*
        step,Vtot,Rh,angle1,step/2);
    step2=Vb_u-V_bu_f;
    [Pem,Pcm,Vbm]=find_Pcmax2(V_bu_f+step2/10,Vb_u,Vtot,Rh,angle1
        ,step2/10);
    C=Pcm-Pc_bu_f-(Pem-Pe_bu_f)*Pc_bu_f/Pe_bu_f;
    if A*C<0
        b=c;
        B=C;
    else
        a=c;
        A=C;
    end
    I=b-a;

    save midle1 c C a A b B V_bu_f Vb_u Vbm
end

```

```
omega=Pc_bu_f/Pe_bu_f;
%
%%%%%%%%%%%%%%%%%%%%%%%%%%%%%%%%%%%%%%%%%%%%%%%%%%%%%%%%%%%%%%%%%%%%%%%%%%%%%%


function [Pe]=find_Vs(Vtot,Vb,Rh)
% This function finds configuration with minimum bubble volume

At=(Vtot+Vb);

a=3.5;
b=5.398;
[LL,y_end,y_end2,ac,area,Energy]=tubeprofile(a,Rh);
A=area-At;
[LL,y_end,y_end2,ac,area,Energy]=tubeprofile(b,Rh);
B=area-At;
I=b-a;
while I>10^-12
    c=a+I/2;
    [LL,y_end,y_end2,ac,area,Energy]=tubeprofile(c,Rh);
    C=area-At;
    if A*C<0
        b=c;
        B=C;
    else
        a=c;
        A=C;
    end
    I=b-a;
end
Pe=c;
```

```
%
  %%%%%%%%%%%%%%%%%%%%%%%%%%%%%%%%%%%%%%%%%%%%%%%%%%%%%%%%%%%%%%%%%%%%%%%%%%%%%%%%

function [Pe,Pc1,Pc2,Vb]=find_Vbm(Vtot,Vbs,Vbf,Rh,angle1,tol)
% This function finds configuration when bubble touches the
    opposite wall.

b=Vbf;
Pe=find_Vs(Vtot,b,Rh);
[z0,alpha0]=write_bubble(angle1,Pe,Rh,b);
write_solve_bubble(Rh,z0);
[Pc2,energy,area,B]=solve_bubble(z0);
while B<0
     b=b*1.5;
     Pe=find_Vs(Vtot,b,Rh);
     [z0,alpha0]=write_bubble(angle1,Pe,Rh,b);
     write_solve_bubble(Rh,z0);
     [Pc2,energy,area,B]=solve_bubble(z0);
end

a=Vbs;
Pe=find_Vs(Vtot,b,Rh);
[z0,alpha0]=write_bubble(angle1,Pe,Rh,a);
write_solve_bubble(Rh,z0);
[Pc1,energy,area,A]=solve_bubble(z0);
while A>0
     a=a/2;
     Pe=find_Vs(Vtot,b,Rh);
     [z0,alpha0]=write_bubble(angle1,Pe,Rh,a);
     write_solve_bubble(Rh,z0);
     [Pc1,energy,area,A]=solve_bubble(z0);
end

```

```
if A*B>0
    'error'
    return
end


I=b-a;
while I>tol
    c=a+I/2;
    Pe=find_Vs(Vtot,c,Rh);
    [z0,alpha0]=write_bubble(angle1,Pe,Rh,c);
    write_solve_bubble(Rh,z0);
    [Pc,energy,area,C]=solve_bubble(z0);
    if A*C<0
        b=c;
        B=C;
        Pc2=Pc;
    else
        a=c;
        A=C;
        Pc1=Pc;
    end
    I=b-a;
end
Pe1=find_Vs(Vtot,c+c/20,Rh);
[z0,alpha0]=write_bridge(angle1,Pe1,Rh,c+c/20);
write_solve_bridge(Rh,z0);
[Pc2,energy,area,stability]=solve_bridge(alpha0,angle1,Rh);

Pc1=Pc;

Vb=c;
```

```
%
%%%%%%%%%%%%%%%%%%%%%%%%%%%%%%%%%%%%%%%%%%%%%%%%%%%%%%%%%%%%%%%%%%%%%%%%%%%%%

function [Pe,Pc,Vb]=find_Pcmax2(V1,V2,Vtot,Rh,angle1,tol)
% This finction finds configuration with the maximum capillary
    pressure when a liquid bridge is formed.

a=V1;
b=V2;

Pe2=find_Vs(Vtot,b,Rh);
[z0,alpha0]=write_bridge(angle1,Pe2,Rh,b);
write_solve_bridge(Rh,z0);
[B,energy,area,stb]=solve_bridge2(alpha0,angle1,Rh);

Pe1=find_Vs(Vtot,a,Rh);
[z0,alpha0]=write_bridge(angle1,Pe1,Rh,a);
write_solve_bridge(Rh,z0);
[A,energy,area,stb]=solve_bridge2(alpha0,angle1,Rh);


I=b-a;
while I>tol
     m1=a+I/3;
     m2=b-I/3;

     Pem1=find_Vs(Vtot,m1,Rh);
     [z0,alpha0]=write_bridge(angle1,Pem1,Rh,m1);
     write_solve_bridge(Rh,z0);
     [M1,energy,area,stb]=solve_bridge2(alpha0,angle1,Rh);

     Pem2=find_Vs(Vtot,m2,Rh);
```

```
    [z0,alpha0]=write_bridge(angle1,Pem2,Rh,m2);
    write_solve_bridge(Rh,z0);
    [M2,energy,area,stb]=solve_bridge2(alpha0,angle1,Rh);

    Pcm=[A M1 M2 B];
    Vm=[a m1 m2 b];
    Pem=[Pe1 Pem1 Pem2 Pe2];
    [max1,imax]=max(Pcm);
    if imax==1
        b=Vm(imax+2);
        B=Pcm(imax+2);
        Pe2=Pem(imax+2);
    elseif imax==4
        a=Vm(imax-2);
        A=Pcm(imax-2);
        Pe1=Pem(imax-2);
    else
        b=Vm(imax+1);
        B=Pcm(imax+1);
        a=Vm(imax-1);
        A=Pcm(imax-1);
        Pe1=Pem(imax-1);
        Pe2=Pem(imax+1);
    end

    I=b-a;
end
Vb=Vm(imax);
Pc=max1;
Pe=Pem(imax);
%
  %%%%%%%%%%%%%%%%%%%%%%%%%%%%%%%%%%%%%%%%%%%%%%%%%%%%%%%%%%%%%%%%%%%%%%%%%%%%%%%%%%%%%%%%%%%%%%%%%%%%%%%%%%%%%%%%%%%%%%%%%%%%%%%%%%%%%%%%%%%%%%
```

```
function [Pem,Pcm,Vbm]=find_unstable2(Pe1,Pe2,Vtot,Rh,L,angle1,
    tol)
% This function finds configuration when bridge becomes unstable
    by exceeding wetting angle1.

a=Pe2;
[LL,y_end,y_end2,a1,Area,Energy,alpha0]=tubeprofile(a,Rh);
Vb=Area*L-Vtot;
[z0,alpha0]=write_bridge(angle1,a,Rh,Vb);
write_solve_bridge(Rh,z0);
[Pc,energy,area,A]=solve_bridge2(alpha0,angle1,Rh);


b=Pe1;
[LL y_end y_end2 a1 Area Energy,alpha0]=tubeprofile(b,Rh);
Vb=Area*L-Vtot;
[z0,alpha0]=write_bridge(angle1,b,Rh,Vb);
write_solve_bridge(Rh,z0);
[Pc,energy,area,B]=solve_bridge2(alpha0,angle1,Rh);


I=(b-a);
while I>tol
    c=a+I/2;
    [LL y_end y_end2 a1 Area Energy,alpha0]=tubeprofile(c,Rh);
    Vb=Area*L-Vtot;
    [z0,alpha0]=write_bridge(angle1,c,Rh,Vb);
    write_solve_bridge(Rh,z0);
    [Pc,energy,area,C]=solve_bridge2(alpha0,angle1,Rh);
    if A*C<0
        b=c;
        B=C;
    else
        a=c;
```

```
            A=C;
        end
        I=b-a;
end
Pem=c;
Pcm=Pc;
Vbm=Vb;
% %%%%%%%%%%%%%%%%%%%%%%%%%%%%%%%%%%%%%%%%%%%%%%%%%%%%%%%%%%%%%%%%%%%%%%%%%%%%%%%%%%%%%%%%%%%%


function [z0,alpha0]=write_bridge(angle1,Pe,Rh,V)
% This function writes initial conditio of a bridge for Surface Evolver

[r0,z0,z02,a,area_t,ene,alpha0]=tubeprofile(Pe,Rh);
nn=[1 2 3 4];
an=[nn; a];


T=-cos(angle1*pi/180);
rr=Rh;

theta=0:pi/8:pi;
xx=Rh*cos(theta);
zzz=((a(1)*(r0^2-xx.^2).^2+a(2)*(r0^2-xx.^2).^1.5+a(3)*(r0^2-xx.^2)+a(4)*(r0^2-xx.^2).^0.5));

fid = fopen('bridge.fe', 'w');
fprintf(fid, '// Evolver data for a bubble of prescribed volume between the opposite walls of a\n');
fprintf(fid, '//collapsed tube without gravity.\n');

```

```
fprintf(fid, 'SPRING_CONSTANT 1 // for most accurate gap areas for constraint 1\n');
fprintf(fid, 'SYMMETRIC_CONTENT     // for volume calculations\n');

fprintf(fid, 'PARAMETER angle := %6.2f // interior angle between plane and surface, degrees\n', angle1);
fprintf(fid, 'PARAMETER r0 := %8.7f /* distance from center at y=0 */\n', r0);
fprintf(fid, 'PARAMETER Rh := %7.6f // Hole radius\n', Rh);
fprintf(fid, 'PARAMETER z0 := %8.7f // end height\n',z0);
fprintf(fid, 'PARAMETER Vol = %8.7f  //volume\n',V);
fprintf(fid, 'PARAMETER ten = %8.7f  //tension\n',T);
fprintf(fid, 'PARAMETER a%d = %8.7f\n',an);
fprintf(fid, 'PARAMETER rr = %8.7f\n',rr);


fprintf(fid, 'constraint 1 CONVEX // hole\n');
fprintf(fid, 'function: x^2 + y^2 = Rh^2\n');

fprintf(fid, 'constraint 2 CONVEX // hole\n');
fprintf(fid, 'function z=-((a1*(r0^2-x^2)^2+a2*(r0^2-x^2)^1.5+a3*(r0^2-x^2)+a4*(r0^2-x^2)^0.5))\n');

fprintf(fid, 'constraint 3 CONVEX // wall\n');
fprintf(fid, 'function z=((a1*(r0^2-x^2)^2+a2*(r0^2-x^2)^1.5+a3*(r0^2-x^2)+a4*(r0^2-x^2)^0.5))\n');


fprintf(fid, 'vertices\n');
fprintf(fid, '1 rr*cos(pi) rr*sin(pi) %8.7f  constraint 3\n',zzz(9));
fprintf(fid, '2 rr*cos(7*pi/8) rr*sin(7*pi/8) %8.7f  constraint 3\n',zzz(8));
```

```
fprintf(fid, '3 rr*cos(6*pi/8) rr*sin(6*pi/8) %8.7f  constraint 3\n',zzz(7));
fprintf(fid, '4 rr*cos(5*pi/8) rr*sin(5*pi/8) %8.7f  constraint 3\n',zzz(6));
fprintf(fid, '5 rr*cos(4*pi/8) rr*sin(4*pi/8) %8.7f  constraint 3\n',zzz(5));
fprintf(fid, '6 rr*cos(3*pi/8) rr*sin(3*pi/8) %8.7f  constraint 3\n',zzz(4));
fprintf(fid, '7 rr*cos(2*pi/8) rr*sin(2*pi/8) %8.7f  constraint 3\n',zzz(3));
fprintf(fid, '8 rr*cos(pi/8) rr*sin(pi/8) %8.7f  constraint 3\n',zzz(2));
fprintf(fid, '9 rr*cos(0) rr*sin(0) %8.7f  constraint 3\n',zzz(1));
fprintf(fid, '10 rr*cos(-pi/8) rr*sin(-pi/8) %8.7f  constraint 3\n',zzz(2));
fprintf(fid, '11 rr*cos(-2*pi/8) rr*sin(-2*pi/8) %8.7f constraint 3\n',zzz(3));
fprintf(fid, '12 rr*cos(-3*pi/8) rr*sin(-3*pi/8) %8.7f constraint 3\n',zzz(4));
fprintf(fid, '13 rr*cos(-4*pi/8) rr*sin(-4*pi/8) %8.7f constraint 3\n',zzz(5));
fprintf(fid, '14 rr*cos(-5*pi/8) rr*sin(-5*pi/8) %8.7f constraint 3\n',zzz(6));
fprintf(fid, '15 rr*cos(-6*pi/8) rr*sin(-6*pi/8) %8.7f constraint 3\n',zzz(7));
fprintf(fid, '16 rr*cos(-7*pi/8) rr*sin(-7*pi/8) %8.7f constraint 3\n',zzz(8));
fprintf(fid, '17 rr*cos(pi) rr*sin(pi) -%8.7f constraint 1,2\n',zzz(9));
fprintf(fid, '18 rr*cos(7*pi/8) rr*sin(7*pi/8) -%8.7f constraint 1,2\n',zzz(8));
fprintf(fid, '19 rr*cos(6*pi/8) rr*sin(6*pi/8) -%8.7f constraint 1,2\n',zzz(7));
```

```
fprintf(fid, '20 rr*cos(5*pi/8) rr*sin(5*pi/8) -%8.7f constraint
    1,2\n',zzz(6));
fprintf(fid, '21 rr*cos(4*pi/8) rr*sin(4*pi/8) -%8.7f constraint
    1,2\n',zzz(5));
fprintf(fid, '22 rr*cos(3*pi/8) rr*sin(3*pi/8) -%8.7f constraint
    1,2\n',zzz(4));
fprintf(fid, '23 rr*cos(2*pi/8) rr*sin(2*pi/8) -%8.7f constraint
    1,2\n',zzz(3));
fprintf(fid, '24 rr*cos(pi/8) rr*sin(pi/8) -%8.7f constraint 1,2\
    n',zzz(2));
fprintf(fid, '25 rr*cos(0) rr*sin(0) -%8.7f constraint 1,2\n',zzz
    (1));
fprintf(fid, '26 rr*cos(-pi/8) rr*sin(-pi/8) -%8.7f constraint
    1,2\n',zzz(2));
fprintf(fid, '27 rr*cos(-2*pi/8) rr*sin(-2*pi/8) -%8.7f
    constraint 1,2\n',zzz(3));
fprintf(fid, '28 rr*cos(-3*pi/8) rr*sin(-3*pi/8) -%8.7f
    constraint 1,2\n',zzz(4));
fprintf(fid, '29 rr*cos(-4*pi/8) rr*sin(-4*pi/8) -%8.7f
    constraint 1,2\n',zzz(5));
fprintf(fid, '30 rr*cos(-5*pi/8) rr*sin(-5*pi/8) -%8.7f
    constraint 1,2\n',zzz(6));
fprintf(fid, '31 rr*cos(-6*pi/8) rr*sin(-6*pi/8) -%8.7f
    constraint 1,2\n',zzz(7));
fprintf(fid, '32 rr*cos(-7*pi/8) rr*sin(-7*pi/8) -%8.7f
    constraint 1,2\n',zzz(8));

fprintf(fid, 'edges /* given by endpoints and attribute */\n');
fprintf(fid, '1 1 2 constraint 3\n');
fprintf(fid, '2 2 3 constraint 3\n');
fprintf(fid, '3 3 4 constraint 3\n');
fprintf(fid, '4 4 5 constraint 3\n');
fprintf(fid, '5 5 6 constraint 3\n');
fprintf(fid, '6 6 7 constraint 3\n');
```

```
fprintf(fid, '7 7 8 constraint 3\n');
fprintf(fid, '8 8 9 constraint 3\n');
fprintf(fid, '9 9 10 constraint 3\n');
fprintf(fid, '10 10 11 constraint 3\n');
fprintf(fid, '11 11 12 constraint 3\n');
fprintf(fid, '12 12 13 constraint 3\n');
fprintf(fid, '13 13 14 constraint 3\n');
fprintf(fid, '14 14 15 constraint 3\n');
fprintf(fid, '15 15 16 constraint 3\n');
fprintf(fid, '16 16 1 constraint 3\n');
fprintf(fid, '17 17 18 constraint 1,2\n');
fprintf(fid, '18 18 19 constraint 1,2\n');
fprintf(fid, '19 19 20 constraint 1,2\n');
fprintf(fid, '20 20 21 constraint 1,2\n');
fprintf(fid, '21 21 22 constraint 1,2\n');
fprintf(fid, '22 22 23 constraint 1,2\n');
fprintf(fid, '23 23 24 constraint 1,2\n');
fprintf(fid, '24 24 25 constraint 1,2\n');
fprintf(fid, '25 25 26 constraint 1,2\n');
fprintf(fid, '26 26 27 constraint 1,2\n');
fprintf(fid, '27 27 28 constraint 1,2\n');
fprintf(fid, '28 28 29 constraint 1,2\n');
fprintf(fid, '29 29 30 constraint 1,2\n');
fprintf(fid, '30 30 31 constraint 1,2\n');
fprintf(fid, '31 31 32 constraint 1,2\n');
fprintf(fid, '32 32 17 constraint 1,2\n');
fprintf(fid, '33 1 17\n');
fprintf(fid, '34 2 18\n');
fprintf(fid, '35 3 19\n');
fprintf(fid, '36 4 20\n');
fprintf(fid, '37 5 21\n');
fprintf(fid, '38 6 22\n');
fprintf(fid, '39 7 23\n');
fprintf(fid, '40 8 24\n');
```

```
fprintf(fid, '41 9 25\n');
fprintf(fid, '42 10 26\n');
fprintf(fid, '43 11 27\n');
fprintf(fid, '44 12 28\n');
fprintf(fid, '45 13 29\n');
fprintf(fid, '46 14 30\n');
fprintf(fid, '47 15 31\n');
fprintf(fid, '48 16 32\n');

fprintf(fid, 'faces /* given by oriented edge loop */\n');
fprintf(fid, '1 -1 -16 -15 -14 -13 -12 -11 -10 -9 -8 -7 -6 -5 -4
    -3 -2 tension ten constraint 3\n');
fprintf(fid, '2 1 34 -17 -33\n');
fprintf(fid, '3 2 35 -18 -34 \n');
fprintf(fid, '4 3 36 -19 -35\n');
fprintf(fid, '5 4 37 -20 -36\n');
fprintf(fid, '6 5 38 -21 -37\n');
fprintf(fid, '7 6 39 -22 -38\n');
fprintf(fid, '8 7 40 -23 -39\n');
fprintf(fid, '9 8 41 -24 -40\n');
fprintf(fid, '10 9 42 -25 -41\n');
fprintf(fid, '11 10 43 -26 -42\n');
fprintf(fid, '12 11 44 -27 -43\n');
fprintf(fid, '13 12 45 -28 -44\n');
fprintf(fid, '14 13 46 -29 -45\n');
fprintf(fid, '15 14 47 -30 -46\n');
fprintf(fid, '16 15 48 -31 -47\n');
fprintf(fid, '17 16 33 -32 -48\n');
fprintf(fid, '18 17 18 19 20 21 22 23 24 25 26 27 28 29 30 31 32
    tension 0 constraint 2 //fixed\n');

fprintf(fid, 'bodies /* one body, defined by its oriented faces
    */\n');
```

```
fprintf(fid, '1 1 2 3 4 5 6 7 8 9 10 11 12 13 14 15 16 17 18 volume Vol density 0\n');

fclose(fid);

%
%%%%%%%%%%%%%%%%%%%%%%%%%%%%%%%%%%%%%%%%%%%%%%%%%%%%%%%%%%%%%%%%%%%%%%%%%%%%%%%%%%%%%%%%

function [z0,alpha0]=write_bubble(angle1,Pe,Rh,V)
% This function writes initial conditio of a bubble for Surface Evolver

[r0,z0,z02,a,area_t,alpha0]=tubeprofile(Pe,Rh);
nn=[1 2 3 4];
an=[nn; a];


T=-cos(angle1*pi/180);
rr=Rh/2;

theta=0:pi/8:pi;
xx=Rh*cos(theta);
zzz=((a(1)*(r0^2-xx.^2).^2+a(2)*(r0^2-xx.^2).^1.5+a(3)*(r0^2-xx.^2)+a(4)*(r0^2-xx.^2).^0.5));

if V<Rh^3/10
    zt=-zzz(9)/2;
elseif V<Rh^3
    zt=0;
else
    zt=zzz(9)/2;
end

```

```
fid = fopen('bubble.fe', 'w');
fprintf(fid, '// Evolver data for a bubble of prescribed volume between the opposite walls of a\n');
fprintf(fid, '//collapsed tube without gravity.\n');

fprintf(fid, 'SPRING_CONSTANT 1 // for most accurate gap areas for constraint 1\n');
fprintf(fid, 'SYMMETRIC_CONTENT     // for volume calculations\n');

fprintf(fid, 'PARAMETER angle := %6.2f // interior angle between plane and surface, degrees\n', angle1);
fprintf(fid, 'PARAMETER r0 := %8.7f /* distance from center at y=0 */\n', r0);
fprintf(fid, 'PARAMETER Rh := %7.6f // Hole radius\n', Rh);
fprintf(fid, 'PARAMETER z0 := %8.7f // end height\n',z0);
fprintf(fid, 'PARAMETER Vol = %8.7f  //volume\n',V);
fprintf(fid, 'PARAMETER a%d = %8.7f\n',an);
fprintf(fid, 'PARAMETER rr = %8.7f\n',rr);


fprintf(fid, 'constraint 1 CONVEX // hole\n');
fprintf(fid, 'function: x^2 + y^2 = Rh^2\n');

fprintf(fid, 'constraint 2 CONVEX // hole\n');
fprintf(fid, 'function z=-((a1*(r0^2-x^2)^2+a2*(r0^2-x^2)^1.5+a3*(r0^2-x^2)+a4*(r0^2-x^2)^0.5))\n');


fprintf(fid, 'vertices\n');
fprintf(fid, '1 rr*cos(pi) rr*sin(pi) %8.7f   \n',zt);
fprintf(fid, '2 rr*cos(7*pi/8) rr*sin(7*pi/8) %8.7f   \n',zt);
fprintf(fid, '3 rr*cos(6*pi/8) rr*sin(6*pi/8) %8.7f   \n',zt);
```

```
fprintf(fid, '4 rr*cos(5*pi/8) rr*sin(5*pi/8) %8.7f   \n',zt);
fprintf(fid, '5 rr*cos(4*pi/8) rr*sin(4*pi/8) %8.7f   \n',zt);
fprintf(fid, '6 rr*cos(3*pi/8) rr*sin(3*pi/8) %8.7f   \n',zt);
fprintf(fid, '7 rr*cos(2*pi/8) rr*sin(2*pi/8) %8.7f   \n',zt);
fprintf(fid, '8 rr*cos(pi/8) rr*sin(pi/8) %8.7f   \n',zt);
fprintf(fid, '9 rr*cos(0) rr*sin(0) %8.7f   \n',zt);
fprintf(fid, '10 rr*cos(-pi/8) rr*sin(-pi/8) %8.7f   \n',zt);
fprintf(fid, '11 rr*cos(-2*pi/8) rr*sin(-2*pi/8) %8.7f   \n',zt);
fprintf(fid, '12 rr*cos(-3*pi/8) rr*sin(-3*pi/8) %8.7f   \n',zt);
fprintf(fid, '13 rr*cos(-4*pi/8) rr*sin(-4*pi/8) %8.7f   \n',zt);
fprintf(fid, '14 rr*cos(-5*pi/8) rr*sin(-5*pi/8) %8.7f   \n',zt);
fprintf(fid, '15 rr*cos(-6*pi/8) rr*sin(-6*pi/8) %8.7f   \n',zt);
fprintf(fid, '16 rr*cos(-7*pi/8) rr*sin(-7*pi/8) %8.7f   \n',zt);
fprintf(fid, '17 Rh*cos(pi) Rh*sin(pi) -%8.7f constraint 1,2\n',zzz(9));
fprintf(fid, '18 Rh*cos(7*pi/8) Rh*sin(7*pi/8) -%8.7f constraint 1,2\n',zzz(8));
fprintf(fid, '19 Rh*cos(6*pi/8) Rh*sin(6*pi/8) -%8.7f constraint 1,2\n',zzz(7));
fprintf(fid, '20 Rh*cos(5*pi/8) Rh*sin(5*pi/8) -%8.7f constraint 1,2\n',zzz(6));
fprintf(fid, '21 Rh*cos(4*pi/8) Rh*sin(4*pi/8) -%8.7f constraint 1,2\n',zzz(5));
fprintf(fid, '22 Rh*cos(3*pi/8) Rh*sin(3*pi/8) -%8.7f constraint 1,2\n',zzz(4));
fprintf(fid, '23 Rh*cos(2*pi/8) Rh*sin(2*pi/8) -%8.7f constraint 1,2\n',zzz(3));
fprintf(fid, '24 Rh*cos(pi/8) Rh*sin(pi/8) -%8.7f constraint 1,2\n',zzz(2));
fprintf(fid, '25 Rh*cos(0) Rh*sin(0) -%8.7f constraint 1,2\n',zzz(1));
fprintf(fid, '26 Rh*cos(-pi/8) Rh*sin(-pi/8) -%8.7f constraint 1,2\n',zzz(2));
```

```
fprintf(fid, '27 Rh*cos(-2*pi/8) Rh*sin(-2*pi/8) -%8.7f
    constraint 1,2\n',zzz(3));
fprintf(fid, '28 Rh*cos(-3*pi/8) Rh*sin(-3*pi/8) -%8.7f
    constraint 1,2\n',zzz(4));
fprintf(fid, '29 Rh*cos(-4*pi/8) Rh*sin(-4*pi/8) -%8.7f
    constraint 1,2\n',zzz(5));
fprintf(fid, '30 Rh*cos(-5*pi/8) Rh*sin(-5*pi/8) -%8.7f
    constraint 1,2\n',zzz(6));
fprintf(fid, '31 Rh*cos(-6*pi/8) Rh*sin(-6*pi/8) -%8.7f
    constraint 1,2\n',zzz(7));
fprintf(fid, '32 Rh*cos(-7*pi/8) Rh*sin(-7*pi/8) -%8.7f
    constraint 1,2\n',zzz(8));

fprintf(fid, 'edges /* given by endpoints and attribute */\n');
fprintf(fid, '1 1 2  \n');
fprintf(fid, '2 2 3  \n');
fprintf(fid, '3 3 4  \n');
fprintf(fid, '4 4 5  \n');
fprintf(fid, '5 5 6  \n');
fprintf(fid, '6 6 7  \n');
fprintf(fid, '7 7 8  \n');
fprintf(fid, '8 8 9  \n');
fprintf(fid, '9 9 10  \n');
fprintf(fid, '10 10 11  \n');
fprintf(fid, '11 11 12  \n');
fprintf(fid, '12 12 13  \n');
fprintf(fid, '13 13 14  \n');
fprintf(fid, '14 14 15  \n');
fprintf(fid, '15 15 16  \n');
fprintf(fid, '16 16 1  \n');
fprintf(fid, '17 17 18 constraint 1,2\n');
fprintf(fid, '18 18 19 constraint 1,2\n');
fprintf(fid, '19 19 20 constraint 1,2\n');
fprintf(fid, '20 20 21 constraint 1,2\n');
```

```
fprintf(fid, '21 21 22 constraint 1,2\n');
fprintf(fid, '22 22 23 constraint 1,2\n');
fprintf(fid, '23 23 24 constraint 1,2\n');
fprintf(fid, '24 24 25 constraint 1,2\n');
fprintf(fid, '25 25 26 constraint 1,2\n');
fprintf(fid, '26 26 27 constraint 1,2\n');
fprintf(fid, '27 27 28 constraint 1,2\n');
fprintf(fid, '28 28 29 constraint 1,2\n');
fprintf(fid, '29 29 30 constraint 1,2\n');
fprintf(fid, '30 30 31 constraint 1,2\n');
fprintf(fid, '31 31 32 constraint 1,2\n');
fprintf(fid, '32 32 17 constraint 1,2\n');
fprintf(fid, '33 1 17\n');
fprintf(fid, '34 2 18\n');
fprintf(fid, '35 3 19\n');
fprintf(fid, '36 4 20\n');
fprintf(fid, '37 5 21\n');
fprintf(fid, '38 6 22\n');
fprintf(fid, '39 7 23\n');
fprintf(fid, '40 8 24\n');
fprintf(fid, '41 9 25\n');
fprintf(fid, '42 10 26\n');
fprintf(fid, '43 11 27\n');
fprintf(fid, '44 12 28\n');
fprintf(fid, '45 13 29\n');
fprintf(fid, '46 14 30\n');
fprintf(fid, '47 15 31\n');
fprintf(fid, '48 16 32\n');

fprintf(fid, 'faces /* given by oriented edge loop */\n');
fprintf(fid, '1 -1 -16 -15 -14 -13 -12 -11 -10 -9 -8 -7 -6 -5 -4
    -3 -2\n');
fprintf(fid, '2 1 34 -17 -33\n');
fprintf(fid, '3 2 35 -18 -34 \n');
```

```
fprintf(fid, '4 3 36 -19 -35\n');
fprintf(fid, '5 4 37 -20 -36\n');
fprintf(fid, '6 5 38 -21 -37\n');
fprintf(fid, '7 6 39 -22 -38\n');
fprintf(fid, '8 7 40 -23 -39\n');
fprintf(fid, '9 8 41 -24 -40\n');
fprintf(fid, '10 9 42 -25 -41\n');
fprintf(fid, '11 10 43 -26 -42\n');
fprintf(fid, '12 11 44 -27 -43\n');
fprintf(fid, '13 12 45 -28 -44\n');
fprintf(fid, '14 13 46 -29 -45\n');
fprintf(fid, '15 14 47 -30 -46\n');
fprintf(fid, '16 15 48 -31 -47\n');
fprintf(fid, '17 16 33 -32 -48\n');
fprintf(fid, '18 17 18 19 20 21 22 23 24 25 26 27 28 29 30 31 32
    tension 0 constraint 2 //fixed\n');

fprintf(fid, 'bodies /* one body, defined by its oriented faces
    */\n');
fprintf(fid, '1 1 2 3 4 5 6 7 8 9 10 11 12 13 14 15 16 17 18
    volume Vol density 0\n');

fclose(fid);
%
    %%%%%%%%%%%%%%%%%%%%%%%%%%%%%%%%%%%%%%%%%%%%%%%%%%%%%%%%%%%%%%%%%%%%%%%%%%%%%%%

function []=write_solve_bridge(Rh,zz)
% This finction writes the solution procedure for Surface Evolver
     when the
% interface is a bridge.

fid = fopen('solve_proc.txt', 'w');
fprintf(fid, 'bridge.fe\n');
fprintf(fid, 'r\n');
```

```
fprintf(fid, 'g10\n');
fprintf(fid, 'u\n');
fprintf(fid, 'g10\n');
fprintf(fid, 'u\n');
fprintf(fid, 't\n');
fprintf(fid, '%8.7f\n',Rh/10);
fprintf(fid, 'g10\n');
fprintf(fid, 'u\n');

fprintf(fid, 'r\n');
fprintf(fid, 't\n');
fprintf(fid, '%8.7f\n',Rh/10);
fprintf(fid, 'u\n');
fprintf(fid, 'g10\n');
fprintf(fid, 't\n');
fprintf(fid, '%8.7f\n',Rh/10);
fprintf(fid, 'u\n');
fprintf(fid, 'g10\n');
fprintf(fid, 'u\n');

fprintf(fid, 'r\n');
fprintf(fid, 'g20\n');
fprintf(fid, 't\n');
fprintf(fid, '%8.7f\n',Rh/10);
fprintf(fid, 'u\n');
fprintf(fid, 'g20\n');
fprintf(fid, 't\n');
fprintf(fid, '%8.7f\n',Rh/10);
fprintf(fid, 'u\n');

fprintf(fid, 'U\n');
fprintf(fid, 'g20\n');
fprintf(fid, 't\n');
fprintf(fid, '%8.7f\n',Rh/10);
```

```
fprintf(fid, 'u\n');
fprintf(fid, 'g20\n');
fprintf(fid, 't\n');
fprintf(fid, '%8.7f\n',Rh/10);
fprintf(fid, 'u\n');

tol=min(abs(zz),abs(Rh/30));

fprintf(fid, 'r\n');
fprintf(fid, 'g20\n');
fprintf(fid, 't\n');
fprintf(fid, '%8.7f\n',tol);
fprintf(fid, 'u\n');
fprintf(fid, 'g20\n');
fprintf(fid, 't\n');
fprintf(fid, '%8.7f\n',tol);
fprintf(fid, 'u\n');

fprintf(fid, 'r\n');
fprintf(fid, 'g20\n');
fprintf(fid, 't\n');
fprintf(fid, '%8.7f\n',tol);
fprintf(fid, 'u\n');
fprintf(fid, 'g20\n');
fprintf(fid, 't\n');
fprintf(fid, '%8.7f\n',tol);
fprintf(fid, 'u\n');

fprintf(fid, 'd\n');
fprintf(fid, 'f1.fe\n');

fclose(fid);
%
    %%%%%%%%%%%%%%%%%%%%%%%%%%%%%%%%%%%%%%%%%%%%%%%%%%%%%%%%%%%%%%%%%%%%%%%%%%%%%
```

```
function []=write_solve_bubble(Rh,zz)
% This finction writes the solution procedure for Surface Evolver
    when the
% interface is a bubble.

fid = fopen('solve_proc.txt', 'w');
fprintf(fid, 'bubble.fe\n');
fprintf(fid, 'r\n');
fprintf(fid, 'g10\n');
fprintf(fid, 'u\n');
fprintf(fid, 'g10\n');
fprintf(fid, 'u\n');
fprintf(fid, 't\n');
fprintf(fid, '%8.7f\n',Rh/8);
fprintf(fid, 'g10\n');
fprintf(fid, 'u\n');
fprintf(fid, 't\n');
fprintf(fid, '%8.7f\n',Rh/8);
fprintf(fid, 'g10\n');
fprintf(fid, 'u\n');

fprintf(fid, 'r\n');
fprintf(fid, 't\n');
fprintf(fid, '%8.7f\n',Rh/10);
fprintf(fid, 'u\n');
fprintf(fid, 'g10\n');
fprintf(fid, 't\n');
fprintf(fid, '%8.7f\n',Rh/10);
fprintf(fid, 'u\n');
fprintf(fid, 'g10\n');
fprintf(fid, 'u\n');

fprintf(fid, 'r\n');
```

```
fprintf(fid, 'g20\n');
fprintf(fid, 't\n');
fprintf(fid, '%8.7f\n',Rh/10);
fprintf(fid, 'u\n');
fprintf(fid, 'g20\n');
fprintf(fid, 't\n');
fprintf(fid, '%8.7f\n',Rh/10);
fprintf(fid, 'u\n');

fprintf(fid, 'U\n');
fprintf(fid, 'g20\n');
fprintf(fid, 't\n');
fprintf(fid, '%8.7f\n',Rh/10);
fprintf(fid, 'u\n');
fprintf(fid, 'g20\n');
fprintf(fid, 't\n');
fprintf(fid, '%8.7f\n',Rh/10);
fprintf(fid, 'u\n');

tol=min(abs(zz),abs(Rh/30));

fprintf(fid, 'r\n');
fprintf(fid, 'g20\n');
fprintf(fid, 't\n');
fprintf(fid, '%8.7f\n',tol);
fprintf(fid, 'u\n');
fprintf(fid, 'g20\n');
fprintf(fid, 't\n');
fprintf(fid, '%8.7f\n',tol);
fprintf(fid, 'u\n');

fprintf(fid, 'r\n');
fprintf(fid, 'g20\n');
fprintf(fid, 't\n');
```

```
fprintf(fid, '%8.7f\n',tol);
fprintf(fid, 'u\n');
fprintf(fid, 'g20\n');
fprintf(fid, 't\n');
fprintf(fid, '%8.7f\n',tol);
fprintf(fid, 'u\n');

fprintf(fid, 'd\n');
fprintf(fid, '/Users/msoleimani/Documents/MATLAB2/R01/f1.fe\n');

fclose(fid);
%%%%%%%%%%%%%%%%%%%%%%%%%%%%%%%%%%%%%%%%%%%%%%%%%%%%%%%%%%%%%%%%%%%%%%%%%%%%%%%%%%%%%%%%%%%%%%%%%%%%%%%%%%%%

function [Pc,energy,area,stability]=solve_bridge2(alpha0,angle1,Rh)
% This function solve finds the liquid bridge shape, energy, and pressure,
% and check its stability

[status,result]=system('/usr/local/bin/evolver < solve_proc.txt');

lc=length(result);
for ii=lc:-1:1
    if result(ii-5:ii)=='energy'
        lc2=ii+3;
        for jj=lc2:lc2+50
            if result(jj:jj+4)=='scale'
                lc3=jj;
                break
            end
        end
        energy=str2num(result(lc2:lc3-3));
```

```
            break
        end
end

for ii=lc:-1:1
    if result(ii-3:ii)=='area'
        lc2=ii+3;
        for jj=lc2:lc2+50
            if result(jj:jj+5)=='energy'
                lc3=jj;
                break
            end
        end
        area=str2num(result(lc2:lc3-3));
        break
    end
end


stability=1;

C = textread('f1.fe', '%s','delimiter', '\n');
L=size(C);
for ii=1:L
    Lc=length(C{ii});
    if Lc>19
        for jj=1:Lc-18
            if C{ii}(jj:jj+18)=='lagrange_multiplier'
                Pc=str2num(C{ii}(jj+20:jj+30));
            end
        end
    end
end
```

```
for ii=10:L
    if length(C{ii})>8
        if C{ii}(1:8)=='vertices'
            start_vertices=ii+1;
        end
    end
    if length(C{ii})>5
        if C{ii}(1:5)=='edges'
            end_vertices=ii-2;
            break
        end
    end

end
ii2=1;
ii3=1;
for ii=1:(end_vertices-start_vertices)
    Li=length(C{start_vertices+ii-1});
    for jj=1:Li
        if C{start_vertices+ii-1}(jj:jj+7)== 'constrai'
            vertice=str2num(C{start_vertices+ii-1}(1:jj-1));
            nn(ii)=vertice(1);
            x(ii)=vertice(2);
            y(ii)=vertice(3);
            z(ii)=vertice(4);
            x1(ii3)=vertice(2);
            y1(ii3)=vertice(3);
            z1(ii3)=vertice(4);
            ii3=ii3+1;
            break
        elseif C{start_vertices+ii-1}(jj:jj+7)== 'original'
            vertice=str2num(C{start_vertices+ii-1}(1:jj-1));
            nn(ii)=vertice(1);
            x(ii)=vertice(2);
```

```
            y(ii)=vertice(3);
            z(ii)=vertice(4);
            x2(ii2)=vertice(2);
            y2(ii2)=vertice(3);
            z2(ii2)=vertice(4);
            ii2=ii2+1;
            break
        elseif jj>Li-8
            vertice=str2num(C{start_vertices+ii-1});
            nn(ii)=vertice(1);
            x(ii)=vertice(2);
            y(ii)=vertice(3);
            z(ii)=vertice(4);
            x2(ii2)=vertice(2);
            y2(ii2)=vertice(3);
            z2(ii2)=vertice(4);
            ii2=ii2+1;
            break
        end
    end
end

Lv=length(x);
Lv1=length(x1);
Lv2=length(x2);

jj1=1;
% finding x_max & y_max
for ii=1:Lv1  %constraint
    if (z1(ii))<0
        x_hole(jj1)=x1(ii);
        z_hole(jj1)=z1(ii);
        y_hole(jj1)=y1(ii);
        jj1=jj1+1;
```

```
    end
end
[x_max,i_xmax]=max(x_hole);
z_xmax=z_hole(i_xmax);
y_xmax=y_hole(i_xmax);

[y_max,i_ymax]=max(y_hole);
z_ymax=z_hole(i_ymax);
x_ymax=x_hole(i_ymax);

%finding closest points
d_xmax=((x2-x_max).^2+(y2-y_xmax).^2+(z2-z_xmax).^2).^0.5;
d_ymax=((x2-x_ymax).^2+(y2-y_max).^2+(z2-z_ymax).^2).^0.5;

[xmax_close,i_xmc]=min(d_xmax);
[ymax_close,i_ymc]=min(d_ymax);
x_xmc=x2(i_xmc);
y_xmc=y2(i_xmc);
z_xmc=z2(i_xmc);

x_ymc=x2(i_ymc);
y_ymc=y2(i_ymc);
z_ymc=z2(i_ymc);

slope_c_x=(z_xmax-z_xmc)/(x_max-x_xmc);
slope_c_y=(z_ymax-z_ymc)/(y_max-y_ymc);

if min(z)<z_xmax-Rh/1000
    stability=-1;
end

if slope_c_x>0 && z_xmc<z_xmax && Pc<0
    stability=1;
end
```

```

if slope_c_y>0 && z_ymc<z_ymax && Pc<0
    stability=1;
end

%
    %%%%%%%%%%%%%%%%%%%%%%%%%%%%%%%%%%%%%%%%%%%%%%%%%%%%%%%%%%%%%%%%%%%%%

function [Pc,energy,area,situation]=solve_bubble(zz)
% This function solve finds the bubble shape, energy, and
    pressure,
% and check its stability

[status,result]=system('/usr/local/bin/evolver < solve_proc.txt')
    ;

lc=length(result);
for ii=lc:-1:1
    if result(ii-5:ii)=='energy'
        lc2=ii+3;
        for jj=lc2:lc2+50
            if result(jj:jj+4)=='scale'
                lc3=jj;
                break
            end
        end
        energy=str2num(result(lc2:lc3-2));
        break
    end
end

for ii=lc:-1:1
    if result(ii-3:ii)=='area'
        lc2=ii+3;
```

```
            for jj=lc2:lc2+50
                if result(jj:jj+5)=='energy'
                    lc3=jj;
                    break
                end
            end
            area=str2num(result(lc2:lc3-1));
            break
        end
end


C = textread('f1.fe', '%s','delimiter', '\n');
L=size(C);
for ii=1:L
    Lc=length(C{ii});
    if Lc>19
        for jj=1:Lc-18
            if C{ii}(jj:jj+18)=='lagrange_multiplier'
                Pc=str2num(C{ii}(jj+20:jj+30));
            end
        end
    end
end

situation=1;

%finding vertices' coordinates
for ii=10:L
    if length(C{ii})>8
        if C{ii}(1:8)=='vertices'
            start_vertices=ii+1;
        end
    end
```

```
        if length(C{ii})>5
            if C{ii}(1:5)=='edges'
                end_vertices=ii-2;
                break
            end
        end

end
for ii=1:(end_vertices-start_vertices)
        Li=length(C{start_vertices+ii-1});
        for jj=1:Li
            if C{start_vertices+ii-1}(jj:jj+7)== 'constrai'
                vertice=str2num(C{start_vertices+ii-1}(1:jj-1));
                nn(ii)=vertice(1);
                x(ii)=vertice(2);
                y(ii)=vertice(3);
                z(ii)=vertice(4);
                break
            elseif C{start_vertices+ii-1}(jj:jj+7)== 'original'
                vertice=str2num(C{start_vertices+ii-1}(1:jj-1));
                nn(ii)=vertice(1);
                x(ii)=vertice(2);
                y(ii)=vertice(3);
                z(ii)=vertice(4);
                break
            elseif jj>Li-8
                vertice=str2num(C{start_vertices+ii-1});
                nn(ii)=vertice(1);
                x(ii)=vertice(2);
                y(ii)=vertice(3);
                z(ii)=vertice(4);
                break
            end
        end
```

```
end

if max(z)<zz-10^-4
    situation=-1;
end
```

Appendix F

Matlab code for Chapter 5

```
% This code calculates the capillary force and torque of a liquid drop at
% the intersection of two crossing filaments with prescribed liquid volume,
% contact angle, crossing angle, fibre length, separation, and
% elasto-capillary number.

clear
clc

% Defining the parameters
theta=0; % Contact angle
d0=0.5; % Separation
Len=15; % Fibre length
EI=700; % Elasto-capillary number

dV=0.5;
for delta=[30 60 90] % Crossing angle
    % Writing the results for this crossing angle
     fid = fopen('ssaavvee.m', 'w');
     fprintf(fid, 'save delta%d\n',delta);
     fclose(fid);
```

```

    % Clearing previous crossing-angle results
    clear P_m Pr_m M_m energy_m energy_t_m Li_m
    ii=1;

    V(ii)=4.1; % Initial volume
    % This loop decreases the liquid volume and calculates the force,
    % torque and energy.
    for iii=1:9
        if ii==1
            [P,Pr,M,energy,energy_t,Li,Pmax(ii)]=find_equ_fun(theta,delta,d0,Len,EI,V(ii),0,1);
        else
            [P,Pr,M,energy,energy_t,Li,Pmax(ii)]=find_equ_fun(theta,delta,d0,Len,EI,V(ii),P(1),Li(1));
        end
        LL=length(P);
        for jj=1:LL
            P_m(ii,jj)=P(jj);
            Pr_m(ii,jj)=Pr(jj);
            M_m(ii,jj)=M(jj);
            energy_m(ii,jj)=energy(jj);
            energy_t_m(ii,jj)=energy_t(jj);
            Li_m(ii,jj)=Li(jj);
        end
        Pr_f(ii)=Pr(end); % Final capillary force
        M_f(ii)=M(end);  % Final capillary torque
        energy_f(ii)=energy(end);  % Final interfacial energy
        energy_t_f(ii)=energy_t(end);  % Final total energy
        Li_f(ii)=Li(end); % Final liquid-column length

        ssaavvee
        V(ii)=V(ii-1)-dV;
```

```
        if V(ii)<0
            break
        end
    end
end

%%%%%%%%%%%%%%%%%%%%%%%%%%%%%%%%%%%%%%%%%%%%%%%%%%%%%%%%%%%%%%%%%%%%%%%%%%%%%%%%%%%%%%%%%%%%%%%%%%%%%%%%%%%%%%%%%%%%%%%%%%%%%%%%%%%%%%%%%%%%%%%%%%%%%%%%%%%%%%%
function [P,Pr,M,energy,energy_t,Li_m,Pmax]=find_equ_fun(theta,delta,d0,Lt,EI,V,P0,Li0)
% This function finds the equilibrium iteratively.

ii=1;

% Initial condition of the system with an initial force, torque, and liquid-column length.
[M(1),P(1),energy(1),Li_m]=find_force(theta,delta,V,d0,0,P0,Lt,Li0,EI,0,ii);
Li=Li_m;
% The force required for contact between the filaments.
Pmax=EI*d0/((1/384)*Li^4-(1/96)*Li^3*Lt+(1/48)*Li*Lt^3)*Li;
Pr=P; % Real force.
pp=P/Li; % Distributed load.
mm=6*M/Li^2; % Distributed torque.
% Total energy
energy_t(ii)=energy(ii)+((1/96)*pp^2*Lt^3*Li^2-(1/96)*pp^2*Lt*Li^4+(1/240)*pp^2*Li^5)/EI+((1/30240)*mm^2*Li^4*(35*Lt^2-54*Lt*Li+21*Li^2)/Lt)/EI;

% If the real force is larger than the maximum force, take the maximum force to
% calculate the filament deflection.
if P(ii)>Pmax
```

```
    P(1)=0.999*Pmax;
end

% Errors of force and torque
I1=1;I2=1;

ii=ii+1;

% Continue until the errors are smaller than 0.01.
while I1>0.01 || I2>0.01
    [M(ii),P(ii),energy(ii),Li_m(ii)]=find_force(theta,delta,V,d0
        ,M(ii-1),P(ii-1),Lt,Li_m(ii-1),EI,0,ii);
    Li=Li_m(ii);
    Pr(ii)=P(ii);
    pp=P(ii)/Li;
    mm=6*M(ii)/Li^2;
    energy_t(ii)=energy(ii)+((1/96)*pp^2*Lt^3*Li^2-(1/96)*pp^2*Lt
        *Li^4+(1/240)*pp^2*Li^5)/EI+((1/30240)*mm^2*Li^4*(35*Lt
        ^2-54*Lt*Li+21*Li^2)/Lt)/EI;
    I1=abs(P(ii)-P(ii-1));
    I2=abs(M(ii)-M(ii-1));
    Pmax=EI*d0/((1/384)*Li^4-(1/96)*Li^3*Lt+(1/48)*Li*Lt^3)*Li;
    if P(ii)>Pmax
        P(ii)=0.999*Pmax;
        I1=abs(P(ii)-P(ii-1));
    end
    ii=ii+1;
end


%
    %%%%%%%%%%%%%%%%%%%%%%%%%%%%%%%%%%%%%%%%%%%%%%%%%%%%%%%%%%%%%%%%%%%%%%%%%%%%%%%%%%%%%%%%%%%
```

```
function [M,P,energy,Li_f]=find_force(theta,delta,V,d0,M0,P0,Lt,
    Li,EI,ii1,kk1)
% This function calculates the capillary force P and torque M
    using finite
% differences.

[b0]=write_bridge(theta,delta/2,V,d0+0.01,M0,P0,Lt,Li,EI);
write_solve_bridge(ii1,kk1,b0,d0);
[energy1,area1,Li1]=solve_bridge_energy(ii1,kk1);

Pmax=EI*d0/((1/384)*Li^4-(1/96)*Li^3*Lt+(1/48)*Li*Lt^3)*Li;

% If the filaments have contact, we can not decrease d0.
if abs(P0-0.999*Pmax)<0.001
     [b0]=write_bridge(theta,delta/2,V,d0,M0,P0,Lt,Li,EI);
     write_solve_bridge(ii1,kk1,b0,d0);
     [energy2,area2,Li2]=solve_bridge_energy(ii1,kk1);
    P=(energy1-energy2)/0.02;
else
     [b0]=write_bridge(theta,delta/2,V,d0-0.01,M0,P0,Lt,Li,EI);
     write_solve_bridge(ii1,kk1,b0,d0);
     [energy2,area2,Li2]=solve_bridge_energy(ii1,kk1);
    P=(energy1-energy2)/0.04;
end

% Because of symmetry, M=0 at delta=0, 90.
if delta==0 || delta==90
    M=0;
     energy=energy2;
     Li_f=Li2;
else
     [b0]=write_bridge(theta,delta/2+1,V,d0,M0,P0,Lt,Li,EI);
     write_solve_bridge(ii1,kk1,b0,d0);
     [energy3,area3,Li3]=solve_bridge_energy(ii1,kk1);
```

```
    [b0]=write_bridge(theta,delta/2-1,V,d0,M0,P0,Lt,Li,EI);
    write_solve_bridge(ii1,kk1,b0,d0);
    [energy4,area4,Li4]=solve_bridge_energy(ii1,kk1);

   M=(energy3-energy4)/(4*pi/180);

    energy=energy2;
    Li_f=Li2;
end

%
 %%%%%%%%%%%%%%%%%%%%%%%%%%%%%%%%%%%%%%%%%%%%%%%%%%%%%%%%%%%%%%%%%%%%%%%%%%%%%%%%%%%%

function [b0]=write_bridge(angle1,phi,V,d0,M,P,Lt,Li,EI)
% This function writes the initial condition for Surface Evolver.

% Calculateing the coefficients of the shape of the deflected
    filament.
pp=P/Li;
mm=6*M/Li^2;

c5=48/2880*mm/Li/EI;
c3=80/2880*mm*Li^2/Lt/EI-120/2880*mm*Li/EI;
c1=mm*(40*Lt*Li^2-45*Li^3+12*Li^4/Lt)/EI/2880;

b4=(1/24)*pp/EI;
b2=(1/16)*pp*Li^2/EI-(1/8)*pp*Lt*Li/EI;
b0=((1/384)*pp*Li^4-(1/96)*pp*Li^3*Lt+(1/48)*pp*Li*Lt^3)/EI;

% Parameters of the initial condition.
T=-cos(angle1*pi/180);
r1=0.7;
```

```
LL=2;


fid = fopen('bridge.fe', 'w');
fprintf(fid, 'SPRING_CONSTANT 1 // for most accurate gap areas
   for constraint 1 \n');
fprintf(fid, 'SYMMETRIC_CONTENT\n');

fprintf(fid, 'PARAMETER angle = %8.7f // interior angle between
   plane and surface, degrees \n', angle1);
fprintf(fid, '#define T (-cos(angle*pi/180)) // virtual tension
   of facet on plane\n');
fprintf(fid, '#define TR 1 /* cylindre radius */\n');
fprintf(fid, 'PARAMETER phi = %8.7f\n', phi);

fprintf(fid, '#define c1 %7.6f\n',c1);
fprintf(fid, '#define c3 %7.6f\n',c3);
fprintf(fid, '#define c5 %7.6f\n',c5);

fprintf(fid, '#define b0 %7.6f\n',b0);
fprintf(fid, '#define b2 %7.6f\n',b2);
fprintf(fid, '#define b4 %7.6f\n',b4);

fprintf(fid, '#define V %7.6f\n',V);
fprintf(fid, '#define d0 %7.6f\n',d0);
fprintf(fid, '#define r1 %7.6f\n',r1);
fprintf(fid, '#define LL %7.6f\n',LL);


fprintf(fid, 'constraint 1 CONVEX // cylindrical wall\n');
fprintf(fid, 'function: ((x*cos(phi*pi/180)+y*sin(phi*pi/180))-(
   c5*(y*cos(phi*pi/180)-x*sin(phi*pi/180))^5+c3*(y*cos(phi*pi
   /180)-x*sin(phi*pi/180))^3+c1*(y*cos(phi*pi/180)-x*sin(phi*pi
   /180))))^2/(1+0.5*(5*c5*(y*cos(phi*pi/180)-x*sin(phi*pi/180))
```

```
    ^4+3*c3*(y*cos(phi*pi/180)-x*sin(phi*pi/180))^2+c1)^2)^2 + (z-
    TR-d0+(b4*(y*cos(phi*pi/180)-x*sin(phi*pi/180))^4+b2*(y*cos(
    phi*pi/180)-x*sin(phi*pi/180))^2+b0))^2/(1-0.5*(4*b4*(y*cos(
    phi*pi/180)-x*sin(phi*pi/180))^3+2*b2*(y*cos(phi*pi/180)-x*sin
    (phi*pi/180)))^2)^2 = TR^2\n');

fprintf(fid, 'constraint 2 CONVEX \n');
fprintf(fid, 'function: ((x*cos(phi*pi/180)-y*sin(phi*pi/180))+(
    c5*(y*cos(phi*pi/180)+x*sin(phi*pi/180))^5+c3*(y*cos(phi*pi
    /180)+x*sin(phi*pi/180))^3+c1*(y*cos(phi*pi/180)+x*sin(phi*pi
    /180))))^2/(1+0.5*(5*c5*(y*cos(phi*pi/180)+x*sin(phi*pi/180))
    ^4+3*c3*(y*cos(phi*pi/180)+x*sin(phi*pi/180))^2+c1)^2)^2 + (z+
    TR+d0-(b4*(y*cos(phi*pi/180)+x*sin(phi*pi/180))^4+b2*(y*cos(
    phi*pi/180)+x*sin(phi*pi/180))^2+b0))^2/(1-0.5*(4*b4*(y*cos(
    phi*pi/180)+x*sin(phi*pi/180))^3+2*b2*(y*cos(phi*pi/180)+x*sin
    (phi*pi/180)))^2)^2 = TR^2\n');

fprintf(fid, 'vertices\n');
fprintf(fid, '1 (r1*cos(phi*pi/180)+LL*sin(phi*pi/180)) (-r1*sin(
    phi*pi/180)+LL*cos(phi*pi/180)) -sqrt(TR^2-r1^2)+TR+d0
    constraint 1\n');
fprintf(fid, '2 (-r1*cos(phi*pi/180)+LL*sin(phi*pi/180)) (r1*sin(
    phi*pi/180)+LL*cos(phi*pi/180)) -sqrt(TR^2-r1^2)+TR+d0
    constraint 1\n');
fprintf(fid, '3 (-r1*cos(phi*pi/180)-LL*sin(phi*pi/180)) (r1*sin(
    phi*pi/180)-LL*cos(phi*pi/180)) -sqrt(TR^2-r1^2)+TR+d0
    constraint 1 \n');
fprintf(fid, '4 (r1*cos(phi*pi/180)-LL*sin(phi*pi/180)) (-r1*sin(
    phi*pi/180)-LL*cos(phi*pi/180)) -sqrt(TR^2-r1^2)+TR+d0
    constraint 1\n');
fprintf(fid, '5 (r1*cos(phi*pi/180)-LL*sin(phi*pi/180)) (r1*sin(
    phi*pi/180)+LL*cos(phi*pi/180)) sqrt(TR^2-r1^2)-TR-d0
    constraint 2\n');
```

```
fprintf(fid, '6 (-r1*cos(phi*pi/180)-LL*sin(phi*pi/180)) (-r1*sin
    (phi*pi/180)+LL*cos(phi*pi/180)) sqrt(TR^2-r1^2)-TR-d0
    constraint 2\n');
fprintf(fid, '7 (-r1*cos(phi*pi/180)+LL*sin(phi*pi/180)) (-r1*sin
    (phi*pi/180)-LL*cos(phi*pi/180)) sqrt(TR^2-r1^2)-TR-d0
    constraint 2 \n');
fprintf(fid, '8 (r1*cos(phi*pi/180)+LL*sin(phi*pi/180)) (r1*sin(
    phi*pi/180)-LL*cos(phi*pi/180)) sqrt(TR^2-r1^2)-TR-d0
    constraint 2\n');

fprintf(fid, 'edges /* given by endpoints and attribute */\n');
fprintf(fid, '1 1 2 constraint 1 \n');
fprintf(fid, '2 2 3 constraint 1 \n');
fprintf(fid, '3 3 4 constraint 1 \n');
fprintf(fid, '4 4 1 constraint 1 \n');
fprintf(fid, '5 5 6 constraint 2 \n');
fprintf(fid, '6 6 7 constraint 2 \n');
fprintf(fid, '7 7 8 constraint 2 \n');
fprintf(fid, '8 8 5 constraint 2 \n');
fprintf(fid, '9 1 5 \n');
fprintf(fid, '10 2 6 \n');
fprintf(fid, '11 3 7 \n');
fprintf(fid, '12 4 8 \n');

fprintf(fid, 'faces /* given by oriented edge loop */\n');
fprintf(fid, '1 5 -10 -1 9\n');
fprintf(fid, '2 6 -11 -2 10\n');
fprintf(fid, '3 7 -12 -3 11 \n');
fprintf(fid, '4 8 -9 -4 12 \n');
fprintf(fid, '5 -8 -7 -6 -5 constraint 2 tension (-cos(angle*pi
    /180)) \n');
fprintf(fid, '6 1 2 3 4 constraint 1 tension (-cos(angle*pi/180))
     \n');

```

```
fprintf(fid, 'bodies /* one body, defined by its oriented faces
    */\n');
fprintf(fid, '1 1 2 3 4 5 6 volume V density 0\n');

fclose(fid);

%
    %%%%%%%%%%%%%%%%%%%%%%%%%%%%%%%%%%%%%%%%%%%%%%%%%%%%%%%%%%%%%%%%%%%%%%%%%%%%%%%%%%

function []=write_solve_bridge(ii1,jj1,b0,d0)
% This function writes the procedure that Surface Evolver uses to
    calculate
% the equilibrium.

fid = fopen('solve_proc.txt', 'w');
fprintf(fid, 'bridge.fe\n');
fprintf(fid, 'g500\n');

fprintf(fid, 'r\n');
fprintf(fid, 'g1000\n');

fprintf(fid, 'r\n');
fprintf(fid, 'U\n');
fprintf(fid, 'g400\n');

fprintf(fid, 'r\n');
fprintf(fid, 'g250\n');

fprintf(fid, 'r\n');
fprintf(fid, 'g200\n');

fprintf(fid, 'r\n');
fprintf(fid, 'g100\n');
```

```matlab

fprintf(fid, 'list vertices where z> %7.6f\n',(d0-b0));


fprintf(fid, 'd\n');
fprintf(fid, 'solution_bridge%d%d.fe\n',ii1,jj1);

fclose(fid);

%%%%%%%%%%%%%%%%%%%%%%%%%%%%%%%%%%%%%%%%%%%%%%%%%%%%%%%%%%%%%%%%%%%%%%%%
function [energy,area,Li]=solve_bridge_energy(ii1,jj1)
% This function calculates the interface shape, energy, and pressure using
% Surface Evolver and the files written by previous functions.

[status,result]=system('/usr/local/bin/evolver < solve_proc.txt');

% Finding the energy
lc=length(result);
for ii=lc:-1:1
    if result(ii-5:ii)=='energy'
        lc2=ii+3;
        for jj=lc2:lc2+50
            if result(jj:jj+4)=='scale'
                lc3=jj;
                break
            end
        end
        energy=str2num(result(lc2:lc3-3));
        break
    end
```

```
end

% Finding the area
for ii=lc:-1:1
    if result(ii-3:ii)=='area'
        lc2=ii+3;
        for jj=lc2:lc2+50
            if result(jj:jj+5)=='energy'
                lc3=jj;
                break
            end
        end
        area=str2num(result(lc2:lc3-3));
        break
    end
end

% Finding the liquid-column length
for ii=lc:-1:1
    if result(ii-17:ii)=='Id                X'
        lc2=ii+37;
        for jj=lc2:lc
            if result(jj:jj+22)=='Enter name of dump file'
                lc3=jj-16;
                break
            end
        end
        vertices_str=(result(lc2:lc3));
        break
    end
end

lc_st=length(vertices_str);
for ii=1:lc_st-12
```

```
    if vertices_str(ii:ii+12)=='constraints 1'
        vertices_str(ii:ii+12)='             ';
    end
end
vertices_co=str2num(vertices_str);
Li=2*max(vertices_co(:,3));
```